

AEDC-TR-66-233

ARCHIVE COPY
DO NOT LOAN

ay!



INSTRUMENTATION DEVELOPMENT PROGRAM SUMMARY REPORT

R. H. Hines and F. L. Crosswy
ARO, Inc.

April 1967

Distribution of this document is unlimited.

ARNOLD ENGINEERING DEVELOPMENT CENTER
AIR FORCE SYSTEMS COMMAND
ARNOLD AIR FORCE STATION, TENNESSEE

AEDC TECHNICAL LIBRARY



PROPERTY OF U. S. AIR FORCE
AFSPC LIBRARY
AF 40(600)1200

NOTICES

When U. S. Government drawings, specifications, or other data are used for any purpose other than a definitely related Government procurement operation, the Government thereby incurs no responsibility nor any obligation whatsoever, and the fact that the Government may have formulated, furnished, or in any way supplied the said drawings, specifications, or other data, is not to be regarded by implication or otherwise, or in any manner licensing the holder or any other person or corporation, or conveying any rights or permission to manufacture, use, or sell any patented invention that may in any way be related thereto.

Qualified users may obtain copies of this report from the Defense Documentation Center.

References to named commercial products in this report are not to be considered in any sense as an endorsement of the product by the United States Air Force or the Government.

INSTRUMENTATION DEVELOPMENT PROGRAM
SUMMARY REPORT

R. H. Hines and F. L. Crosswy
ARO, Inc.

Distribution of this document is unlimited.

FOREWORD

The work reported herein was sponsored by Headquarters, Arnold Engineering Development Center (AEDC), Air Force Systems Command (AFSC), under Program Element 62405184, Project 5730, Task 573004.

The results of research presented were obtained by ARO, Inc. (a subsidiary of Sverdrup & Parcel and Associates, Inc.), contract operator of AEDC, AFSC, Arnold Air Force Station, Tennessee, under Contract AF 40(600)-1200. The research was conducted under ARO Project No. BW2401 and the manuscript was submitted for publication on January 30, 1967.

Publication of this report does not constitute Air Force approval of the report's findings or conclusions. It is published only for the exchange and stimulation of ideas.

Donald K. Law
Major, USAF
AF Representative, AEF
Directorate of Test

Leonard T. Glaser
Colonel, USAF
Director of Test

ABSTRACT

The design and operational characteristics of an in-house-built 5-cm-diam Kaufman-type ion engine that was used to evaluate diagnostic methods is presented. The discharge of the ion engine was investigated and analyzed by employing various types of material probes. The emissive probe was used to determine the beam potential. In addition, the same probe was used as an ordinary Langmuir probe to determine the electron temperature and to ascertain the ion impingement current density. The double Langmuir probe was also used to determine the electron temperature and the ion impingement current density so that cross correlation between probes could be effected. The analytical and experimental results are compared and discussed. During the course of the work a lateral ion probe was developed to determine the density of ions having a velocity transverse to the directional velocity of the exhaust. In addition, an in-house-developed instrument is described which automatically reads out the electron temperatures, thereby obviating tedious hand calculations.

CONTENTS

	<u>Page</u>
ABSTRACT	iii
NOMENCLATURE	viii
I. INTRODUCTION	1
II. PLASMA POTENTIAL MEASUREMENTS USING THE ELECTRON EMISSIVE PROBE	
2.1 Introduction	1
2.2 General Theory.	2
2.3 Experimental Apparatus and Procedures	3
2.4 Discussion of Results	4
2.5 Conclusions	6
III. DOUBLE PROBE	
3.1 Introduction	7
3.2 Theory of Double Probe	7
3.3 Determination of Electron Temperature.	8
3.4 Electron Temperature Determination by Other Methods	9
3.5 T_e of the Ion Source.	12
3.6 Automatic Electron Temperature Determination . . .	13
3.7 Conclusions	14
IV. EXPERIMENTAL ENGINE DESIGN AND PERFORMANCE EVALUATION	
4.1 General Description	14
4.2 Apparatus and Procedure	15
4.3 Evaluation of Engine Performance	16
4.4 Conclusions	23
V. LATERAL ION PROBE	
5.1 Introduction	24
5.2 Experimental Apparatus.	24
5.3 Experimental Procedure.	25
5.4 Results and Discussion	26
5.5 Conclusions	27

APPENDIX
Illustrations

Figure

1. Emissive Probe Construction Details.	33
2. Ideal Emissive Probe Characteristics	34

<u>Figure</u>	<u>Page</u>
3. Vacuum System, Engine Power Supply, Instrumentation Rack, and Related Equipment	35
4. Circuitry for Obtaining Langmuir and Emissive Probe Characteristics	36
5. Comparison of Langmuir Probe Characteristics, Contaminated and Clean	37
6. Langmuir Probe Characteristics (Temperature Effects)	38
7. Effect of Temperature and Total Accelerating Voltage on Emissive Probe Current	39
8. Emissive Probe Characteristics	41
9. Comparison of Langmuir Probe and Emissive Probe Indications of Plasma Potential	42
10. Comparison of Langmuir Probe and Emissive Probe Indications of Plasma Potential	43
11. Basic Double Probe Circuit	44
12. Double Probe Characteristics of the Exhaust of a 5-cm Electron Bombardment Ion Engine	45
13. Ideal Double Probe Volt-Ampere Characteristic	46
14. Theoretical and Experimental Electron Current Plots for the Double Probe Method	47
15. Double Probe Temperature Determination Plot	48
16. Beam Profile of 5-cm Ion Source as Obtained from the Double Probe	49
17. Block Diagram and Voltage Waveforms of Circuitry for Monitoring Te with the Double Probe	50
18. Basic Magnetoresistance Bridge Analog Division Circuit	51
19. Circuitry for Readout of Electron Temperature and Ion Density from a Double Langmuir Probe	52
20. 5-cm Electron Bombardment Ion Engine and Probe Mounting System	53
21. Schematic of Ion Engine and Power Supplies	54
22. Magnetic Field Strength versus Distance from Propellant Distributor	55

<u>Figure</u>	<u>Page</u>
23. Ionization Chamber Efficiency versus Chamber Potential Difference	56
24. Ionization Chamber Efficiency versus Chamber Potential Difference as a Function of Propellant Flow Rate	57
25. Ion Beam Current versus Neutral Propellant Flow Rate	58
26. Emissive Probe and Ion Beam Impingement Probe Circuitry	59
27. Radial Ion Beam Density Profile (Impingement Probe).	60
28. Radial Plasma Potential Profile	61
29. Axial Plasma Potential Profile	62
30. Power Efficiency versus Ionization Chamber Potential.	63
31. Probe Voltage-Current Curves in the Ambient Plasma Stream.	64
32. Probe Voltage-Logarithm of Current Curves in the Ambient Plasma Stream	65
33. Probe, Shield, and Traverse System	66
34. Langmuir Characteristic Equipment Schematic	67
35. Wake Investigation Equipment Schematic	68
36. Neutralizer Emission Current versus Neutralizer Heater Current.	69
37. Positive Charge Distribution in the Wake (Shield 0.1 in. from Probe).	70
38. Positive Charge Distribution in the Wake (Shield 1.1 in. from Probe).	71
39. Positive Charge Distribution in the Wake (Shield 2.1 in. from Probe).	72
40. Positive Charge Distribution in the Wake (Shield 3.1 in. from Probe).	73
41. Positive Charge Distribution in the Wake (Shield 4.1 in. from Probe).	74

<u>Figure</u>		<u>Page</u>
42. Area of Probe Exposed as it Passes under the Shield.		75
43. Contour Plot of Positive Ions in the Wake (0 v on Shield).		76
44. Contour Plot of Positive Ions in the Wake (-50 v on Shield)		77
45. Contour Plot of Positive Ions in the Wake (-100 v on Shield)		78
46. Current Distribution Collected by Probe Biased 6.0 v (Shield 0.1 in. from Probe)		79
47. Current Distribution Collected by Probe Biased 6.0 v (Shield 1.1 in. from Probe)		80
48. Current Distribution Collected by Probe Biased 6.0 v (Shield 2.1 in. from Probe)		81
49. Current Distribution Collected by Probe Biased 6.0 v (Shield 3.1 in. from Probe)		82
50. Current Distribution Collected by Probe Biased 6.0 v (Shield 4.1 in. from Probe)		83
51. Probe Current Difference (0 v on Shield)		84
52. Probe Current Difference (-50 v on Shield)		85
53. Probe Current Difference (-100 v on Shield)		86

NOMENCLATURE

A	Specified point on voltage-current characteristic curve corresponding to V_A , amplifier gain
A_1	Area of probe 1
A_2	Area of probe 2
B	Specified point on voltage-current characteristic curve; magnetic field strength
D	Arbitrary region in double probe characteristic curve
d	Probe diameter

e/m	Charge-to-mass ratio
E _w	Material work function
e	Instantaneous voltage, electron charge
e _a	Instantaneous voltage proportional to i _a
e _b	Instantaneous voltage proportional to i _n
e _c	Instantaneous reference voltage
F	Arbitrary region on double probe characteristic curve
\bar{F}	Lorentz force
f	Distribution function for the particle in phase space
g	Gravitational acceleration constant
I _A	Accelerator drain current
I _B	Ion beam current
I _C	Neutralizer emissive current
I _F	Cathode heater
I _H	Total positive high voltage current
I _I	Anode current
I _m	Magnetic field coil current
I _{NE}	Neutral propellant flow rate
I _n	Neutralizer heater current
I _o	Zeroth order Bessel function
I _{sp}	Specific impulse
i _a	Current between double probes caused by V _A
i _b	Current between double probes caused by V _B
i _d	Double probe to probe current
i _{e1}	Electron current to probe 1 of double probe
i _{e2}	Electron current to probe 2 of double probe
i _j	Current collected by probe in the wake
i _{i_o}	Current collected by probe in ambient stream
i _o	Probe current at plasma potential
i _p	Probe current

i_{p_1}	Ion current to probe 1 of double probe
i_{p_2}	Ion current to probe 2 of double probe
Σi_p	Total ion current to double probe
i_r	Probe collection of random plasma electron current
J_B	Beam current
J_{NE}	Neutral propellant flow rate, equivalent amperes
j_r	Random electron current density impinging on probe 1
j_{r_2}	Random electron current density impinging on probe 2
K	Magnetoresistance bridge (MRB) proportionality constant
K_1	Geometric constant
K_2	Geometric constant
k	Boltzmann constant
m	Mass
n	Neutral particle density
n_{e_0}	Electron density in ambient plasma
n_e	Electron density
n_i	Ion density
n_{i_0}	Ion density in ambient plasma
P_F	Cathode heating power
R	Radius of circular disk
R_o	Dropping resistor
r	Effective radius of probe
\bar{r}	Space vector
T	Thermal temperature
T_e	Electron temperature
T_h	Thrust
U	Potential energy
\bar{v}	Directed velocity
\bar{v}	Random velocity
v^1	$\bar{v} + \bar{v}$
V_1	Voltage at probe 1

V_2	Voltage at probe 2
V_A	Accelerator potential
V_C	Neutralizer bias potential
V_d	Double probe to probe voltage
V_I	Anode potential
V_N	Neutralizer heater potential
ΔV_F	Cathode filament potential difference
ΔV_I	Ionization chamber potential difference
ΔV_m	Magnetic field potential difference
V_ϕ	Difference in potential between probe bias and plasma
X, Y, Z	Input signals to MRB
x, y, z	Specified regions on double probe characteristic curve
$\bar{x}, \bar{y}, \bar{z}$	Rectangular coordinate axes
δ	Unit step function
η	Overall engine power efficiency
η_u	Propellant utilization efficiency
ξ_0	Permittivity of free space
σ	Ratio of ambient plasma currents
ϕ	Reciprocal thermal voltage $\left(\frac{e}{kt}\right)$
$\Delta \bar{r}$	Gradient with respect to ordinary space
∇_v	Gradient with respect to velocity

SECTION I INTRODUCTION

The development of electrical propulsion devices has progressed to the point where extensive testing in the ground test facility complex for extended periods of time is required to ascertain their reliability and endurance. Of dictating importance is the ascertainment of component deterioration under extended periods of operation and the effect of this deterioration upon system performance. One means of determining certain variations in engine performance is by monitoring the exhaust efflux of the engine throughout the operating lifetime. Numerous methods have been suggested to adequately effect ion beam diagnostics, foremost among which are the complex of Langmuir probes. A study was, therefore, initiated to ascertain the feasibility of using a number of different types of ion beam probes to perform engine exhaust diagnostics for extended periods of time under laboratory space simulation conditions as described in Section IV.

The purpose of this report is to summarize the analytical and experimental work that has been conducted in effecting ion beam diagnostics. The measuring techniques that were used centered about the emissive and double Langmuir probes to determine electron and ion current densities, degree of beam neutralization, electron and ion temperatures, and the interaction of the energetic exhaust particles with the probes per se. To effect comparison and correlation among the different probe techniques, a 5-cm-diam Kaufman-type ion engine was designed and constructed. During the course of the work, an ion probe was also developed to measure radial ion velocities and current densities so that a comparison with the current density in the direction of the exhaust could be made. An automatic means for direct readout of electron temperatures was developed to expedite electron temperature measurement, thereby obviating tedious calculations. The results of the work, both theoretical and experimental, are presented, including recommendations for future developmental effort.

SECTION II PLASMA POTENTIAL MEASUREMENTS USING THE ELECTRON EMISSIVE PROBE

2.1 INTRODUCTION

The successful operation of an electrical propulsion device employing an electrostatically accelerated positive ion beam requires charge neutralization of the ion beam. One simple and adequate method to effect charge,

and ultimately current, neutralization is by immersing a thermionic electron emitter into the ion beam. If the ion engine is operated in space or under simulated space conditions where the neutralizer is the predominant source of negative charge carriers, the plasma will attain a sufficiently high potential with respect to the neutralizer to extract the necessary neutralizing electrons. Therefore, a sensitive and accurate measurement of plasma potential is a direct indication of the effectiveness of any neutralization scheme. It has been shown (Refs. 1 through 5) that the electron emissive probe is an accurate means for measuring the plasma potential of a neutralized positive ion beam from an ion engine.

2.2 GENERAL THEORY

The emissive probe basically consists of a U-shaped tungsten filament heated to thermionic temperature and inserted into the ion beam at the point where plasma potential is to be sensed. The probe is biased through a range of voltages and the probe current recorded at each bias setting. Plasma potential is determined by a pronounced break point in the voltage bias-probe current characteristic as the bias voltage is varied through a range of values including the plasma potential. The details of the probe construction are shown in Fig. 1 and an ideal characteristic is shown in Fig. 2. The probe emission characteristics, as a function of bias voltage, are described in three separate regions:

- With the probe biased strongly negative, with respect to plasma potential, the emission is ideally governed by the Richardson-Dushman equation:

$$i_p = K_1 T^2 \exp\left(-\frac{E_w}{kT}\right) \quad (2.1)$$

- With the probe biased near the plasma potential, the emission current is space charge limited and is governed by Child's law:

$$i_p = K_2 V \phi^{\frac{3}{2}} \quad (2.2)$$

where K_2 is a geometric constant for a constant positive ion current density and neutralizing electron current density.

- With the probe biased positively with respect to plasma potential, the emission is governed by the Maxwell-Boltzmann temperature distribution of the thermionic electrons:

$$i_p = i_0 \exp\left(-\frac{eV\phi}{kT}\right) \quad (2.3)$$

where i_0 is the probe current when the probe bias equals plasma potential and T is the temperature of the emitted electrons.

To obtain the true characteristic of the emissive probe, the currents caused by ion impingement and the "Langmuir" current of electrons must be subtracted from the total probe current to yield the true emission current. Since the cross-sectional area of the probe is quite small, the ion impingement current is extremely low and may be neglected.

A procedure for subtracting the "Langmuir" current from the total probe current, outlined in Ref. 2, was employed in the present investigation. With the probe biased negatively with respect to plasma potential, the probe heating current was adjusted until the emitted electron current was small compared to the total ion beam current. The total probe current was recorded at this bias level. The heater current was then reduced until the probe was no longer thermionic and a value of the "Langmuir" current at the same bias recorded. The procedure of recording total probe current then "Langmuir" current is repeated for each bias point until the entire probe characteristic is obtained.

2.3 EXPERIMENTAL APPARATUS AND PROCEDURES

The emissive probe was traverse-mounted in the bell jar test rig shown in Fig. 3 and described in Section IV. The traverse allowed radial and axial positioning of the probe. All the data were obtained using argon as the propellant gas. The beam current was adjusted to 20 ma and the net beam acceleration potential was held at 2000 v. The test cell pressure was typically 1×10^{-5} torr with the ion engine operating.

The values of probe bias and plasma potential were referenced to laboratory "ground." The ion beam was terminated on an electrically floating stainless steel plate. For this condition of operation, the neutralizer furnished virtually all the neutralizing charge carriers. For a well neutralized beam the plasma potential closely follows the positive neutralizer bias values so that the approximate value of plasma potential is known before any probe data are recorded. To provide equipotential emitting surfaces for both the neutralizer and the emissive probe, the heater currents of both were supplied by in-phase, half-wave-rectified pulses with the probe data taken during the interval between pulses. A schematic of the equipment used to record Langmuir and emissive probe characteristics is shown in Fig. 4.

Langmuir probe characteristics were taken with the probe heater current reduced to a value such that the probe was not emissive. The velocity distribution of the neutralizing electrons was assumed to be Maxwellian since the characteristics obtained exhibited a linear relationship between the logarithm of probe current versus probe bias in the region described by:

$$i_p = i_r \exp(-\phi V_\phi) \quad (2.4)$$

where i_r is the plasma random electron current.

When the emissive probe is switched to position 3 (Fig. 4), the probe is essentially isolated from ground and assumes a floating potential that is very near the plasma potential. This floating emissive probe device is particularly interesting since indications of plasma potential can be read out directly on a voltmeter, eliminating the necessity of analytical interpretation of the probe volt-ampere characteristics.

The problem of accurately determining the plasma potential was approached by correlating the data as obtained from the cool-filament emissive probe (used as a Langmuir probe), the biased emissive probe, and the floating emissive probe.

2.4 DISCUSSION OF RESULTS

A study was conducted to determine the effects of probe contaminants on interpretation of Langmuir probe characteristics. Small amounts of diffusion pump oil vapors were found to condense on cool surfaces within the vacuum system, and a probe was considered to be contaminated if left in the vacuum system at room temperature for several hours. The probes were cleaned by heating to approximately 2000°C for several minutes and then allowing them to cool before a Langmuir probe characteristic was taken. The characteristics shown in Fig. 5 are typical of the comparison of the clean and contaminated probes, and it can be seen that the interpreted values of plasma potential agree within several tenths of a volt even though the probe current for the clean condition was the larger throughout the Langmuir probe characteristic region of interest.

Several Langmuir probe characteristics were taken for identical ion beam conditions but for different probe temperatures. Figure 6 illustrates the effect of temperature on the Langmuir probe characteristics. It can be seen that in the region in which the probe was biased negatively with respect to plasma potential, the probe currents differed widely as a function of temperature. This fact made it quite difficult to follow the procedure set forth in Ref. 2 and outlined in Section 2.1 concerning the

subtraction of the Langmuir current from the total probe current to yield the true emission characteristic of the emissive probe. After a data point was obtained with the probe at emission temperature, it was quite difficult to return the probe to the same temperature as the previous Langmuir probe data point. Changes in the Langmuir probe current from data point to data point as a function of probe bias could not be accurately obtained because of the temperature effect. Subsequent emissive probe data were obtained with emission currents greater than the collected Langmuir current of electrons, and no further attempts were made to subtract the Langmuir current from the total probe current.

Emissive probe characteristics were obtained for a wide range of ion beam densities and beam energies, for a wide range of plasma potentials, and for a wide range of emissive probe temperatures. All characteristics exhibited a slope in region 1 shown in Fig. 2 and did not ideally obey the Richardson-Dushman equation. A procedure was devised to investigate the nature of the probe emission in this region. The probe was first brought to an equilibrium temperature as measured with an optical pyrometer. With all other ion beam parameters held constant, the ion engine neutralizer bias was successively switched between three different neutralizer bias voltages for a certain emissive probe bias. In this manner the total accelerating voltages as experienced by the emitted electrons, V_ϕ , could be rapidly varied with assurance that engine operation and other ion beam parameters were essentially constant. The values of plasma potential closely followed the bias placed on the neutralizer as explained in Section 2.2. Figure 7 shows that the probe emission was temperature dependent, as expected, and seemed to be linearly dependent upon V_ϕ , which was not expected. A re-examination of Fig. 6, for the same bias region of the Langmuir probe characteristic, also revealed a linear dependence of probe current upon V_ϕ in the region in which the probe bias is strongly negative with respect to plasma potential. This departure of the emitted electron current from that predicted by the Richardson-Dushman equation for the emissive probe is possibly caused by surface contamination of the tungsten filament which is not remedied by the high temperature cleaning procedure described above in Section 2.3. Surface contamination of the probe filament was evidenced by levels of thermionic emission much greater than that tabulated for clean tungsten surfaces (Ref. 6). With the electron emission at least an order of magnitude greater than the collected Langmuir current, at probe bias levels close to the plasma potential, and with the probe current attributable to ion impingement being negligibly small because of the small area of the probe filament, typical emissive probe characteristics appeared as shown in Fig. 8. Regions 2 and 3 correspond to the same regions on Fig. 2; however, Region 1 of Fig. 8 and Fig. 2 differ as explained above.

A series of probe characteristics was recorded to compare the values of plasma potential as indicated by the biased emissive probe, the floating emissive probe, and the Langmuir probe. Figure 9 contains the data obtained with a biased emissive probe and a Langmuir probe for a neutralizer bias of 6.253 v. Within the accuracy of graphical interpretation, the value of plasma potential as indicated by the two probe characteristics is seen to compare favorably. The floating emissive probe indication of plasma potential was 7.4 v. Figure 10 is a comparison of probe characteristics for a neutralizer bias of 23.69 v. Again the two probe indications of plasma potential are seen to compare favorably. The floating emissive probe indication of plasma potential was 25 v.

Proper plotting of the Langmuir probe characteristics should take into account the contribution to the total probe current by positive ion impingement. However, as can be deduced from Fig. 6 an evaluation of ion impingement current would be somewhat arbitrary because of the electron emission process discussed previously. A calculation of ion impingement current considering the total ion beam current, relative beam density profiles, and the probe surface area showed that actual ion impingement currents should be small compared to the current of collected electrons in the probe bias region described by the Maxwell-Boltzmann relation.

Probe characteristics were recorded as the plasma potential was varied through a range of values from 6 to 50 v and total ion beam current was varied from 10 to 50 ma. The characteristics shown in Figs. 9 and 10 are typical of the data recorded.

2.5 CONCLUSIONS

The determination of plasma potential using the probe shown in Fig. 1 as both a Langmuir and an electron emissive probe was hampered because of a V_ϕ dependent electron emission effect in the bias region in which probe bias was negative with respect to the plasma potential. This emission effect caused emissive probe emission characteristics different from that predicted by the Richardson-Dushman equation. The effect also obscured interpretation of ion impingement current with the Langmuir probe. Fortunately, however, for interpretations of plasma potential the effect was not noted in either the Langmuir or the emissive probe characteristics as the probe bias approached and surpassed the plasma potential. Interpretations of plasma potential by the biased emissive probe and the Langmuir probe were found to agree to within several tenths of a volt. The floating emissive probe indications of plasma potential were consistently from 1 to 1-1/2 v above the values indicated by the other two probes.

SECTION III DOUBLE PROBE

3.1 INTRODUCTION

Since the single probe interacts with the beam by extracting additional electrons from the neutralizer when the probe is positively biased, the double probe developed by E. O. Johnson and L. Malter (Ref. 7) and extended by L. D. Dickson (Ref. 8) was employed for obtaining the beam volt-ampere characteristic. The beam characteristic was compared to that obtained from a gas discharge. Five different methods were used to determine the beam electron temperature from a typical beam double probe volt-ampere characteristic. An electronic circuit was developed to continuously monitor the beam electron temperature.

As with the single Langmuir probe, operation of the double probe is based upon the Boltzmann relation and the plasma sheath properties of a gas discharge. As will be shown later, the beam double probe characteristic, BDPC, is identical to that of a gas discharge in which the distribution of electrons is Maxwellian. The distribution of electrons for an ion engine is an accelerated half-Maxwellian. Electrons are thermally emitted from the neutralizer electrode in a Maxwellian distribution. The neutralizer is biased at a small positive potential. The beam then assumes a potential several volts more positive than the bias voltage so that the beam can extract enough electrons to become neutralized. The electrons are immediately accelerated by this small voltage difference longitudinally in the direction of ion flow and they then drift with the ion flow. This action gives rise to electrons with energies of several electron volts or temperatures in the 10,000°K range.

Because the ions are accelerated through hundreds of volts, they are energetic enough to be unaffected by the small probe bias. Therefore, a positive ion sheath does not exist about the double probe as exists about the single probe. However, the energetic ions that impinge upon the probe surface release secondary electrons from the surface.

3.2 THEORY OF DOUBLE PROBE

The double probe is composed of two identical, closely spaced single probes. A potential difference, V_d , is applied between the two probes, and the resulting current i_d is measured (Fig. 11).

For simplicity, without undue sacrifice in accuracy, the following assumptions can be made: the probes are equal in area, no differences in the ionized discharge exist within close proximity to the probes, and V_d has no effect on the ion current of the system.

Then when V_d is zero, each probe will collect zero net current from the plasma, and both probes will assume floating potential. The current i_d is then zero since there is no net potential existing in the loop. This condition corresponds to point zero on the curve of Fig. 12.

When V_d is some small negative voltage, the probe potentials with respect to the plasma must adjust themselves so that the basic current relations are still satisfied. When probe 1 is closer to plasma potential and collects more electrons, probe 2 is farther from plasma potential and collects fewer electrons. The added electrons flowing from probe 1 pass through the circuit to supply the deficiency at probe 2. This condition corresponds to point A on Fig. 12.

As V_d is made still more negative, probe 1 is closer to space potential and collects the entire electron current to the system since probe 2 is so highly negative with respect to the plasma that no electrons can reach it. Half the electrons reaching probe 1 then pass through the external circuit to probe 2. This corresponds to point B on Fig. 12.

Making V_d more negative should cause no further change in the current distribution because probe 1 already collects sufficient electron current to balance the entire positive ion current flowing to the system. Consequently, probe 1 remains fixed with respect to the plasma, and probe 2 goes negative with V_d . Probe 2 is now saturated with positive ions and the curve in Fig. 12 should become flat along the region xy because further increases in voltage should cause no further increase in current. However, because of ionization of residual gases and emission of secondary electrons from the probes by ion-surface interactions, the voltage-current curves have a slight slope at the extremes.

3.3 DETERMINATION OF ELECTRON TEMPERATURE

Since the system is symmetric, a reversal of V_d to positive will merely cause the previous results to be reversed. The portion of the curve oyx becomes ozw. The relatively flat portion, zw, corresponds to the positive ion impingement at probe 1. The total ion current to the system is simply the sum of the positive ion currents to both probes and can be found by adding the two currents corresponding to points y and z of the curve. Thus:

$$\Sigma i_p = i_{p_1} + i_{p_2} \quad (3.1)$$

The electron current which flows from the plasma to probe 2 is the difference between the total space current and the positive ion current to

the probe. Thus, the electron current to probe 2 is expressed as:

$$|i_{e_2}| = |i_d| - |i_{p_2}| \quad (3.2)$$

Since, for any given V_d , the total current to the system must be zero:

$$i_{p_1} + i_{p_2} = \Sigma i_p = i_{e_1} + i_{e_2} \quad (3.3)$$

where i_{e_1} is the electron current caused by the electrons which are sufficiently energetic to overcome the retarding potential on the probe. This current is expressed by the Boltzmann relation:

$$i_{e_1} = i_{o_1} \exp\left(-\frac{eV_1}{kT_e}\right) = i_{o_1} \exp(-\phi V_1) \quad (3.4)$$

where i_{o_1} is the random electron current adjacent to probe 1.

Similarly,

$$i_{e_2} = i_{o_2} \exp(-\phi V_2) \quad (3.5)$$

Then

$$\frac{\Sigma i_p}{i_{e_2}} - 1 = \frac{i_{o_1}}{i_{o_2}} \exp[-\phi(V_1 - V_2)] = \sigma \exp(-\phi V_d) \quad (3.6)$$

where

$$\sigma = \frac{i_{o_1}}{i_{o_2}} \text{ and } V_d = V_1 - V_2$$

$$\ln\left[\frac{\Sigma i_p}{i_{e_2}} - 1\right] = \ln\sigma - \phi V_d \quad (3.7)$$

Thus the plot of $\ln\left[\frac{\Sigma i_p}{i_{e_2}} - 1\right]$ versus V_d should yield a straight line whose slope is a measure of the electron temperature. This method of determining T_e is known as the logarithmic plot method.

3.4 ELECTRON TEMPERATURE DETERMINATION BY OTHER METHODS

Since

$$i_{e_2} = \frac{\Sigma i_p}{1 + \sigma \exp(-\phi V_d)} \quad (3.8)$$

differentiate i_{e_2} with respect to V_d .

$$\frac{di_{e_2}}{dV_d} = \frac{\sigma \phi \Sigma i_p \exp(-\phi V_d)}{[(1 + \sigma) \exp(-\phi V_d)]^2} \quad (3.9)$$

at $V_d = 0$

$$\left[\frac{di_{e_2}}{dV_d} \right]_{V_d=0} = \left[\frac{di_d}{dV_d} \right]_{V_d=0} = \frac{\sigma \phi \Sigma i_p}{(\sigma + 1)^2} \quad (3.10)$$

Let $R_o = \frac{dV_d}{di_d}$ = equivalent resistance

so that

$$T_e = 11,600 \left[\frac{\sigma \Sigma i_p}{(\sigma + 1)^2} \right] R_o \quad (3.11)$$

This method of determining T_e is known as the equivalent resistance method.

A general approximation for T_e can be obtained for probes of equal area since then $\Sigma i_p = 2i_{p_0}$ and $\sigma = 1$ ($i_{o1} = i_{o2}$)

$$T_e = \frac{11,600 (1)}{4} 2i_{p_0} \frac{V_p}{i_{p_0}} = 5800 V_p \quad (3.12)$$

where

$$R_o = \frac{V_p - 0}{i_{p_0} - 0} = \frac{V_p}{i_{p_0}}$$

Equation (3.7) can again be rearranged as

$$V_d = -\frac{1}{\phi} \ln \left[\frac{1}{\sigma} \left(\frac{\Sigma i_p}{i_{e_2}} - 1 \right) \right] \quad (3.13)$$

Now let V_d'' be the value of V_d which corresponds to $\frac{\Sigma i_p}{i_{e_2}} = D$, and let V_d' be the value of V_d which corresponds to $\frac{\Sigma i_p}{i_{e_2}} = F$ where D and F are arbitrarily in region yoz near y and z in Fig. 12.

Then

$$T_e = 11,600 \left[\frac{V_d'' - V_d'}{\ln(F - 1) - \ln(D - 1)} \right] \quad (3.14)$$

This is known as the intercept method of determining T_e .

Again consider Eq. (3.8) with σ unity rearranged as:

$$\frac{\Sigma i_p}{i_{e_2}} - 1 = \exp(-\phi V_d) \quad (3.15)$$

Since for symmetrical probes, $i_{p1} = i_{p2} = i_p$; $\Sigma i_p = 2i_p$ and $i_{e2} = i_d + i_p$ then

$$\frac{i_p + i_d}{i_p - i_d} = \exp(-\phi V_d) \quad (3.16)$$

$$\frac{1}{2} \ln \left(\frac{1 + \frac{i_d}{i_p}}{1 - \frac{i_d}{i_p}} \right) = 1/2 \phi V_d \quad (3.17)$$

$$\tanh^{-1} \left(\frac{i_d}{i_p} \right) = 1/2 \phi V_d \quad (3.18)$$

$$\phi = \frac{2 \tanh^{-1} \left(\frac{i_d}{i_p} \right)}{V_d} = \frac{11,600}{T_e} \quad (3.19)$$

$$T_e = \frac{5800 V_d}{\tanh^{-1} \left(\frac{i_d}{i_p} \right)} \quad (3.20)$$

This is known as the hyperbolic tangent method of determining T_e .

The ideal double current-voltage characteristic function is given by the equation

$$\frac{i_d}{i_p} = \tanh \left(\frac{\phi V_d}{2} \right) \text{ or } Y = \tanh X \quad (3.21)$$

where

$$X = \frac{\phi V_d}{2} = \frac{e}{2kT_e} V_d \text{ and } Y = \frac{i_d}{i_p} \quad (3.22)$$

A plot of Eq. (3.21) is given in Fig. 13.

The ideal electron current plot for the double probe is given by rearranging Eq. (3.15) as

$$\frac{i_{e2}}{i_p} = \frac{2}{1 + \exp \left(-\frac{\phi V_d}{2} \right)} = \frac{2 \exp \left(\frac{\phi V_d}{2} \right)}{\exp \left(\frac{\phi V_d}{2} \right) + \exp \left(-\frac{\phi V_d}{2} \right)} = \frac{\exp \left(\frac{\phi V_d}{2} \right)}{\cosh \left(\frac{\phi V_d}{2} \right)} \quad (3.23)$$

then

$$\ln \left(\frac{i_{e2}}{i_p} \right) = 1/2 \phi V_d - \ln \cosh (1/2 \phi V_d) \quad (3.24)$$

or

$$Y = X - \ln \cosh X \quad (3.25)$$

where

$$Y = \ln \frac{i_{e2}}{i_p}$$

and

$$X = (1/2 \phi V_d)$$

A plot of Eq. (3.25) is given in Fig. 14.

3.5 T_e OF THE ION SOURCE

The double probe voltage-current characteristic of Fig. 12 was obtained from a double probe inserted in the exhaust of the 5-cm electron bombardment ion engine, described in Section 4.2, operated at 10-ma emission. The acceleration and deceleration grids were at +2000 and -400 v, respectively, and the neutralizer was biased at 6.0 v. The electron temperature, T_e , of the exhaust was computed from the characteristic as follows:

(a) Equivalent Resistance Method:

$$\begin{aligned} T_e &= 11,600 \left[\frac{\sigma \Sigma i_p}{(\sigma + 1)^2} \right] \left[\frac{dV_d}{di_d} \right]_{V_d=0} \\ &= 11,600 \left[\frac{1 (2.85 + 2.60) \times 10^{-6}}{(1 + 1)^2} \right] \left[\frac{7v}{3.4 \times 10^{-6}} \right] \\ &= 32,600^\circ K \end{aligned}$$

(b) Approximation Method:

$$T_e = 5800 V_p = 5800(6) = 34,800^\circ K$$

(c) Intercept Method:

$$T_e = 11,600 \left[\frac{V_d'' - V_d'}{\ln \left(\frac{F-1}{D-1} \right)} \right]$$

at D,

$$\Sigma i_p'' = 5.40 \text{ ma}$$

$$V_d'' = 4 \text{ v}$$

$$i_{e_2}'' = 4.4 \text{ ma}$$

$$D = \frac{\Sigma i_p''}{i_{e_2}''} = 1.23$$

$$D - 1 = 0.23$$

at F,

$$\Sigma i_p' = 5.40 \text{ ma}$$

$$V_d' = -4 \text{ v}$$

$$i_{e_2}' = 0.85 \text{ ma}$$

$$F = \frac{\Sigma i_p'}{i_{e_2}'} = 6.35$$

$$F - 1 = 5.35$$

$$T_e = 11,600 \left[\frac{4 - (-4)}{\ln \left(\frac{5.35}{0.23} \right)} \right] = \frac{11,600 (8)}{\ln 23} = 29,500^\circ K$$

(d) Tanh⁻¹ Method:

$$T_e = \frac{5800 V_d}{\tanh^{-1} \left(\frac{i_d}{i_p} \right)} = \frac{5800 (4)}{\tanh^{-1} \left(\frac{1.9}{2.85} \right)} \text{ at } D = 28,700^\circ K$$

(e) Log Plot Method:

The ln plot of $\left[\frac{\Sigma i_p}{i_{e_2}} - 1 \right]$ versus voltage is plotted in Fig. 15. At Δv equals 2.73 v, $\Delta \left(\frac{\Sigma i_p}{i_{e_2}} - 1 \right)$ equals 2.7

$$T_e = 11,600 \times \text{slope} = 11,600 \times 2.7 = 31,300^\circ K$$

The experimental electron current plots for the double probe are compared to the theoretical plot in Fig. 14. The electron currents in the ion beam are very close to the theoretical values for a T_e of 32,000°K.

Since the effective area of each probe of the double probe is approximately 0.052 in.², and the ion saturation current is approximately 3 μ amp, the beam ion density is about 4.25 μ amp/in.². The theoretical density of the 5-cm engine at 10- μ amp emission is 3.33 μ amp/in.². The higher experimental value is reasonable since the emission is not homogeneously distributed, and the probe is in the center of the beam. The experimental ion beam density profile is shown in Fig. 16. The twin peaks near the source correspond to the geometry of the engine neutralizer.

3.6 AUTOMATIC ELECTRON TEMPERATURE DETERMINATION

T_e may be determined electronically from the equivalent resistance method. Let V_A corresponding to dV_d be a small voltage source such that point A is in the region o-z; then i_A corresponds to d_i_d . Also, let V_B be large such that point B is in the region z-w; then i_B remains essentially constant for increasing voltages and corresponds to $1/2 \Sigma i_p$. Then T_e becomes $5800 V_A \frac{i_b}{i_a}$.

The impressed voltage between the probes is chopped between V_A and V_B as shown in Fig. 17. The IR drop across R_o is a square-wave voltage with peaks e_A and e_B proportional to i_A and i_B . This square wave is isolated from ground through a pair of isolation amplifiers and boosted through a high gain amplifier. The signals are then recovered through a reverse chopper and filter circuit that splits the square wave into two d-c

voltages of amplitudes e_A and e_B . The ratio of the two voltages is then obtained through a Hall-effect magnetoresistance bridge, MRB, multiplier circuit with a proportionality constant introduced so that the output is a direct reading of T_e .

The MRB output voltage Z is equal to the product of the inputs X and Y and a proportionality constant K as shown in Fig. 18. Since $Y = e_A - e_C$ and $X = e_B - Az$; X can be derived as a function of e_A , e_B , and e_C from:

$$X = \frac{e_B}{1 + AKe_A - AKe_C} \quad (3.26)$$

By setting the feedback amplifier gain A equal to $1/K$ and e_C equal to unity, $X = \frac{e_B}{e_A}$.

The composite circuit schematic is shown in Fig. 19. The circuit was constructed around the Philbrick operational manifold MP using P65AU amplifiers with the current gain necessary to drive the MRB being supplied by two P2-P5 pairs. The MRB was the American Aerospace Controls, Inc., 3054 Mistor®.

3.7 CONCLUSIONS

The instrument is used to monitor the exhaust of the 5-cm ion engine with the recorded T_e usually agreeing within ten percent of the mean values obtained with the more laborious and time consuming methods and analytical interpretations discussed.

Values of V_A at 1.35 v and V_B at 22.5 v were found to be satisfactory for all ranges of engine operation.

SECTION IV

EXPERIMENTAL ENGINE DESIGN AND PERFORMANCE EVALUATION

4.1 GENERAL DESCRIPTION

This section of the report is concerned with the design, construction, and evaluation of engine operating characteristics of the laboratory-type electron bombardment ion source. A brief description of the diagnostic devices used to obtain the ion beam characteristics is also included. Although the superior performance characteristics of electron-bombardment-type engines larger than the 5-cm-diam engine are well

documented (Refs. 9 and 10), the deciding factor in the design of this particular engine was that the engine size be compatible with an existing bell-jar vacuum system.

The experimental evaluation of the engine performance will be discussed in the following order:

1. Gas Distributor Performance
2. Magnetic Field Characteristics
3. Ionization Chamber Performance
4. Cathode Performance
5. Accelerator Performance
6. Neutralizer Performance
7. Overall Engine Power Efficiency

4.2 APPARATUS AND PROCEDURE

A 5-cm-diam ion engine (Fig. 20) was constructed and a schematic diagram of the engine and associated power supplies is shown in Fig. 21. The engine was fabricated from type 347 stainless steel except for the electrical insulators, the refractory metal cathode and neutralizer (Refs. 9, 10, 11, 12, 13, and 14). Although engine operation is possible with virtually any propellant gas or vapor, argon was used for all the experiments that are discussed even though nitrogen and hydrogen have also been used for comparative performance evaluation. The propellant gas flow rate, controlled by means of a calibrated orifice, passes through the distributor (Fig. 21) into the ionization chamber, which consists of a 5-cm-diam cylindrical anode and a thermionic cathode coaxial with the anode. Electrons, emitted from the cathode, are accelerated by the anode-cathode potential difference and ionize the propellant particles. A solenoidal winding surrounding the ionization chamber provides an axial magnetic field which increases the path of electron travel from cathode to anode thereby enhancing the probability of a collision with neutral propellant particles.

Ionization collisions with the neutral particles create a plasma within the chamber with some of the positive ions tending to diffuse or drift to the area of the screen. An electric field is established between the screen and accelerator, and ions in this region are accelerated through the match-drilled holes to form the ion beam. The spacing between the screen and accelerator can be varied by changing the size of spherical aluminum oxide spacers. In this way, the total screen-accelerator voltage is variable up

to 6000 v. The accelerator voltage is usually set to a value to provide minimum beam divergence, but in all cases the magnitude of the negative voltage is of a sufficient value to prevent electron backstreaming through the accelerator. The separation distance between the screen and accelerator was set at 5/32 in. for all presently discussed data. The positive ion beam issuing from the accelerator grid is neutralized by electron emission from a U-shaped 0.019-in. -diam tungsten wire heated to thermionic emission temperature and immersed in the beam.

Seven power supplies are used to furnish power to the engine. Three of the supplies, providing voltages referenced to the voltage level of the anode, are the magnetic field supply, the cathode heater supply, and the anode-cathode supply. The positive and negative high voltage supplies and the neutralizer bias supply are referenced to laboratory "ground." The neutralizer heater supply is referenced to the positive side of the neutralizer bias supply. The direct-current supplies are not regulated but are filtered to the extent that ripple voltage is one percent or less at usual operating levels.

The engine was mounted in a 15-in.-diam, glass, bell-jar pipe section which was evacuated, through a 20-in. gate valve, by a 20-in. oil diffusion pump (Fig. 3). A 3-hp mechanical pump was properly valved to serve as either a roughing pump or finishing pump. The diffusion pump was fitted with a refrigerant-cooled baffle to minimize backstreaming of diffusion pump oil. Prior to operation of the engine, the bell jar was evacuated to approximately 7×10^{-4} torr. During operation of the engine, the bell-jar pressure was about 1×10^{-5} torr for an argon propellant flow rate of 0.09 atmospheric cc/sec.

4.3 EVALUATION OF ENGINE PERFORMANCE

4.3.1 Gas Distributor Performance

The gas distributor consists of a flat, 2-5/8-in.-diam stainless steel plate with nine symmetrically spaced 1/4-in.-diam holes centered on a 5/8-in. radius. The cathode support rods are brought through a 3/4-in. by 3/8-in. hole at the center of the distributor. Observance of the sputtering pattern on the accelerator reveals that the beam current density is at a maximum at the center of the accelerating area, contrary to the optimum situation of constant beam current density over the entire accelerating area. The through-feed propellant introduction method, and hence nonoptimum design of the gas distributor, is felt to be the principal cause of the unfavorable beam current density distribution. Propellant introduction at the periphery of the ionization chamber would probably improve ionization chamber performance as well as result in a more uniform beam current

density distribution (Ref. 14). However, for the intended purpose, the ion engine with simple through-feed propellant introduction has been found to be satisfactory.

4.3.2 Magnetic Field Characteristics

The axial magnetic field is produced by current flowing through a solenoidal winding of 22 double turns of American Wire Gage (AWG) No. 16 enameled copper wire. The windings are supported by electrically insulating forms machined from hydrous aluminum silicate. After heat treatment, the aluminum silicate has a melting point of 2912°F and a dielectric strength of 80 v/mil.

Magnetic field windings providing a downstream-to-upstream magnetic field-strength ratio of approximately 0.6 (field at screen/field at distributor) produce a better ionization chamber efficiency than that resulting from a uniform field (Ref. 15). A map of the magnetic field strength along the axis of the anode in the region from the gas distributor to the screen is shown in Fig. 22 for several values of coil current. From Fig. 22, it can be seen that the magnetic field strength ratio for the several coil currents is about 0.5, which is adequate for proper operation of the engine.

The magnetic field strength for the most efficient ionization chamber operation was determined experimentally. It was found that a coil current of 15 amp resulted in the most efficient ionization chamber performance. Coil currents greater than 15 amp yielded negligible increases in ionization chamber efficiencies, but overall engine power efficiency dropped rapidly because of the added power dissipated in the field coil. The engine is usually run with a coil current between 12 and 15 amp.

4.3.3 Ionization Chamber Performance

The ionization chamber is 5.4 cm in diameter with a length-to-diameter ratio of 0.95. The ionization chamber efficiency is generally defined as the energy dissipated in the chamber per beam ion. To accurately determine this efficiency one must account for anode collection of the electrons arising from the ionization process. The magnitude of the collected electron current, attributable to the ionization process, has been found to be about the same as the ion beam current. The ionization chamber efficiency is then defined as the product of the ionization chamber potential difference and total anode current minus beam current (Ref. 16). However, using the wiring and meter arrangement as shown in Fig. 21, it was possible to read total anode current minus beam current directly. It would have been informative to measure the cathode

emission current and the current drain to the screen and propellant distributor, but this is not essential for determining the ionization chamber efficiency and hence was not done in the present series of experiments.

The curves indicating the ionization chamber efficiency, for this particular ion engine, are shown in Fig. 23. The energy per beam ion is plotted against ionization chamber potential difference for a constant beam current and a constant magnetic field strength. Data for the lower ionization chamber potential differences were inconsistent. The reason is that the ionization cross section for argon decreases, resulting in arc instability and extinguishment of the anode-cathode discharge. The ionization chamber efficiencies, in these experiments, compare favorably with those reported for NASA experimental and flight model engines (Refs. 9 through 16).

A factor affecting the probability of ionization by the primary electrons, emitted by the cathode, is the density of the neutral propellant in the chamber. No means was provided in this investigation to measure ionization chamber pressure although the propellant flow rate was accurately measured with a calibrated orifice. An indication of the dependence of ionization chamber efficiency upon propellant density and anode-cathode potential difference can be obtained experimentally by plotting chamber efficiency as a function of potential difference, with propellant flow rate as parameter, while holding the beam current constant. These data are shown in Fig. 24. It can be seen that flow rates between 0.09 atmospheric cc/sec and 0.23 atmospheric cc/sec result in essentially identical efficiencies. No data were taken for flow rates greater than 0.23 atmospheric cc/sec. The engine is usually run at a propellant flow rate of 0.05 atmospheric cc/sec, which yields a reasonable chamber efficiency while maintaining an acceptable propellant utilization efficiency. Propellant utilization efficiency is defined as:

$$\eta_u = \frac{J_B}{J_{NE}} \times 100 \text{ percent} \quad (4.1)$$

4.3.4 Cathode Performance

The cathode for all the data presented in this report consisted of a U-shaped 0.019-in.-diam, 1-1/4-in.-long tungsten wire. The cathode filament was found to be a major limiting factor determining engine lifetime. A cathode lifetime of about 20 hr with beam currents up to 40 ma was experienced. All cathode failures have been the result of mechanical shock with resultant parting of the brittle tungsten wire, rather than caused by electrical burnout. One experiment, of 1/2-hr duration, was performed using a barium-oxide-coated, 0.019-in.-diam tungsten wire placed inside

a tightly wound spiral of 0.005-in.-diam tungsten wire. No binder was added to the oxide, and unexplained anode-cathode arcing (not observed with tungsten wire cathode) resulted in rapid loss of the oxide. However, for a specific setting of engine operating parameters, the heater power required by the oxide-coated cathode was about 40 percent lower than that for the plain tungsten wire cathode. A properly designed, oxide-coated cathode should substantially increase the cathode lifetime as well as the overall engine power efficiency.

Considering small changes of the various engine operating parameters, about a stable operating point, the magnitude of beam current is most sensitive to changes in neutral propellant flow and cathode heater power. The experimentally determined interrelationship between beam current, neutral flow rate, and cathode heater power is shown in Fig. 25. There is an inherent error in these data because of the presence of multiple charged beam ions. A perusal of data showing the percentage of multiple charged argon ions as a function of bombarding electron energy shows that this error is probably less than 10 percent (Ref. 17). From Fig. 25 it can be seen that the propellant utilization efficiency is not as high as might be desired, but is adequate for ion beam diagnostic experiments and development of engine operation monitoring techniques. The propellant utilization efficiency has been found to increase with the mass of the propellant particles, and improved performance should be observed with xenon, cesium, or mercury. A propellant utilization efficiency of about 1 percent was noted using hydrogen.

4.3.5 Accelerator Performance

The electrostatic accelerator consists of two flat stainless steel plates match drilled with 3/16-in.-diam holes. The centers of the holes are set at the apex of equilateral triangles with 0.254-in. sides. The screen plate is held at a high positive potential and the accelerator plate is held at a negative potential; both potentials are referenced to laboratory "ground." The screen and accelerator are mechanically spaced and electrically insulated by small aluminum oxide spheres. The maximum engine run time for beam currents 40 ma and less is limited to about 15 hr because of electrical breakdown across these spacers as the result of contamination by sputtered stainless steel particles. This problem could easily be solved by a somewhat more complicated mechanical design of the screen and accelerator (Ref. 10) such that there is no line-of-sight path from the screen-accelerator space to the spherical insulators.

Accelerator plate impingement is largely determined by acceleration system optics and charge exchange collisions of beam ions with neutrals in the interelectrode space (Ref. 18). For the present case, accelerator

plate impingement was only about 2 percent of the beam magnitude for beam currents up to 40 ma and test cell background pressures of about 1×10^{-5} torr. This low level of impingement at these magnitudes of beam current has presented no accelerator plate and engine lifetime problems.

For steady-state laboratory operation of a well-neutralized beam at low background pressure ($< 1 \times 10^{-5}$), beam divergence is principally determined by accelerator system optics (Ref. 19). Beam divergence is an important measure of accelerator system performance since divergence adversely affects the thrust output of an ion engine.

Radial ion beam density profiles and beam divergence were obtained with an impingement-type probe similar to that described in Ref. 1. The probe and associated circuitry, shown schematically in Fig. 26, permits operation of the probe as an electron emissive probe for plasma potential measurements as well as for ion beam density measurements. To measure ion beam density, the probe heater current was set at a value sufficient to maintain a clean probe surface but below the thermionic emission threshold. The probe was then biased negatively to repel electrons, and the ion beam impingement current to the probe was indicated on a microammeter. Radial beam current density profiles recorded at three axial positions in the beam are presented in Fig. 27. From these data it can be seen that the half-angle beam divergence is about 17 deg for the particular accelerator system conditions stated and a background pressure of about 2×10^{-5} . This value of beam divergence is somewhat greater than the 10-deg divergence quoted in Ref. 20 for a 20-cm ion engine; however, no further attempts were made to optimize accelerator optics. The dips in the density profiles at the geometric center of the beam emitting area are thought to be caused by the physical presence of the cathode and relatively reduced degree of ionization along the centerline of the ionization chamber. This results in a reduced beam current at the centerline relative to the two maximum peaks adjacent to the centerline. Only relative indications of the ion beam density are quoted for this impingement probe because of the V_ϕ and temperature dependent electron emission effect which was previously discussed in Section II.

4.3.6 Neutralizer Performance

One measure of the effectiveness of an ion engine neutralizer is the magnitude of the potential which the beam is forced to attain to extract sufficient electrons from the neutralizer, when all other sources of neutralizing electrons have been effectively eliminated (Ref. 20). For this particular ion engine the neutralizer consisted of a U-shaped, electrically heated 0.019-in.-diam tungsten wire and was normally

biased at a positive level to prevent electron flow to surrounding equipment at "ground" potential. The neutralizer was placed 3/4 in. downstream from the accelerator.

The cooled copper baffle used to reduce diffusion pump oil back-streaming from the diffusion pump was initially used to terminate the ion beam; an electrically floating stainless steel plate was used later. It was originally planned to depend on secondary electron emission from the copper baffle for neutralization of the ion beam during initial checkout of the engine. However, after several hours of engine operation, the baffle became coated with a grease-like substance which reduced the supply of secondary electrons to the point that a neutralizer was required for stable operation of the engine. The grease-like substance is apparently the cracking product of diffusion pump oil that is subjected to energetic charged particle bombardment. Under this condition of ion beam termination, the magnitude of the neutralizer electron emission current was essentially the same as the ion beam current, and plasma potential measurements, referenced to laboratory "ground," follow closely the positive bias on the neutralizer. Although this method of ion beam termination and resultant neutralizer evaluation is less desirable than using an electrically floating metal collector, it was considered adequate for a preliminary evaluation of neutralizer effectiveness.

Measurements of plasma potential were taken with an electron emissive probe similar to that described in Refs. 1, 2, and 3 and shown schematically in Fig. 26. With the probe filament heated to emit an electron current much greater than the collected "Langmuir" electron current for the probe bias range of interest, increases in probe bias produce a potential at which total probe current is zero. The probe bias for zero probe current is taken as an indication of mean plasma potential at a particular probe position and is estimated to be accurate within 1.5 v. A more accurate determination of plasma potential can be made with the emissive probe but for an initial evaluation of neutralizer effectiveness, the 1.5-v accuracy is considered sufficient. A reasonable criterion for assessment of neutralizer effectiveness is that the potential difference between the neutralizer and plasma be 15 v or less (Ref. 1).

The first neutralizer configuration to be investigated consisted of two U-shaped tungsten filaments each immersed 3/4-in. into the beam and diametrically positioned along a diameter of the 5-cm-diam beam emitting area. Radial profiles of plasma potential taken at two axial distances from the accelerator are shown in Fig. 28. As can be seen from these data, the use of two neutralizer filaments resulted in slightly more effective neutralization of the ion beam than when only one neutralizer was used.

According to the effectiveness criterion above, however, the slight advantage of two-neutralizer operation is of academic interest only.

Erosion of the neutralizer caused by sputtering limited its lifetime to about 20 hr for 2000-ev beam particles and beam currents up to 40 ma. An effort was made to increase the neutralizer lifetime by placing the neutralizer at the edge of the beam emitting area to reduce the sputtering damage. The lifetime increased slightly but the neutralization effectiveness decreased as indicated by an increased plasma potential throughout the beam.

An axial plasma potential profile was plotted for two neutralizer wires immersed 1/4 in. into the beam emitting area and diametrically positioned. This was compared with an axial profile obtained using two neutralizers immersed 1 in. into the beam, also diametrically positioned. Each axial profile was taken with the probe located on a line leading from the geometric center of the beam emitting area. The axial potential profiles are shown in Fig. 29. From these data, it can be seen that closer electrical coupling of the neutralizer with the ion beam is effected by deeper neutralizer immersion. Except for the lifetime problem, the simple immersed wire neutralizer is deemed satisfactory for ion beam diagnostic investigations. However, the a-c voltage gradient across the neutralizer wire caused by the heating current does modulate the magnitude of the plasma potential. This modulation necessitates interpretation of the data so that mean values for slow time response plasma potential probes are obtained or the use of fast response probe circuitry for more definitive plasma potential data.

4.3.7 Overall Engine Power Efficiency

Heat radiation is the primary mechanism for cooling of the engine, with the equilibrium temperature of the engine being functionally dependent on the magnitude of the beam current. Operation of the engine at a beam current level of 100 ma resulted in an engine temperature sufficient to cause melting and electrical breakdown of several nylon insulators and limited stable operation of the engine to less than 1 min. However, operation at beam currents of 40 ma and less allowed stable operation of the engine for several hours. An improvement in this engine would be replacement of the nylon insulated feedthroughs with ceramic insulated feedthroughs. Slight warping of some engine parts has also directed attention to the advisability of engine operation at the most efficient setting possible for a certain beam power. The overall engine power efficiency is defined as:

$$\eta_p = \frac{V_I I_B}{V_I I_B + \Delta V_{II} I_I + \Delta V_{MI} I_M + \Delta V_{FI} I_F + (V_I + V_A) I_A} \quad (4.2)$$

The relationship of overall engine power efficiency as a function of anode-cathode potential difference is shown in Fig. 30. The decreasing efficiency with increasing anode-cathode potential difference is mainly caused by increasing anode-cathode discharge losses since the magnetic field loss, the accelerator drain loss, and the beam power are all practically constant and the cathode heater power loss varies only slightly. The engine is usually run at the lowest anode-cathode potential difference possible for a certain neutral propellant flow rate. The magnetic field loss at 12-amp coil current is 48 w, and the use of a permanent magnet system, such as discussed in Ref. 15, would eliminate this power loss completely. For the data of Fig. 30, the mean cathode heater power is 69.3 w. A properly designed oxide-coated cathode could reduce this loss by at least 40 percent. With these improvements, this ion engine could readily achieve an overall power efficiency of 50 percent at 40 ma beam current and 2000 v net acceleration. Higher efficiencies are noted for higher beam currents and higher net accelerating voltages.

The maximum specific impulse that was obtained with this engine was 4500 sec at a thrust level of 2.7×10^{-3} newtons where specific impulse is expressed as

$$I_{sp} = \eta_u \frac{\bar{V}}{g} \quad (4.3)$$

and \bar{V} is:

$$\bar{V} = 2 \frac{e}{m} V_I \quad (4.4)$$

The thrust was calculated using the following expression

$$T_h = 2 \frac{m}{e} V_I I_B \quad (4.5)$$

4.4 CONCLUSIONS

An economically constructed laboratory-type ion engine was found adequate for ion beam diagnostic investigations and development of ion engine operation monitoring procedures for extended periods of testing.

The experimental arrangement consisting of an ion engine and associated power supplies with a bell-jar vacuum system provides a system capable of rapid installation, checkout, and removal of ion beam diagnostic devices with several bleedup and pumpdown cycles of the vacuum system being possible in one day.

The performance characteristics of the engine reveal operating parameters realistically approximating those of flight model electron

bombardment ion engines. The unit has the attractive capability of operation with virtually any propellant gas or vapor compatible with the engine materials.

SECTION V LATERAL ION PROBE

5.1 INTRODUCTION

Another source tending to reduce the efficiency of an operating ion engine stems from the acceleration of ions in a direction normal to the exhaust axis. Since these laterally or transversely directed ions, that are present because of grid misalignment, produce no useful thrust they should be minimized to yield optimum engine operation. It is for this reason that an ion probe was developed to measure these laterally or transversely directed ions.

When an object is immersed in a highly energetic, highly ionized exhaust beam, a wake of charged particles is produced. The charge distribution of this wake was evaluated and found to consist of randomly moving ions in a direction predominantly normal to the engine exhaust axis, and measurements were made to ascertain their velocity component normal to the exhaust. The measurements were made by inserting a guard-ring Langmuir probe (Ref. 17) into a plasma stream, and the probe current was measured as a function of variations in probe voltage. A characteristic plot of this relationship is shown in Fig. 31. Plotting the logarithm of the probe current as a function of the probe voltage resulted in essentially a straight line curve. This is shown in Fig. 32. In view of the straight line region of the logarithmic plot in Fig. 32, it may be shown that the electrons having Maxwellian distribution and their temperatures may be determined from the slope of the line. The equation to be used for ascertaining the temperature is:

$$N_e = N_0 \exp \left(-\frac{E\phi}{kT} \right) \quad (5.1)$$

The average velocity of the particles may be calculated, and they are found to be greater (1×10^6 m/sec) than the directed velocity (8.7×10^4 m/sec) of the ions determined from the known accelerating potential.

5.2 EXPERIMENTAL APPARATUS

The charge distribution behind the wake of an object placed in a highly energetic, highly ionized plasma was measured with a Langmuir

probe located behind a circular disk. A plane guard-ring-type Langmuir probe was constructed of brass to obtain the volt-ampere characteristics at various positions behind the disk. The probe and the disk were biased at various potentials so that charge distribution profiles behind the disk could be obtained.

The plane area of the probe exposed to the beam was 0.052 in. in diameter, the guard-ring was 0.191 in. in diameter with a hole placed in the center approximately 0.67 in. in diameter. Both the probe and guard-ring, mounted in a boron-nitride housing, were electrically insulated from each other and in such a way that the voltage on both probe and guard-ring could be individually controlled. The probe was mounted rigidly to the spool piece coupling the valve and the bell-jar experiment housing. The experiment is shown in Fig. 33. Mounted above the probe was a movable shield composed of a 1/2-in.-diam wafer of thin stainless steel. The shield could be moved both horizontally and vertically. The vertical position was indicated by a pointer appended to the movable carriage which moved along a 6-in. steel scale glued directly to the brass dovetail traverse. The horizontal position was indicated by the use of a dial indicator (accuracy of ± 0.0005 in.) from which the shield was directly mounted so that very little, if any, error would be introduced from any of the powering devices such as the worm gear. The traversing system was driven by small d-c motors; the horizontal motor has a speed of approximately 6 rpm, and the vertical motor a speed of approximately 80 rpm.

For the acquisition of volt-ampere characteristics, the electronic apparatus shown in Fig. 34 was employed. The current from the probe passed through a 200-ohm precision resistor. Each side of the resistor was connected to the inputs of a difference amplifier. The output of the difference amplifier was then fed to the y coordinate of an x-y plotter. The saw-tooth generator was used to bias a probe. It was also used to drive the x coordinate of the recorder.

The guard ring was connected to an isolation amplifier which permitted a current no larger than 10^{-9} amp to flow through the amplifier onto the saw-tooth voltage sweep. By means of this device it was possible to hold the guard ring and the probe at the same potential and did not permit any appreciable amount of guard-ring current to be recorded.

5.3 EXPERIMENTAL PROCEDURE

From Fig. 31 it is seen that the probe current remains essentially constant from about 4.0 v (as the probe voltage is decreased). Therefore, the probe was operated at approximately 0 v so that the positive ion current could be measured. Previous data indicated that the floating potential,

or the neutralizer bias, was approximately 6.0 v. Therefore, for each space positioning of the shield the data are recorded at both of these bias potentials before the shield is moved to another position. Figure 35 shows the experimental arrangements used in acquiring probe current data as a function of the horizontal positioning of the shield with respect to the vertical shield position (the probe bias and the shield voltage were held constant for each series of runs). Two biases were placed upon the probe at ground potential and also at 6 v. Since previous experience indicates that a negligible difference in the amount of current collected within this range existed at the small applied bias potential voltages, the use of a floating guard ring was justified. The engine was operated at a positive potential of approximately 1.6 kv, and the negative supply was approximately -400v. The magnet current was 12 amp, the anode potential was 75 v, and the neutralizer current was 16 amp. The cathode filament was heated to such a level that the positive ion current reading (the probe held at 0 v) was approximately 2.6 to 2.7 μ amp. A negative current (probe held at 0 v) of approximately 3 μ amp was measured when the shield was displaced at the bottom-most position and moved to the side so that the probe would not be obstructed from the beam. At the time of measurement, no voltage was applied to the shield.

From Fig. 36 it may be seen that any small variation in heater current to the neutralizer produced only an imperceptible change in electron current to the probe. This is true since the neutralizer current, at this value, is spacecharge limited. Argon gas was used in these experiments and the flow rate was approximately 8×10^{-5} gm/sec since at this flow rate the most stable beam characteristics were obtained. The total beam current under these conditions was approximately 10 ma.

5.4 RESULTS AND DISCUSSION

The positive charge distribution of a wake at various increments downstream from the source is shown in Figs. 37 through 41. In evaluating these and subsequent data it must be borne in mind that the probe was finite in size, and as the shield passed in front of the probe the amount of current collected behind the edge of the shield would be distorted in such a manner as shown in Fig. 42. That is, a virtual void of positive charged particles existed in the region immediately behind the disk and developed into a conical-shaped void filling behind the disk.

For a potential of 0 v upon the shield, the charged particle density in the wake increases in a smooth transition from a region of essentially no positively charged particles at a position of 0.1 in. behind the probe

(Fig. 37) to the distribution shown in Fig. 41 for a shield which is displaced approximately 4.1 in. from the probe. The negative potentials (-50 and -100 v) were applied to the shield. The apex angle of the charged particle conical void increased as was expected. The potential contour plots are shown in Figs. 43, 44, and 45. Figures 46 through 50 show the results of the measurements taken with the probe biased at 6 v and at 0 v. Figures 46 and 47 show a fairly symmetrical pattern for all three shield biased voltages; however, in Figs. 48, 49, and 50 only a semblance of the symmetrical pattern for the case of 0 v upon the shield is shown, and in all other cases the essentially completely random pattern is experienced. The data from the two sets of current readings were subtracted and the results were plotted in Figs. 51, 52, and 53. From these figures a rather symmetric pattern is indicated, especially for the case of a shield bias potential of 0 v, and in the case of -50 and -100 v a much more symmetrical pattern is observed than those in the curves plotted from the data taken with approximately 6 v biased upon the probe. From Figs. 51 and 53, it can be seen that an electrogasdynamic wake was detected with the experimental apparatus, bearing out qualitatively the theoretical predictions.

5.5 CONCLUSIONS

The charge distribution in the region behind a body placed in a high velocity, low density, highly ionized plasma was analyzed by means of a guard-ring Langmuir probe, and it was determined that an electrogasdynamic wake existed. Furthermore, by making use of the variation in the positive charge particle distribution in a given spatial region of this wake, and by correlating this variation with theory or by means of an independent experiment to determine the "lateral" random ion velocity, a material probe can be developed to directly indicate the "lateral ion temperature" of the plasma.

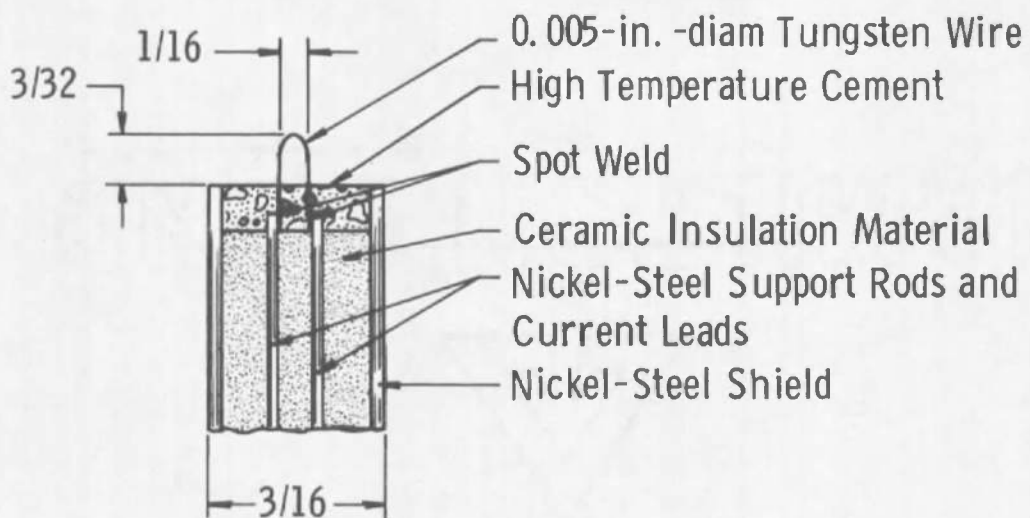
REFERENCES

1. Sellen, J. M., Jr., Forbes, S. G., and Kemp, R. F. "Advanced Ion Beam Diagnostic Techniques." ARS Paper 2067-61, October 1961.
2. Kemp, R. F., Sellen, J. M., Jr., and Pawlik, E. V. "Neutralizer Tests on a Flight-Model Electron-Bombardment Ion Thrustor." NASA TN D-1733, July 1963.

3. Davis, J. W., Walch, A. P., Meyenard, Salz, F., and Lary, E. C. "Theoretical and Experimental Description of the Oscillating Electron Ion Engine." United Aircraft Corporation. IAS-ARS paper 61-103-1797, July 1961.
4. Sellen, J. M., Jr. "Investigation of Ion Beam Diagnostics." Prepared for NASA under Contract NAS 8-1560.
5. Kemp, R. F., and Sellen, J. M., Jr. "Plasma Potential Measurements by Electron Emissive Probes." The Review of Scientific Instruments, Vol. 37, No. 4, April 1966.
6. Handbook of Chemistry and Physics; published by The Chemical Rubber Publishing Company, April 1962, p. 3044.
7. Johnson, E. O. and Malter, L. "A Floating Double Probe Method for Measurements in Gas Discharges." Physical Review, Vol. 80, No. 1, October 1950, p. 58.
8. Dickson, L. D., "Survey of Diagnostic Techniques Used to Determine Temperature and Density in Plasmas." TR AF-95 (AD 275 762) The Johns Hopkins University Radiation Laboratory, Baltimore, Maryland, May 1962. Contract AF 33(616)-6753.
9. Reader, Paul D. "Scale Effects on Ion Rocket Performance." ARS Journal, Vol. 32, No. 5, May 1962.
10. Kaufman, H. R. "An Ion Rocket with an Electron-Bombardment Ion Source." NASA TND-585, January 1961.
11. Nakanishi, Shigeo, Pawlick, E. V., and Baur, C. W. "Experimental Evaluation of Steady-State Control Properties of an Electron-Bombardment Ion Thrustor." NASA TND-2171, February 1964.
12. Pawlick, E. V. and Nakanishi, Shigeo. "Experimental Evaluation of Size Effects on Steady-State Control Properties of Electron-Bombardment Ion Thrustors." NASA TND-2470, September 1964.
13. Kerslake, William R. and Pawlick, Eugene V. "Additional Studies of Screen and Acceleration Grids for Electron-Bombardment Ion Thrusters." NASA TND-1411, August 1963.
14. Reader, Paul D. "Experimental Effects of Propellant-Introduction Mode on Electron-Bombardment Ion Rocket Performance." NASA TND-2587, January 1965.

15. Reader, Paul D. "Ion Rocket with a Permanent Magnet." Astronautics & Aerospace Engineering, Vol. I, October 1963, pp. 83-85.
16. Reader, Paul D. "Investigation of a 10-Centimeter-Diameter Electron-Bombardment Ion Rocket." NASA TND-1163, January 1962.
17. Stuber, Fred A. "Multiple Ionization in Neon, Argon, Krypton and Xenon." The Journal of Chemical Physics, Vol. 42, No. 8, April 15, 1965, pp. 2639-2643.
18. Kerslake, William R. "Charge-Exchange Effects on the Accelerator Impingement of an Electron-Bombardment Ion Rocket." NASA TND-1657, May 1963.
19. Sellen, J. M. and Kemp, R. F. "Cesium Ion Beam Neutralization in Vehicular Simulation." AFOSR-937. Presented to Joint Meeting of the National IAS-ARS, Los Angeles, June 13-16, 1961.
20. Pawlik, Eugene V. "An Experimental Evaluation of Array of Three Electron - Bombardment Ion Thrustors." NASA TN D-2597, January 1965.
21. McKinney, Charles Wesley. "An Investigation of the Properties of the Wake of a Body in a Flowing Plasma and Their Potential as a Lateral Ion Temperature Indicator." Master's Thesis, University of Tennessee Space Institute, December 1965.

**APPENDIX
ILLUSTRATIONS**



Dimensions in Inches

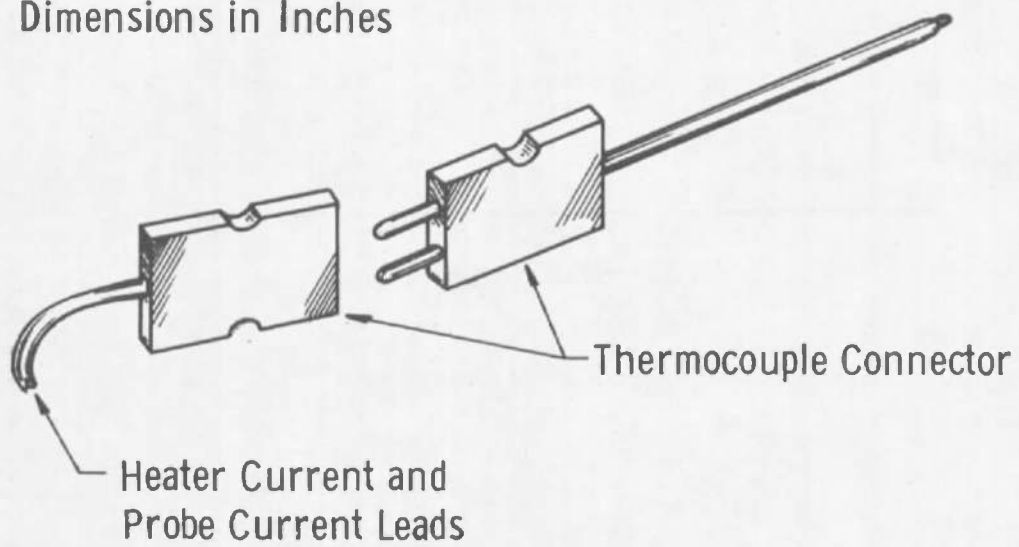


Fig. 1 Emissive Probe Construction Details

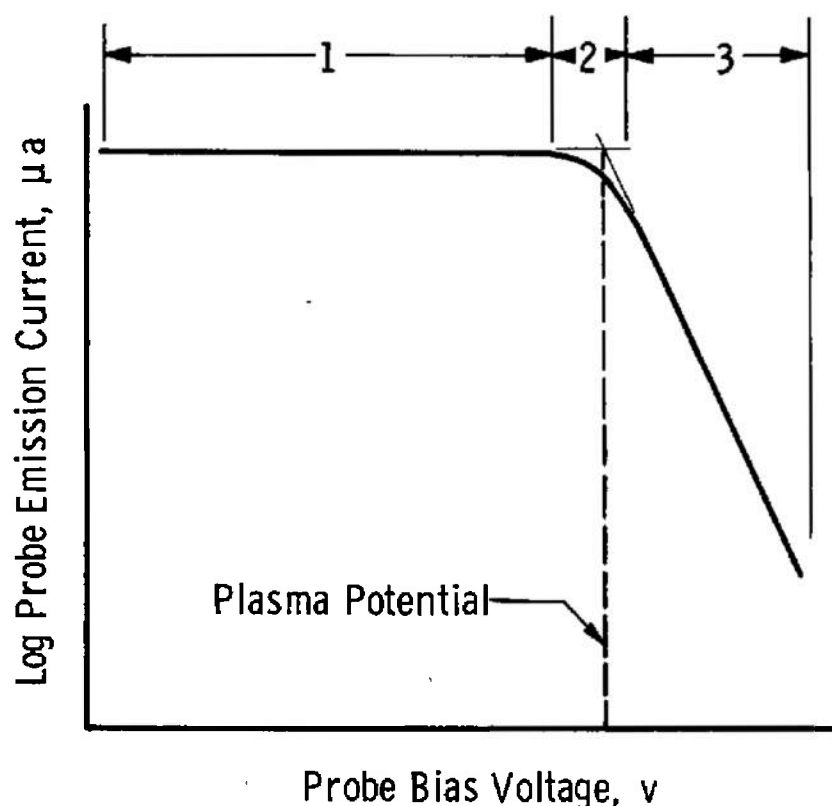


Fig. 2 Ideal Emissive Probe Characteristic

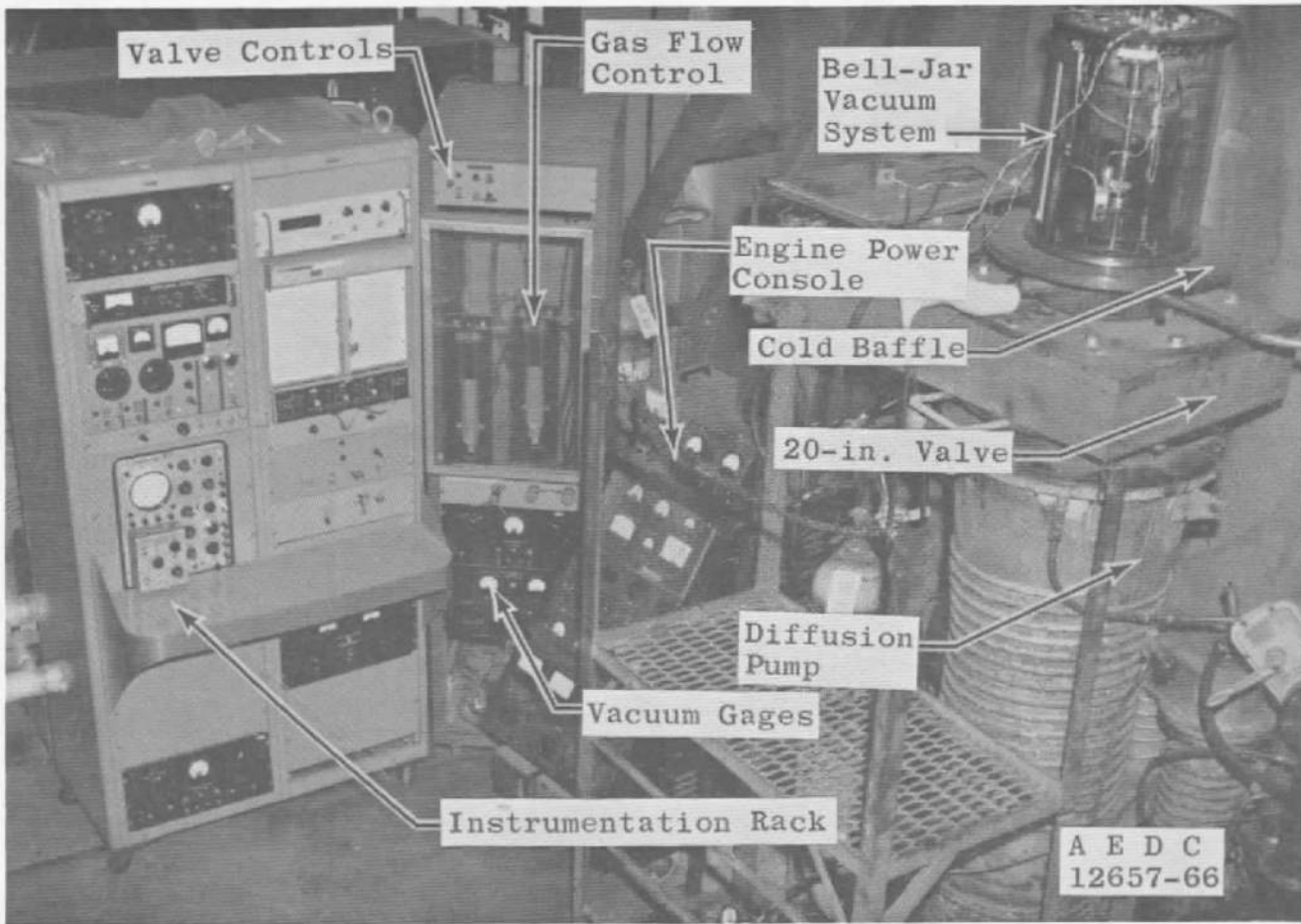


Fig. 3 Vacuum System, Engine Power Supply, Instrumentation Rack, and Related Equipment

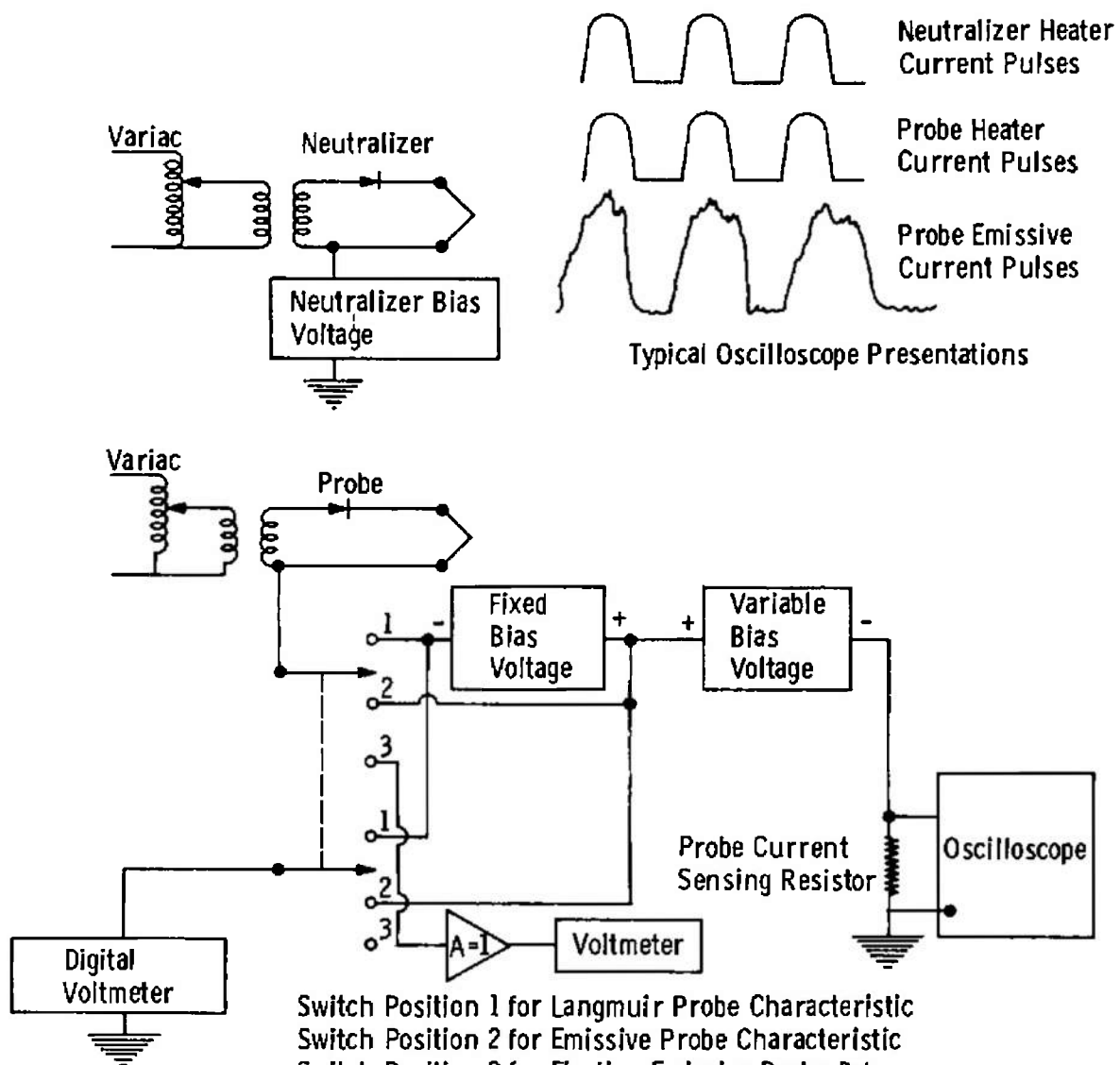


Fig. 4 Circuitry for Obtaining Langmuir and Emissive Probe Characteristics

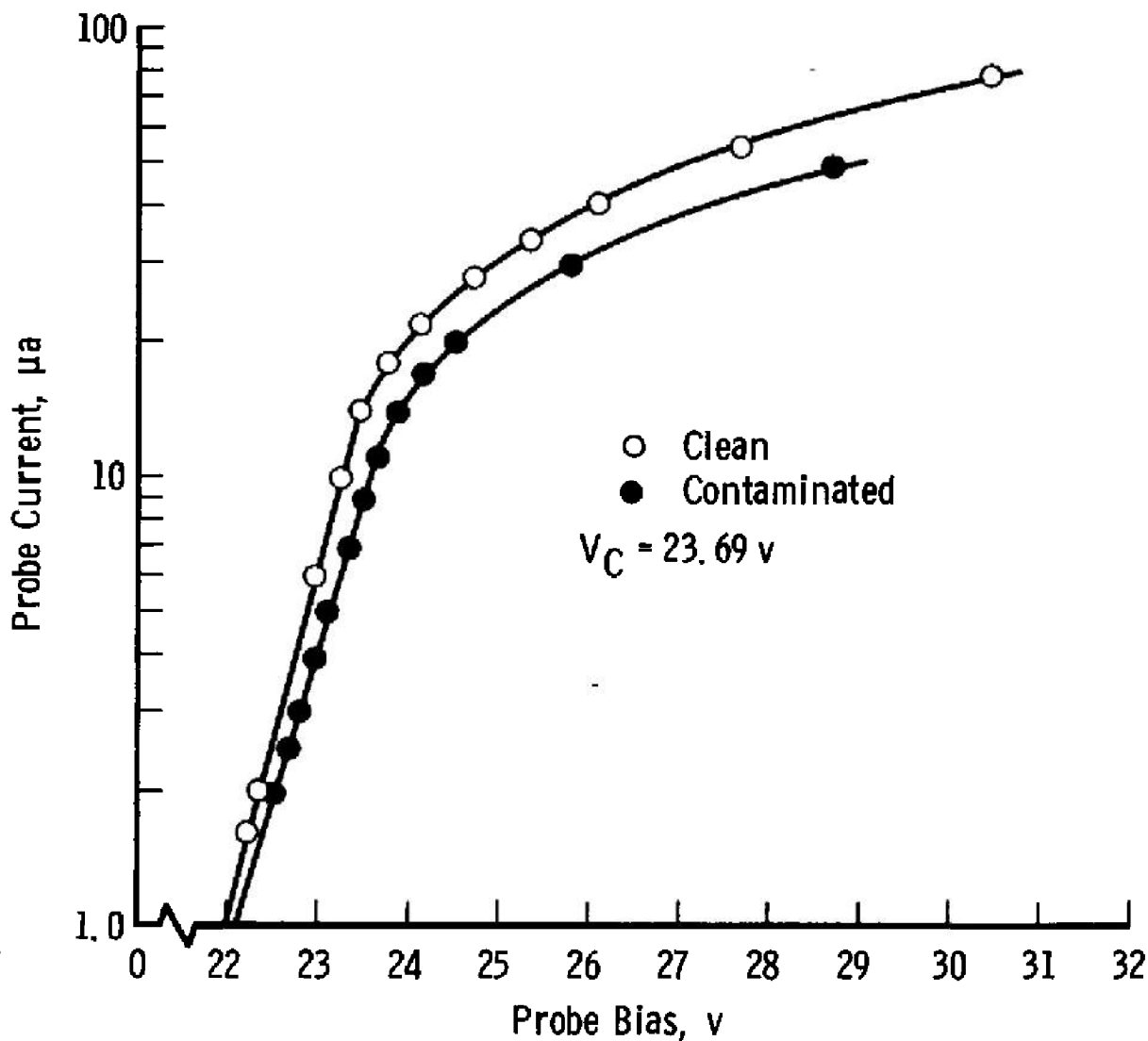


Fig. 5 Comparison of Langmuir Probe Characteristics, Contaminated and Clean

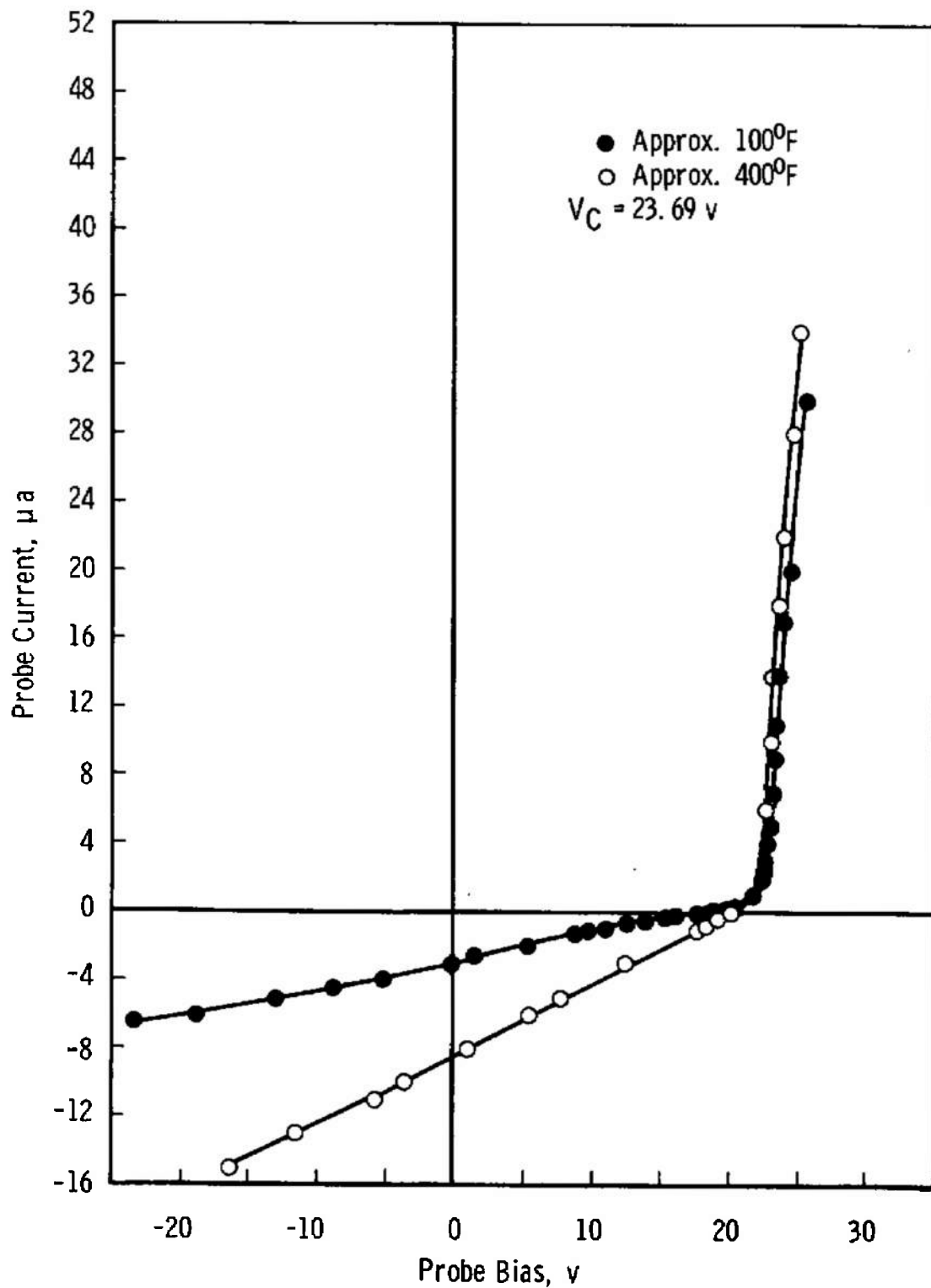


Fig. 6 Langmuir Probe Characteristics (Temperature Effects)

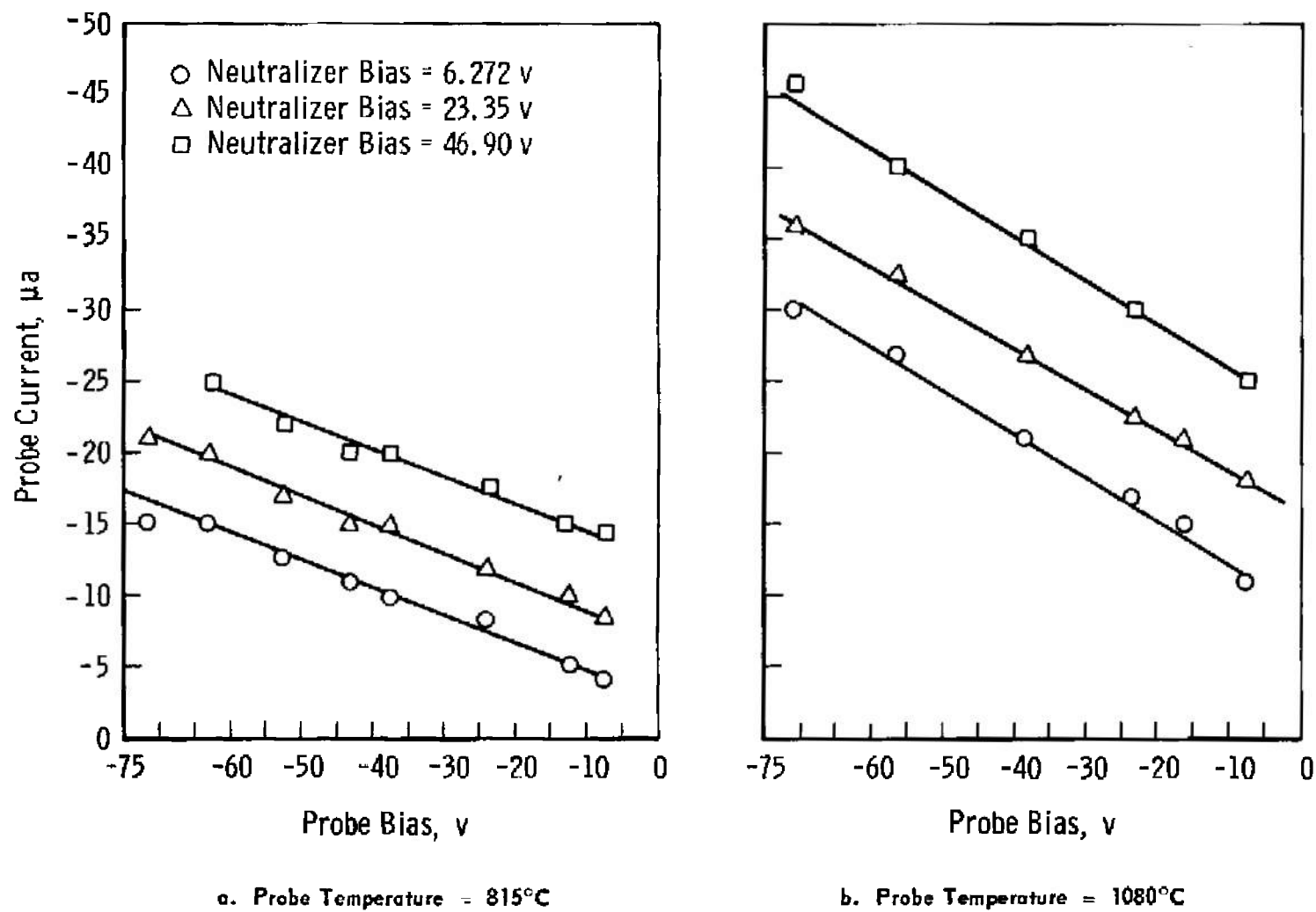
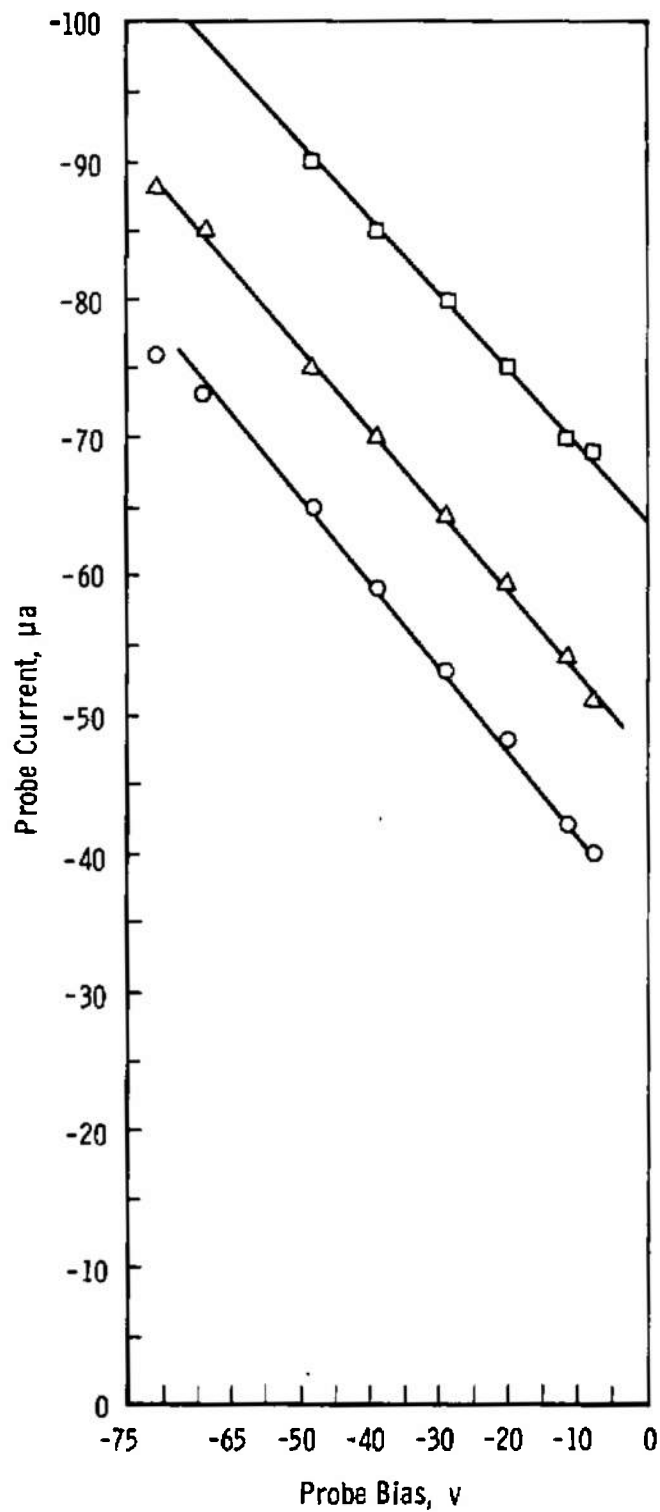


Fig. 7 Effect of Temperature and Total Accelerating Voltage on Emissive Probe Current



c. Probe Temperature = 1800°C

Fig. 7 Concluded

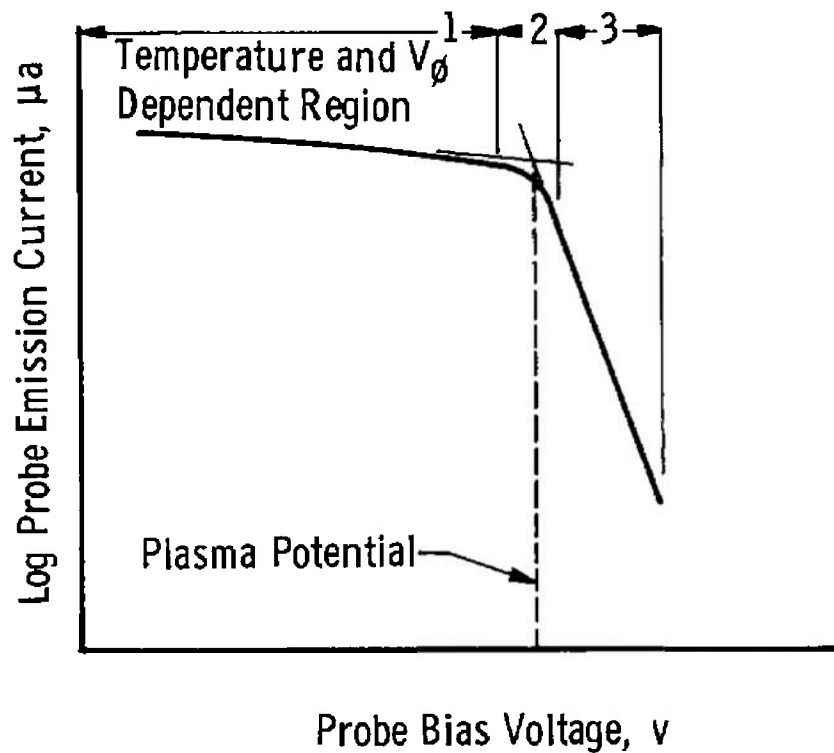


Fig. 8 Emissive Probe Characteristics

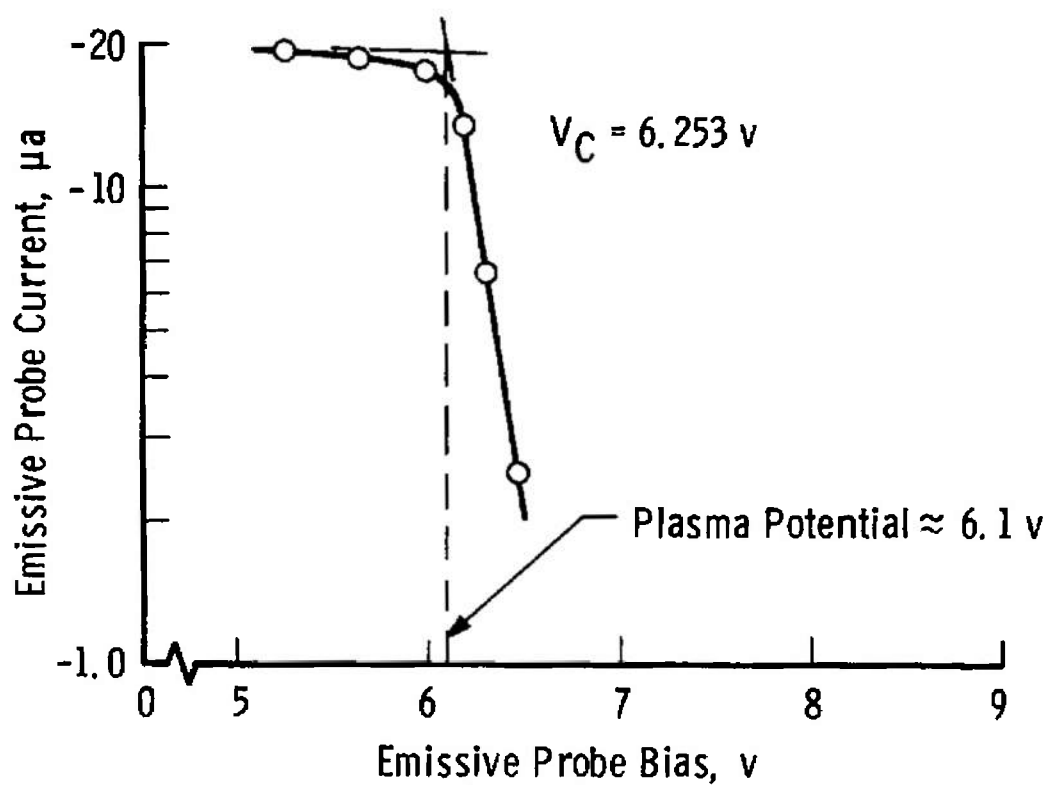
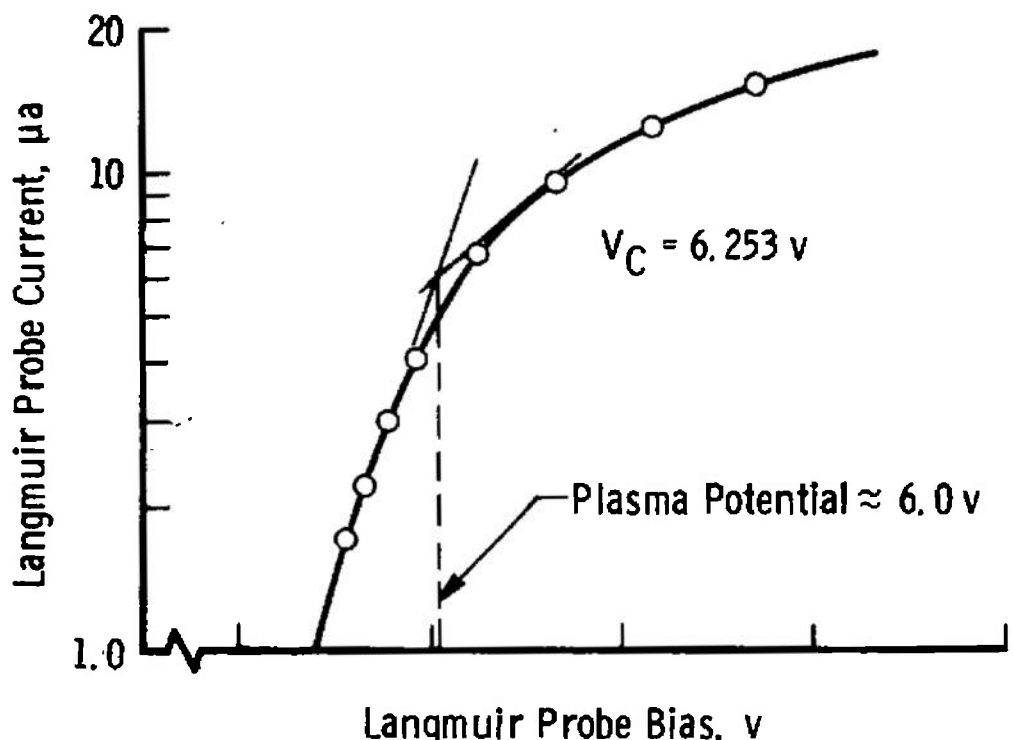


Fig. 9 Comparison of Langmuir Probe and Emissive Probe Indications of Plasma Potential

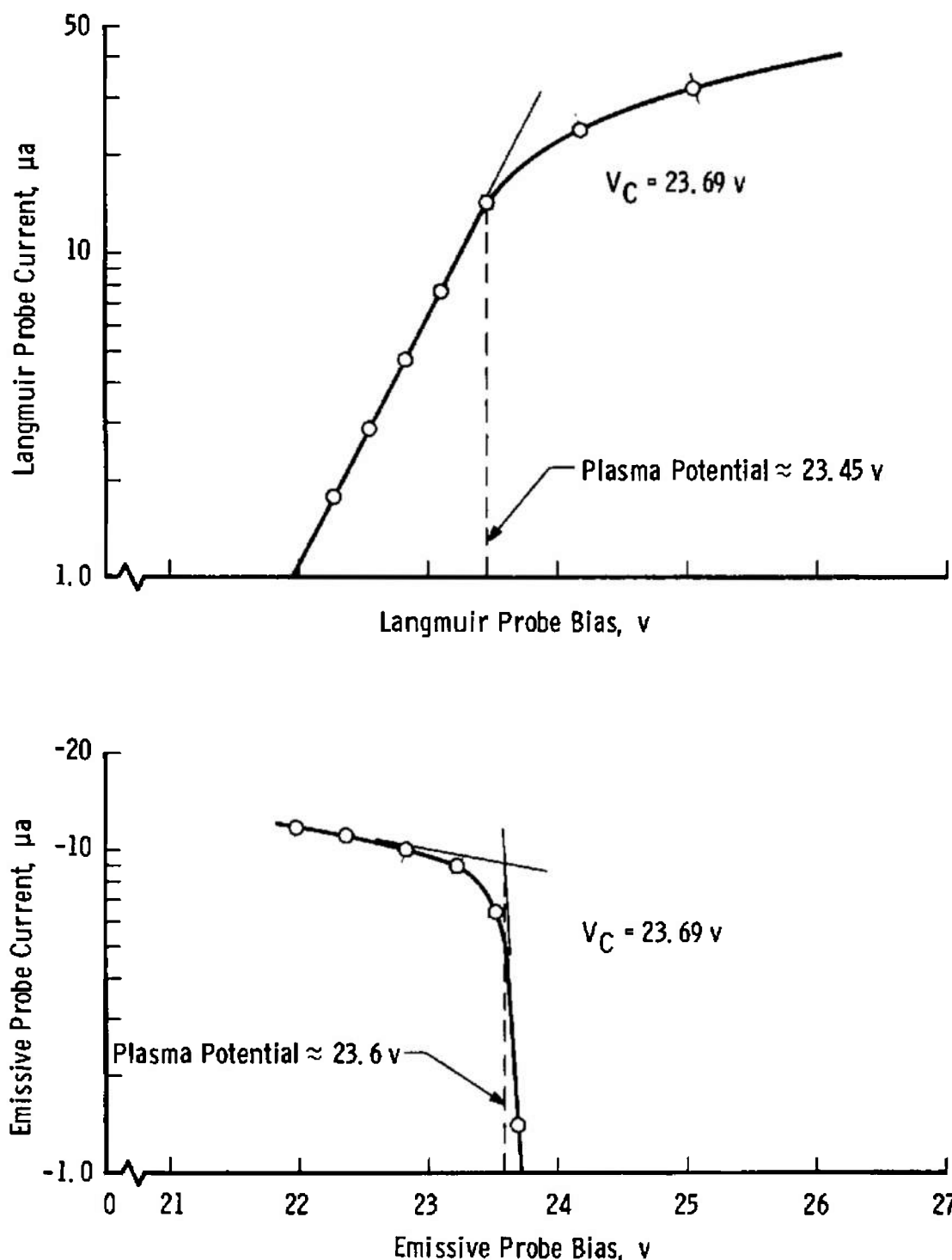


Fig. 10 Comparison of Langmuir Probe and Emissive Probe Indications of Plasma Potential

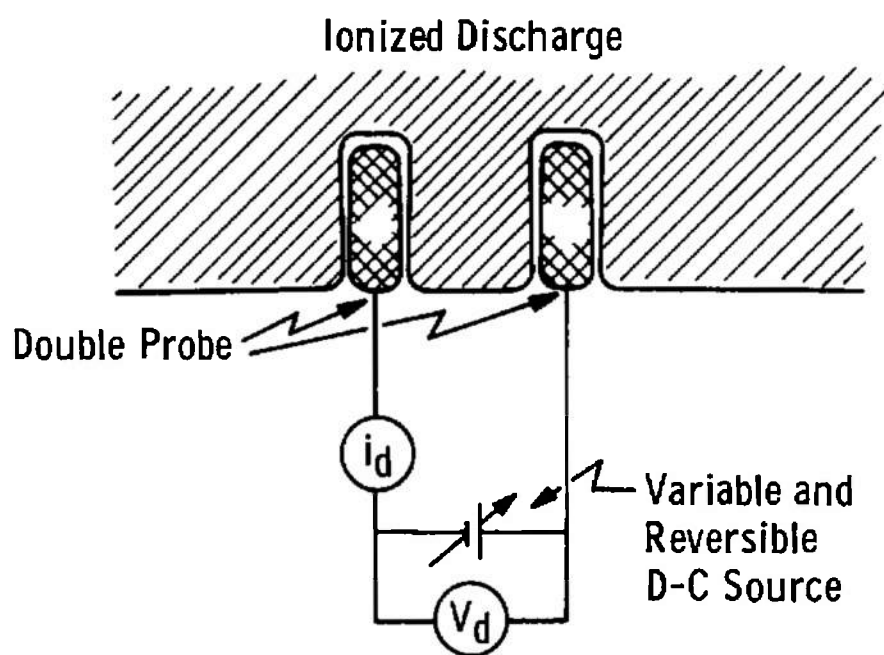


Fig. 11 Basic Double Probe Circuit

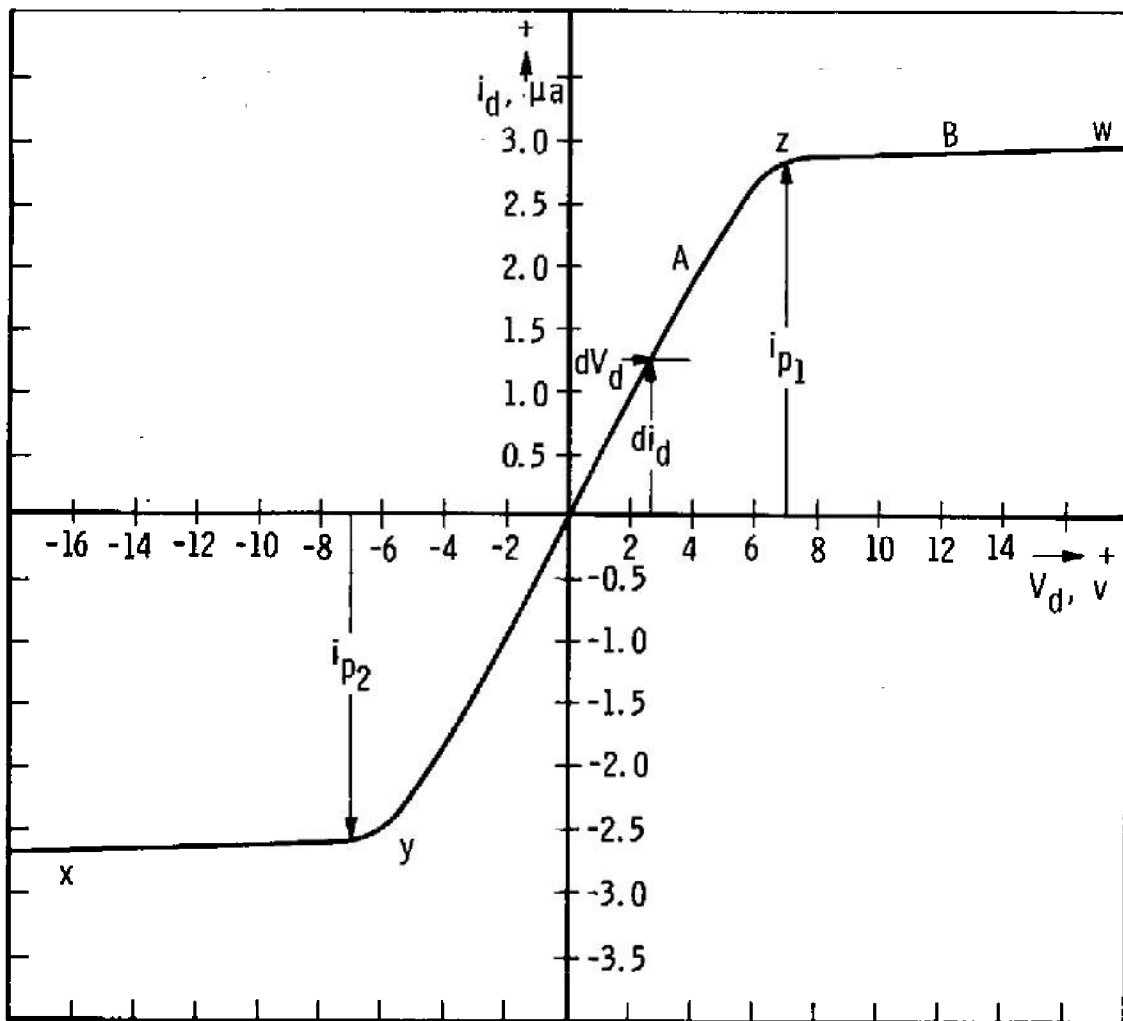


Fig. 12 Double Probe Characteristics of the Exhaust of a 5-cm
Electron Bombardment Ion Engine

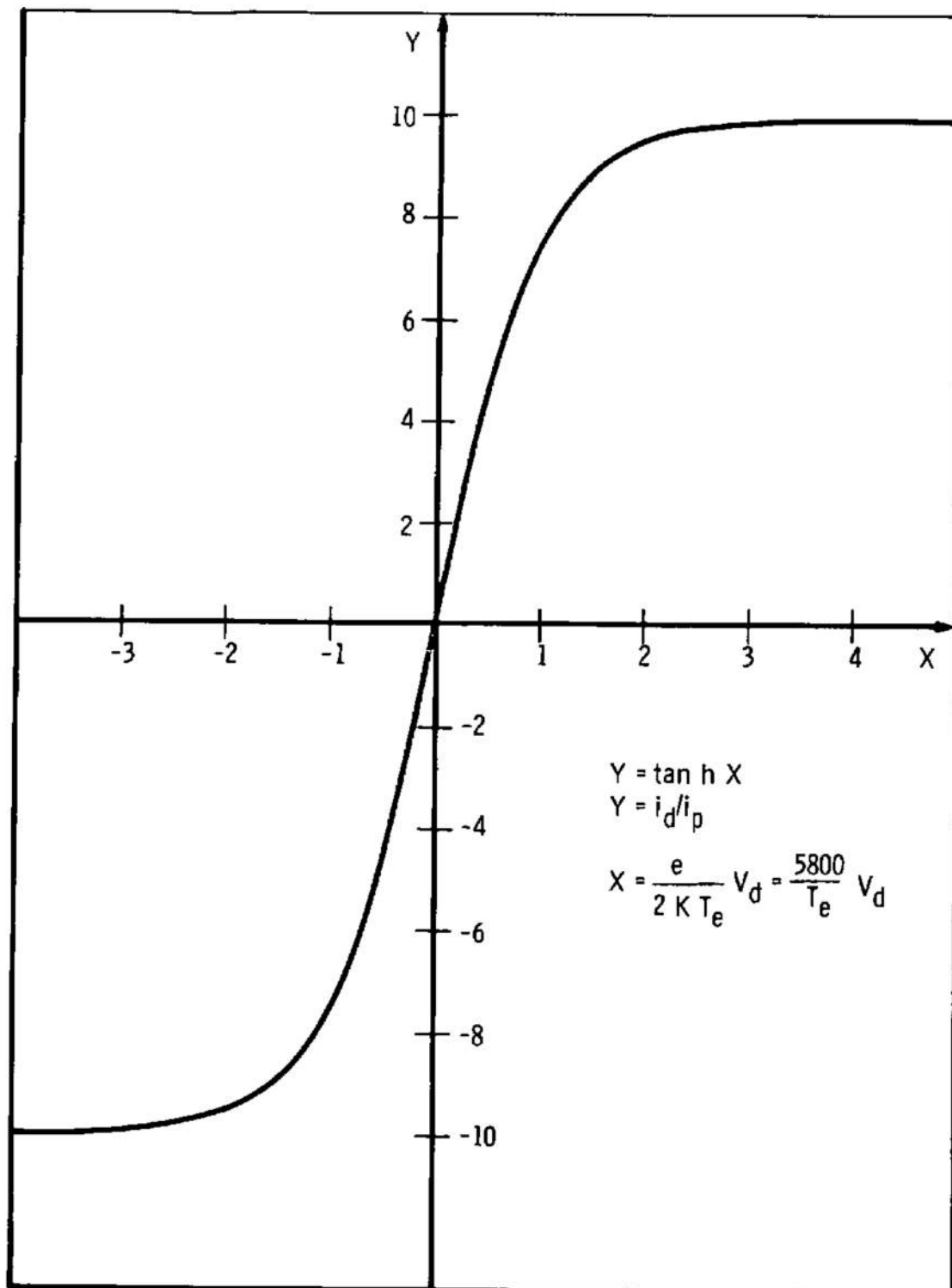


Fig. 13 Ideal Double Probe Volt-Ampere Characteristic

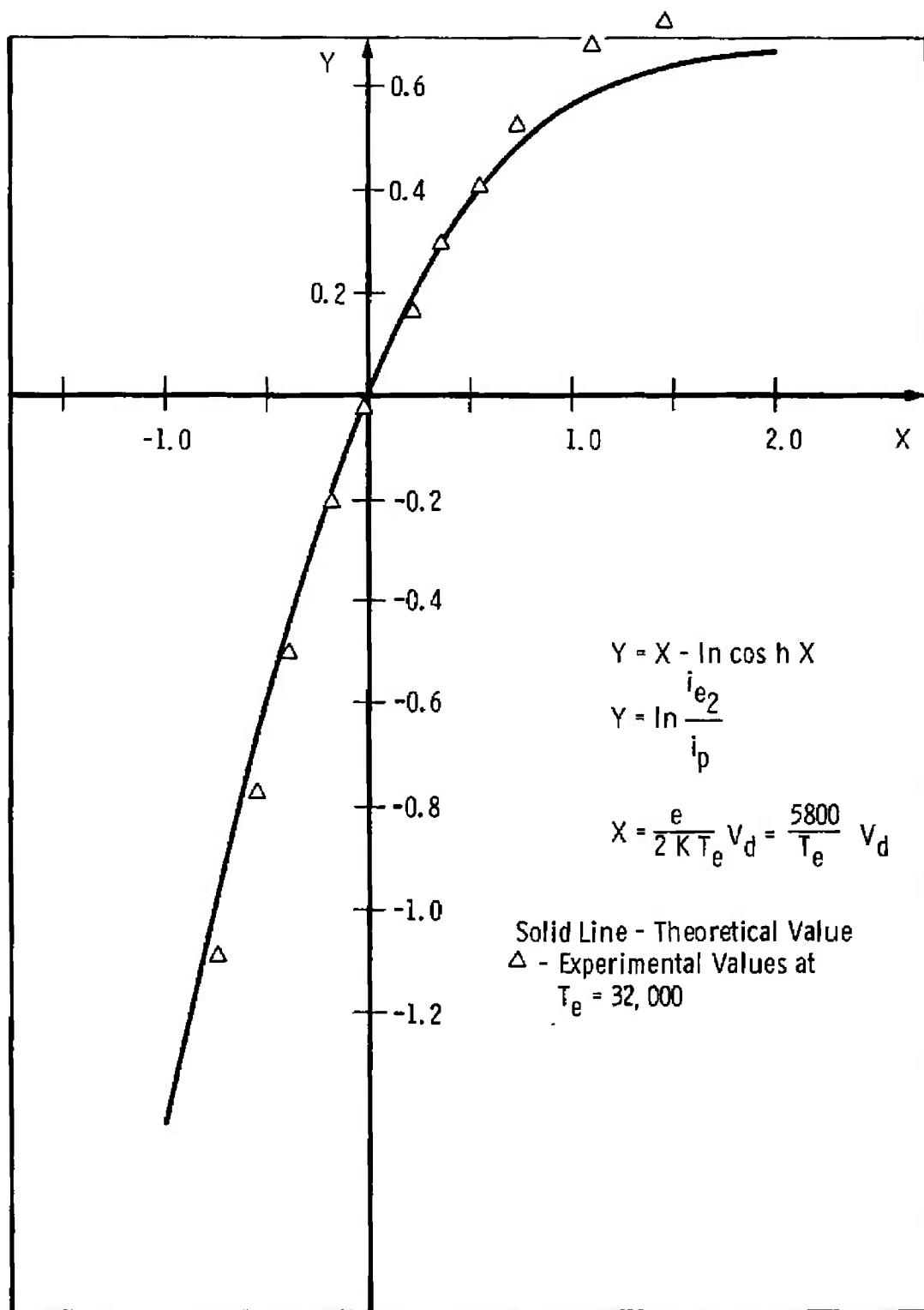


Fig. 14 Theoretical and Experimental Electron Current Plots for the Double Probe Method

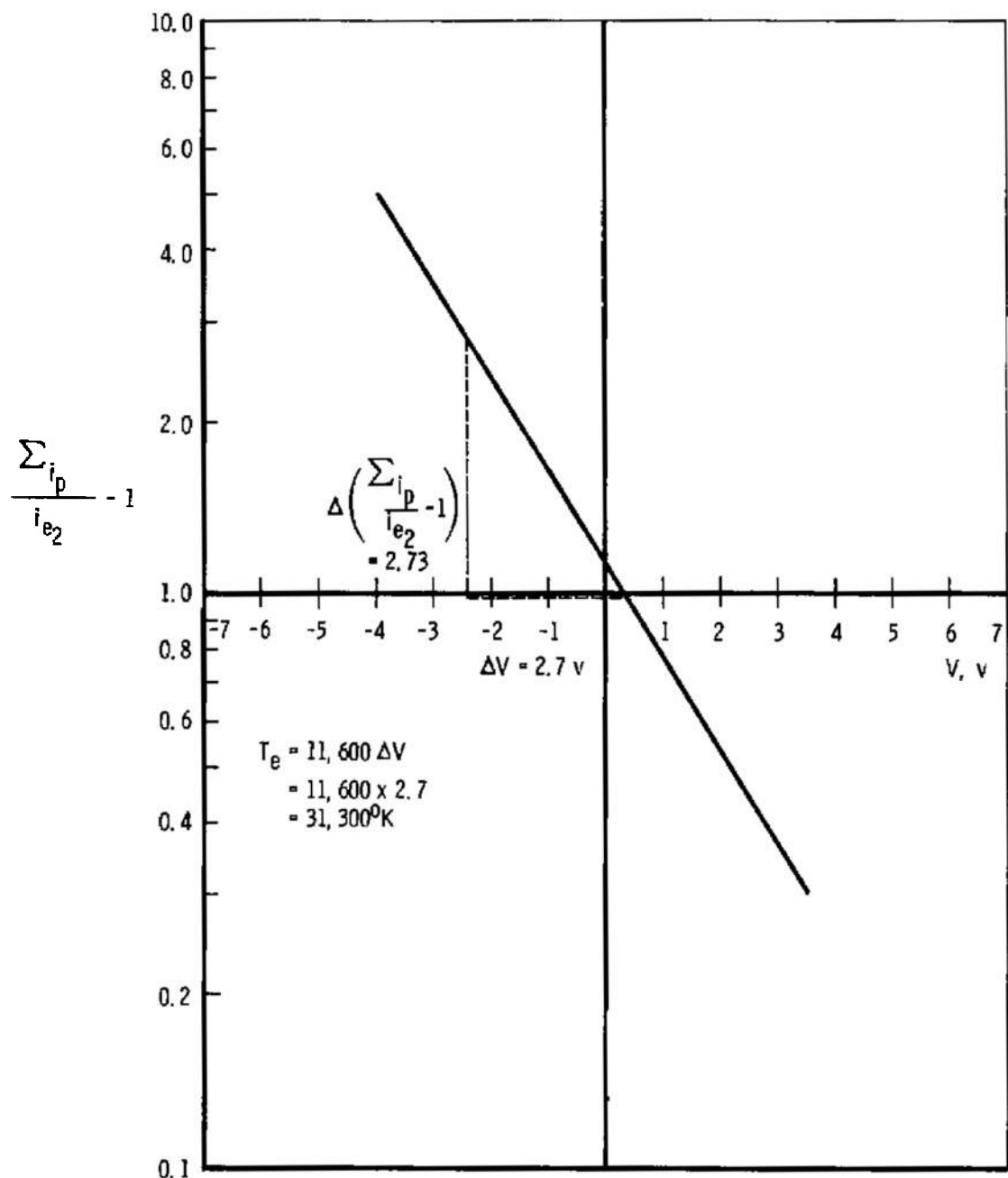


Fig. 15 Double Probe Temperature Determination Plot

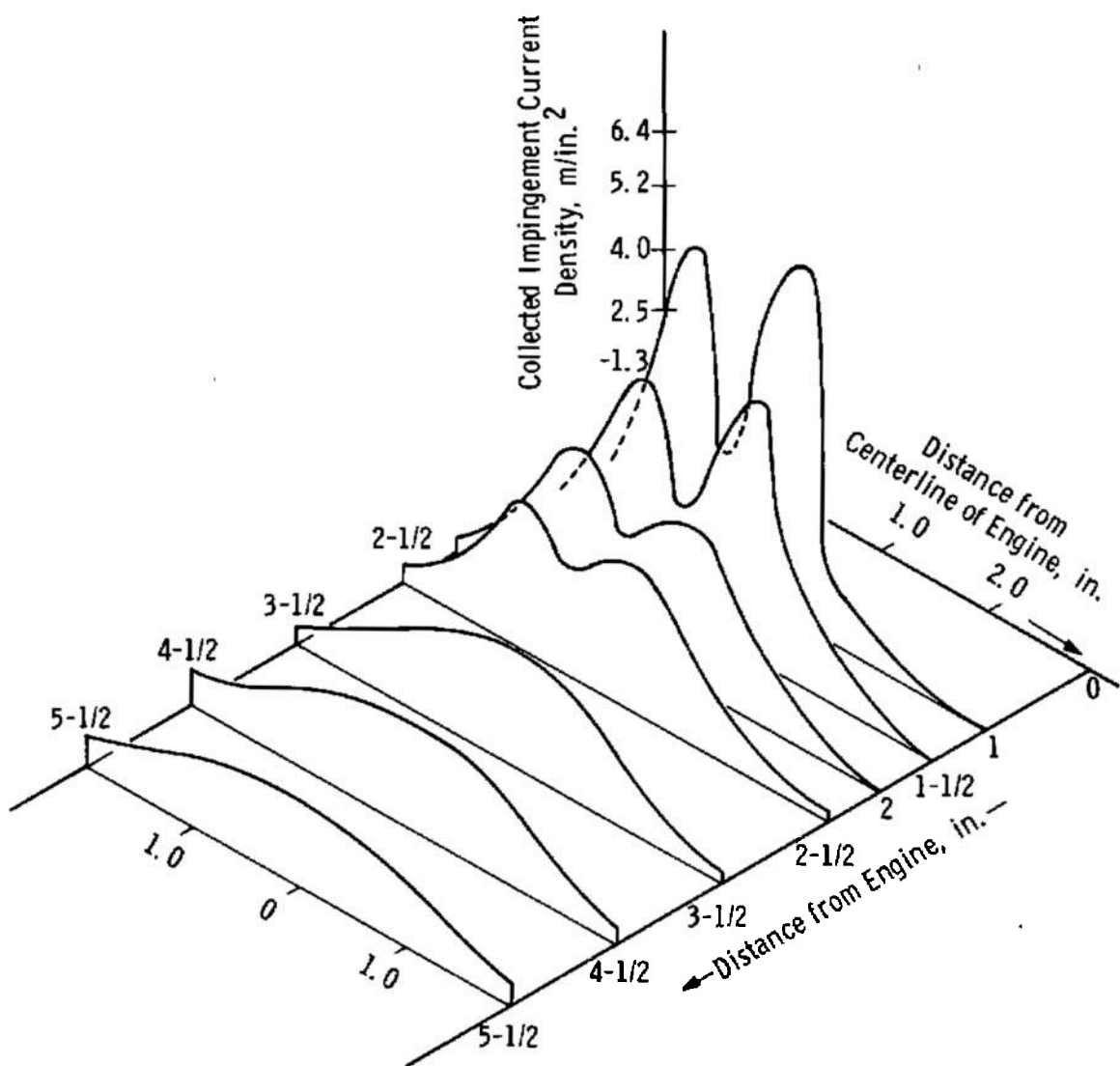


Fig. 16 Beam Profile of 5-cm Ion Source as Obtained from the Double Probe

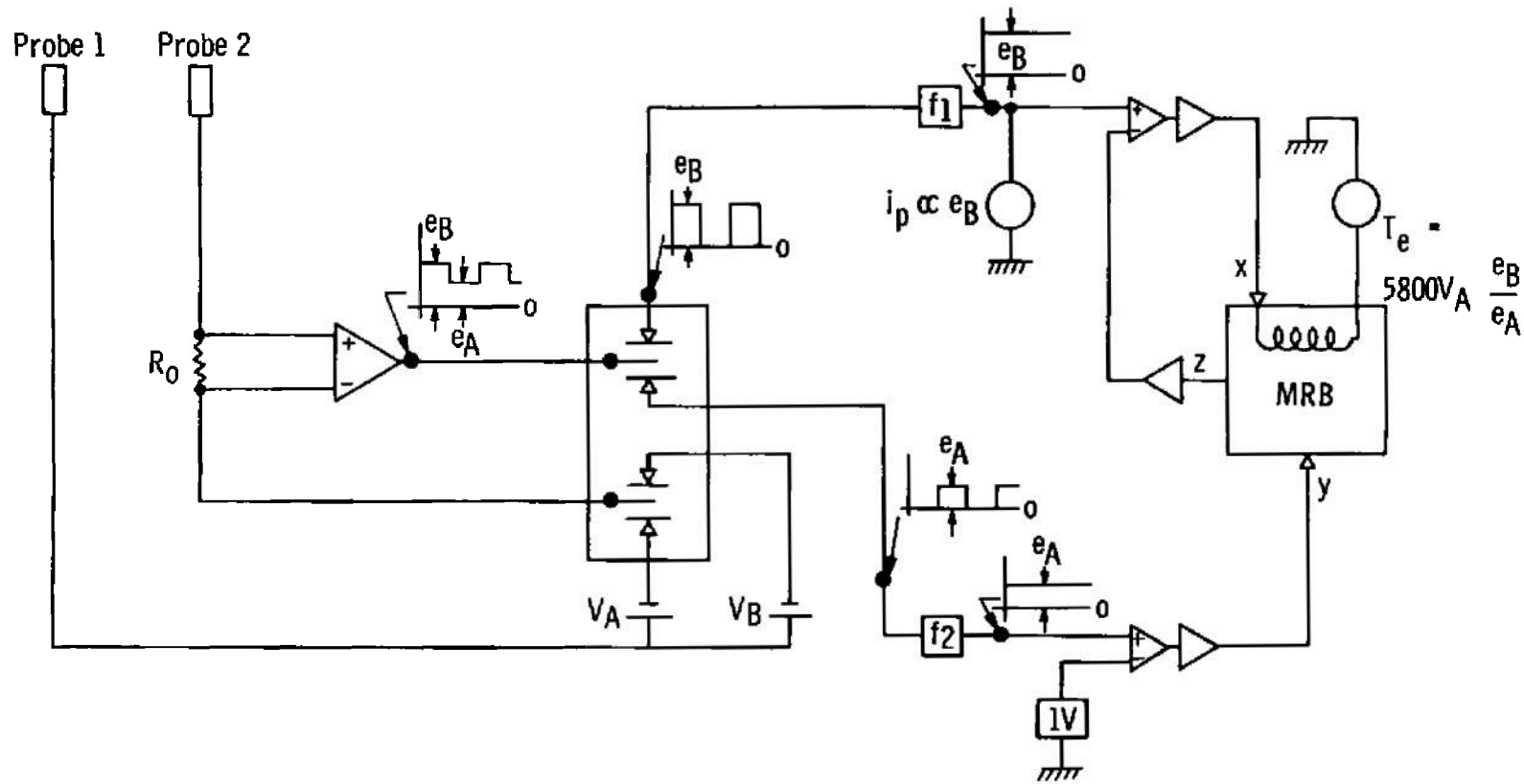


Fig. 17 Block Diagram and Voltage Waveforms of Circuitry for Monitoring T_e with the Double Probe

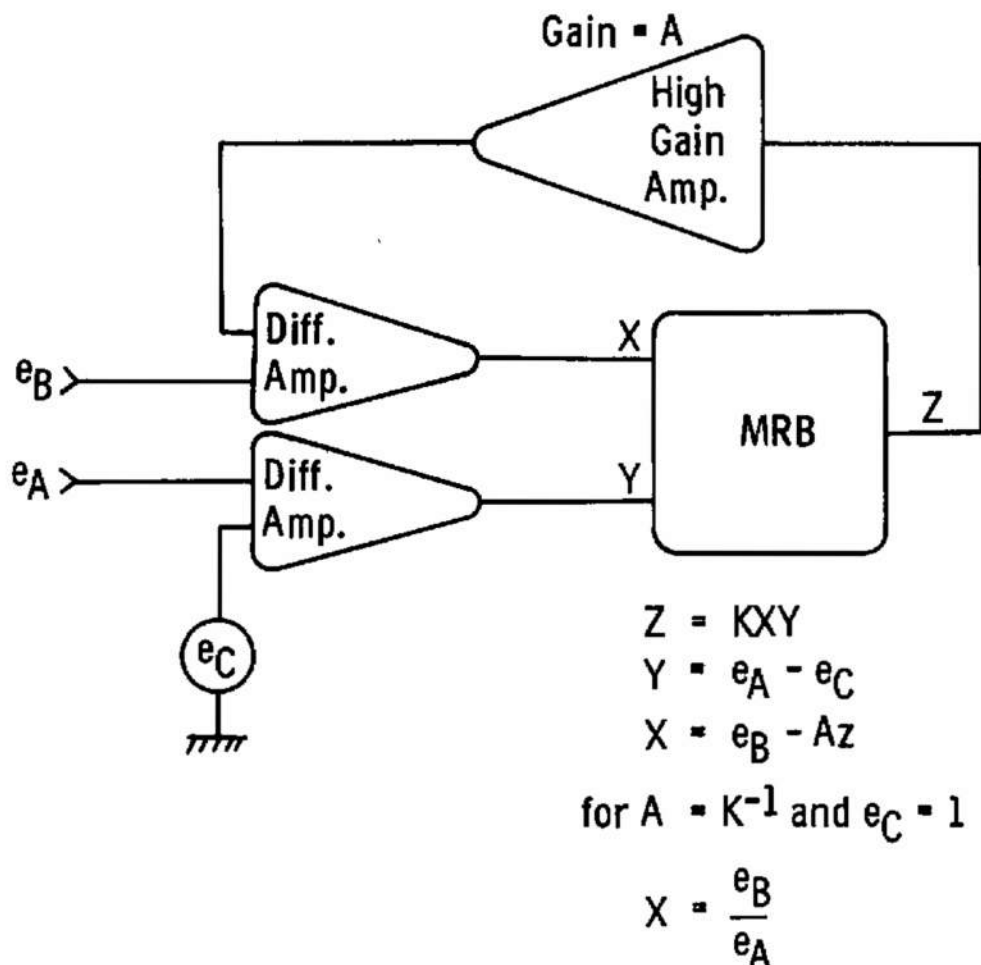


Fig. 18 Basic Magnetoresistance Bridge Analog Division Circuit

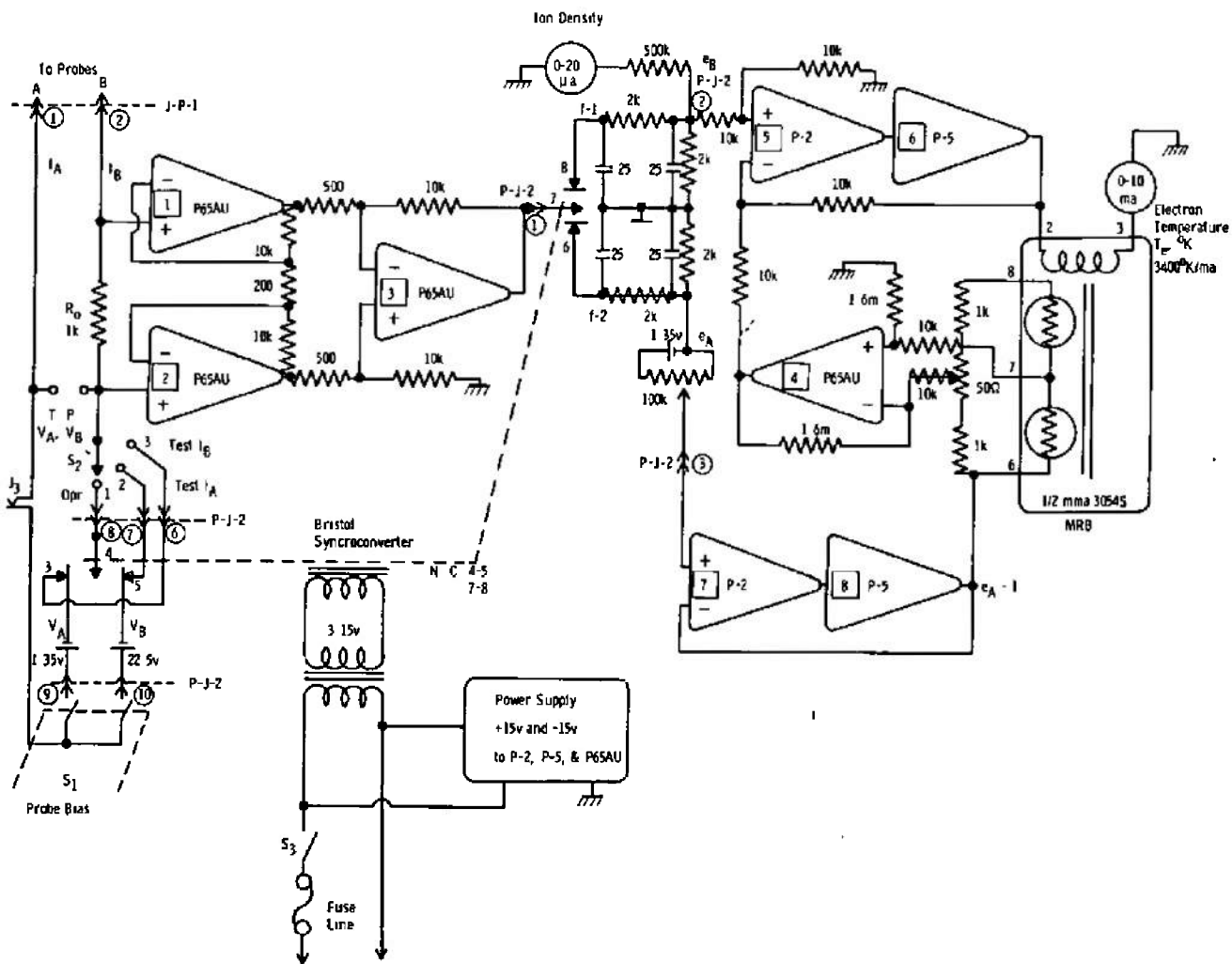


Fig. 19 Circuitry for Readout of Electron Temperature and Ion Density from a Double Langmuir Probe

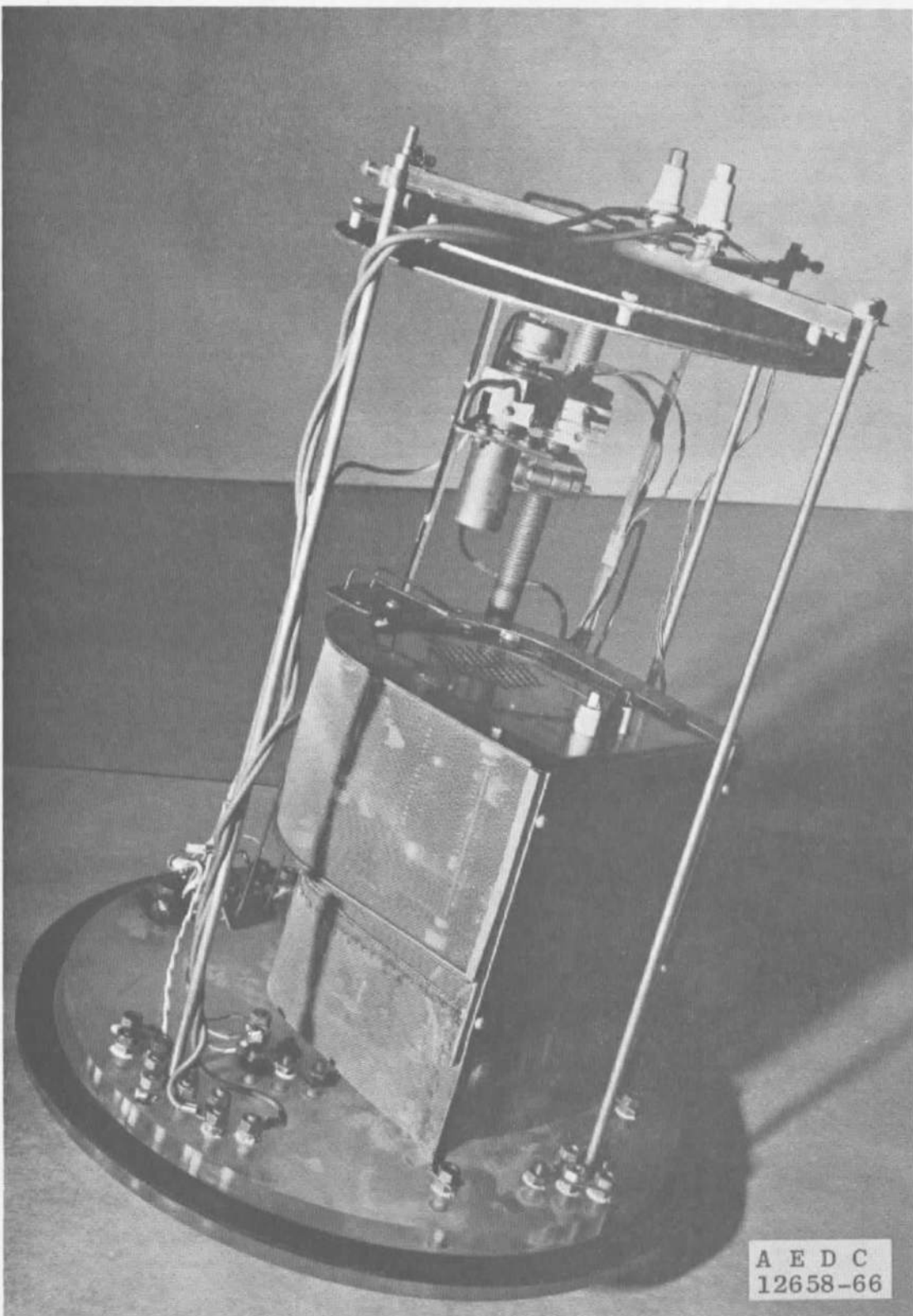


Fig. 20 5-cm Electron Bombardment Ion Engine and Probe Mounting System

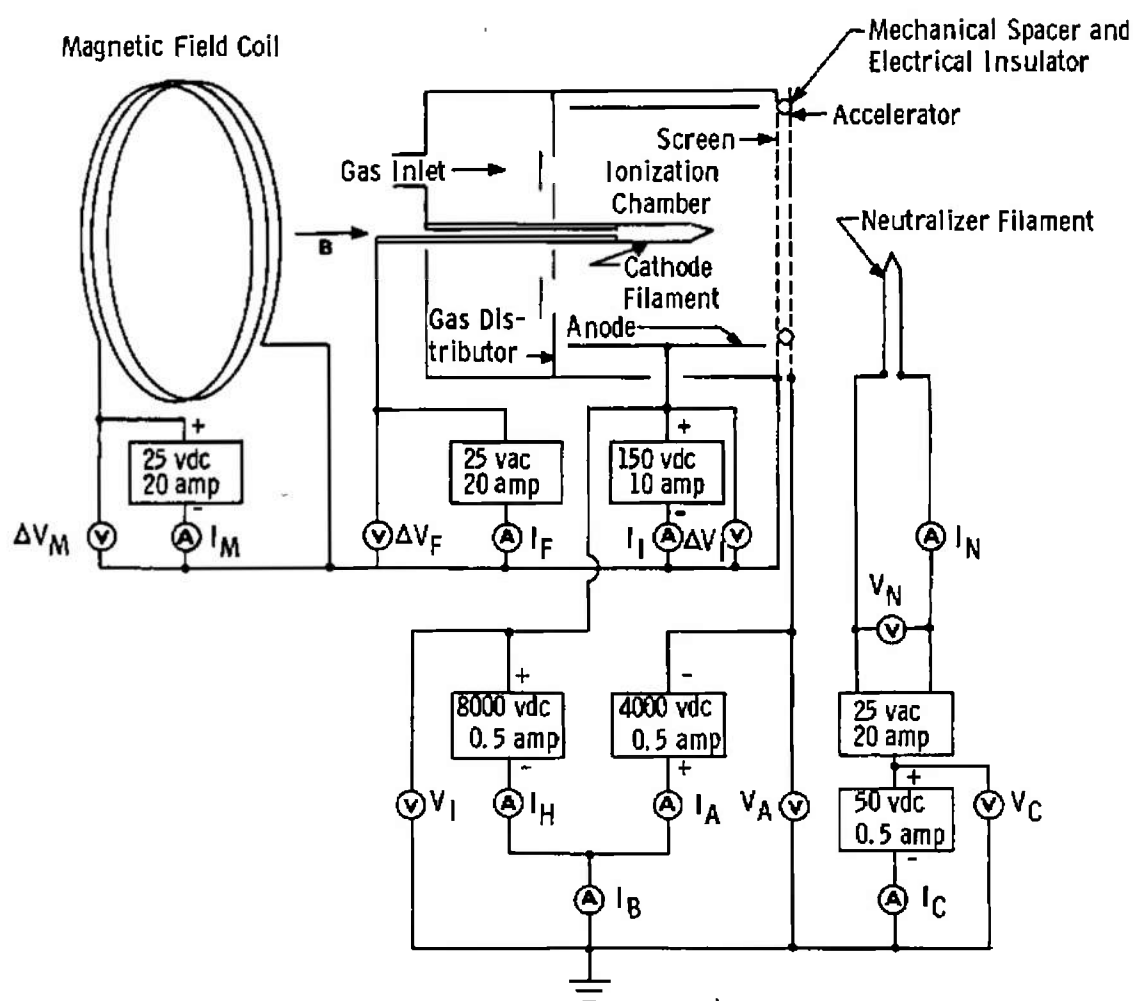


Fig. 21 Schematic of Ion Engine and Power Supplies

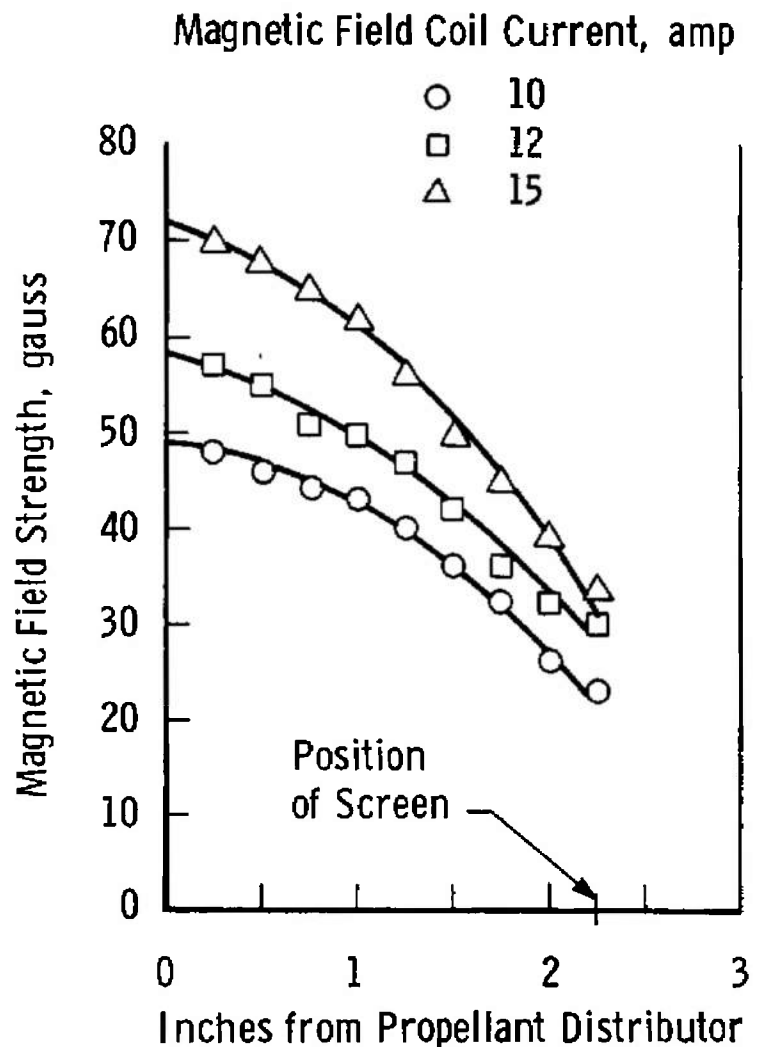


Fig. 22 Magnetic Field Strength versus Distance from Propellant Distributor

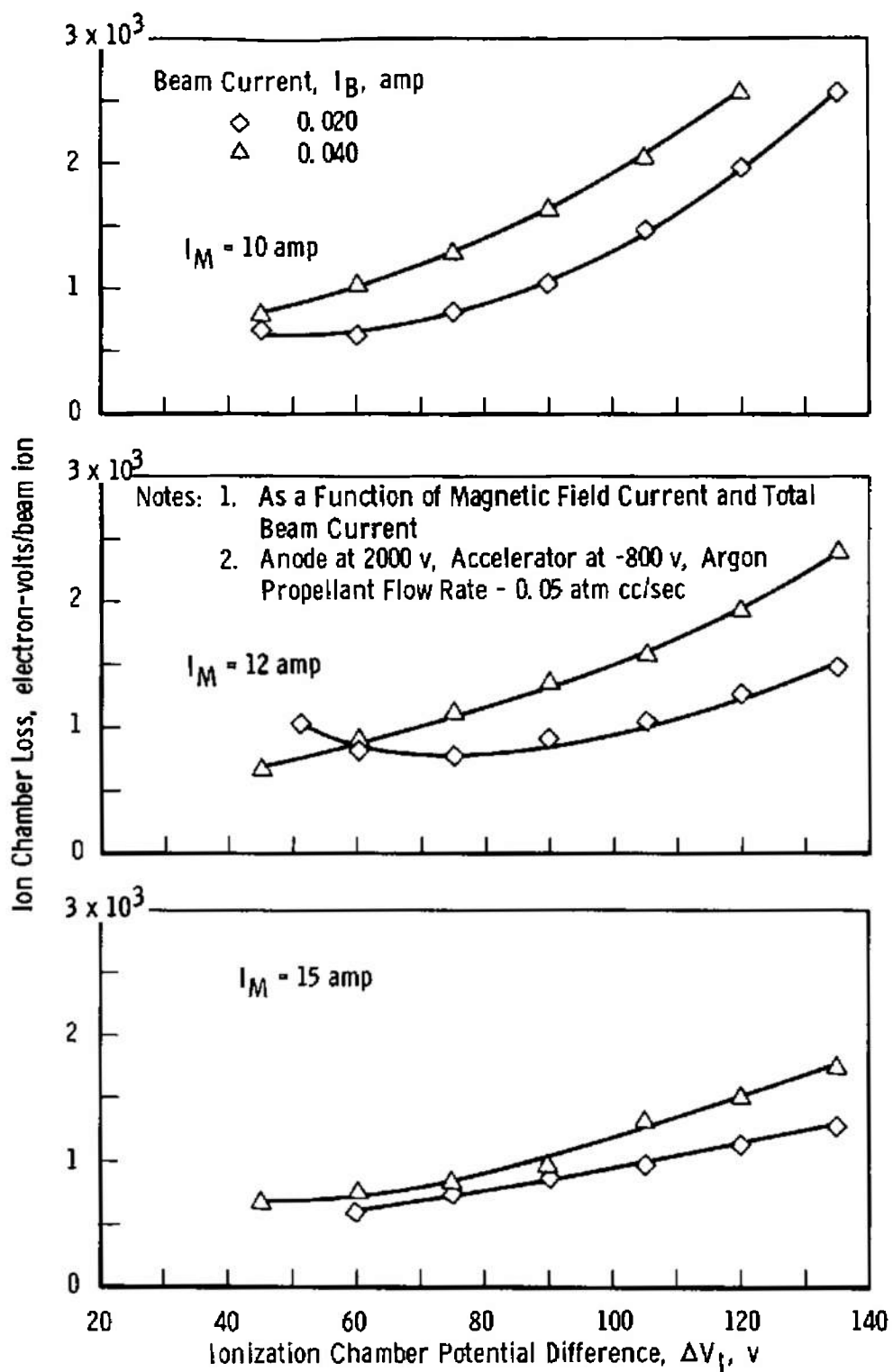


Fig. 23 Ionization Chamber Efficiency versus Chamber Potential Difference

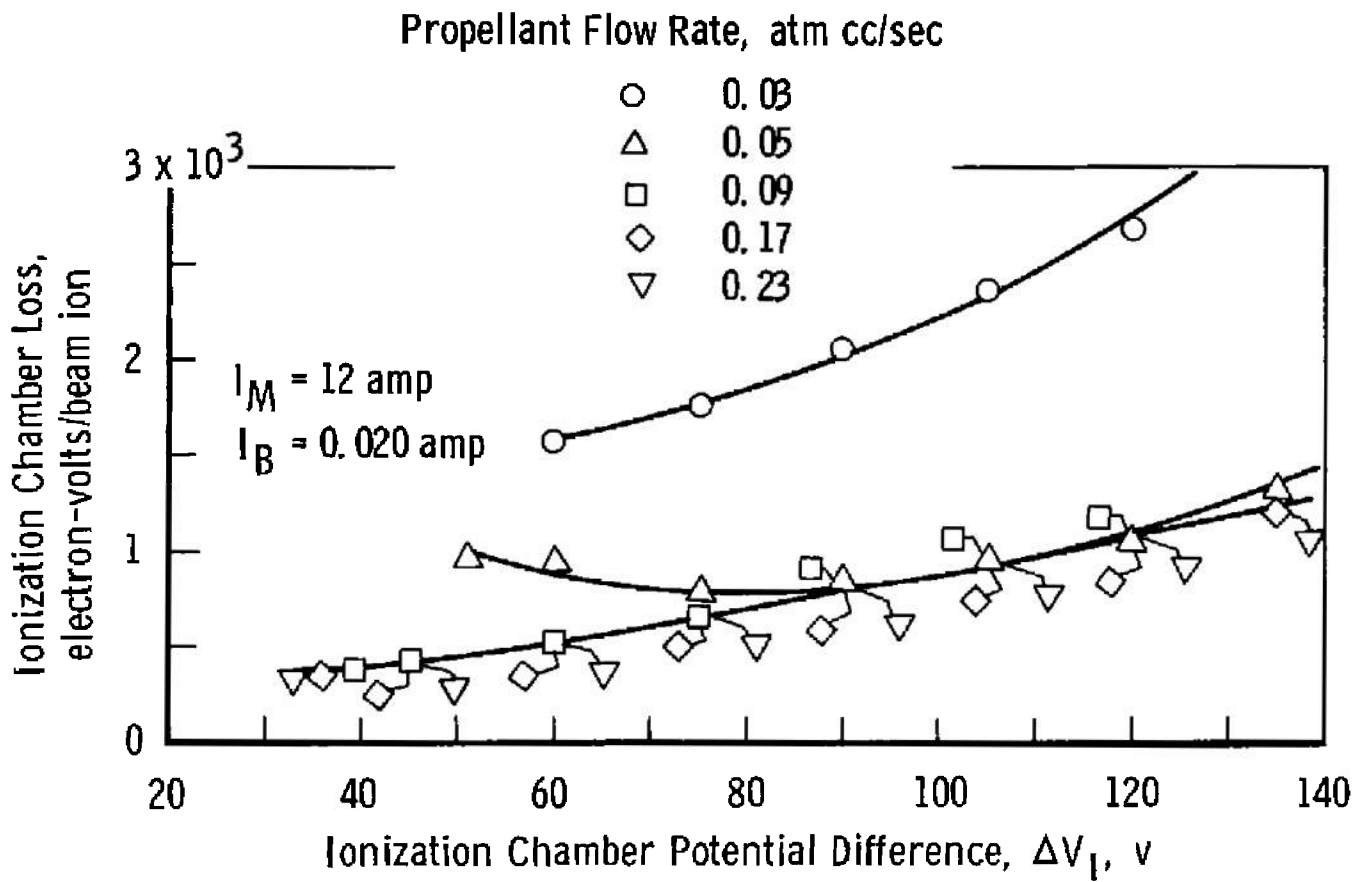


Fig. 24 Ionization Chamber Efficiency versus Chamber Potential Difference as a Function of Propellant Flow Rate

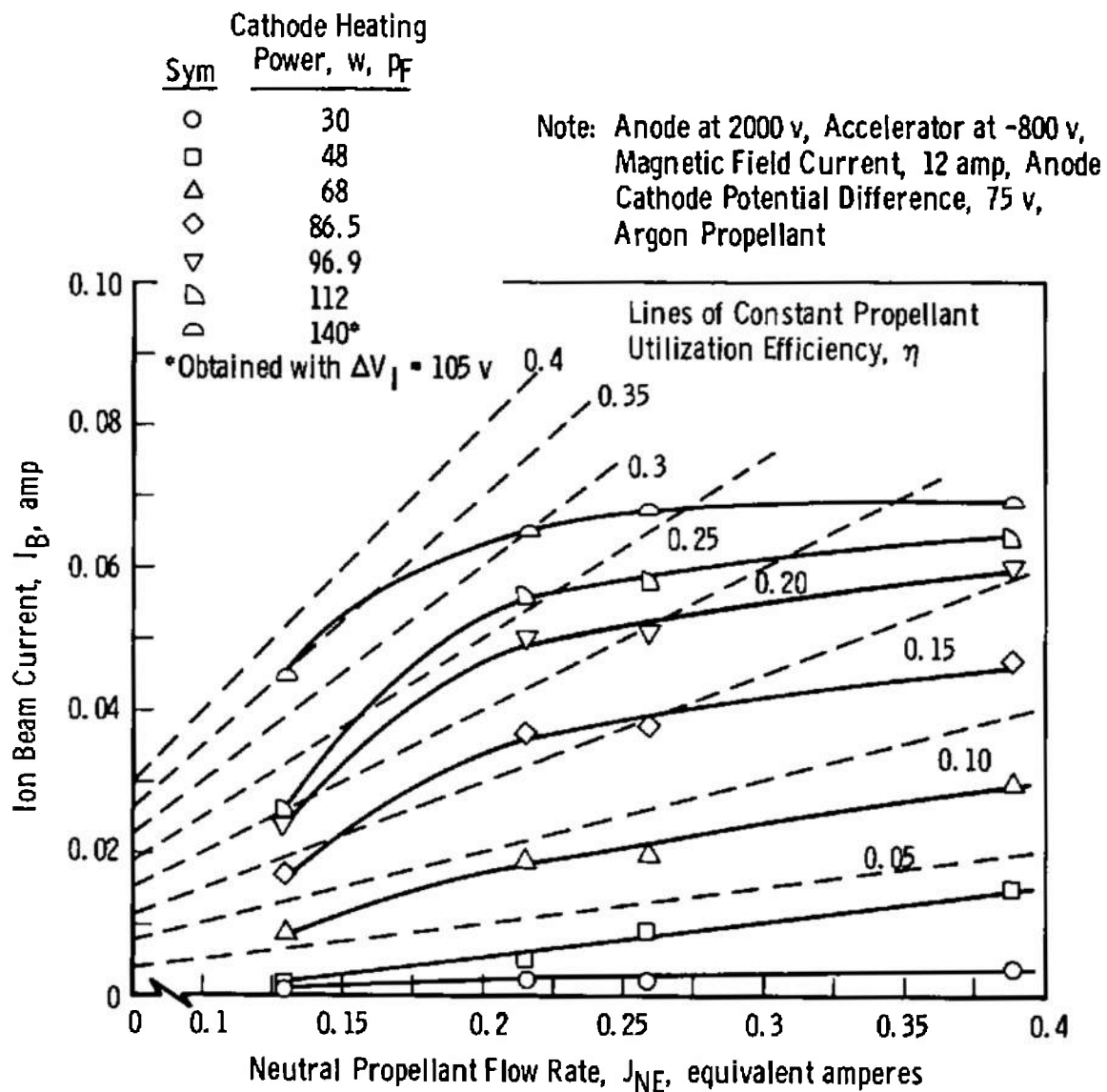


Fig. 25 Ion Beam Current versus Neutral Propellant Flow Rate

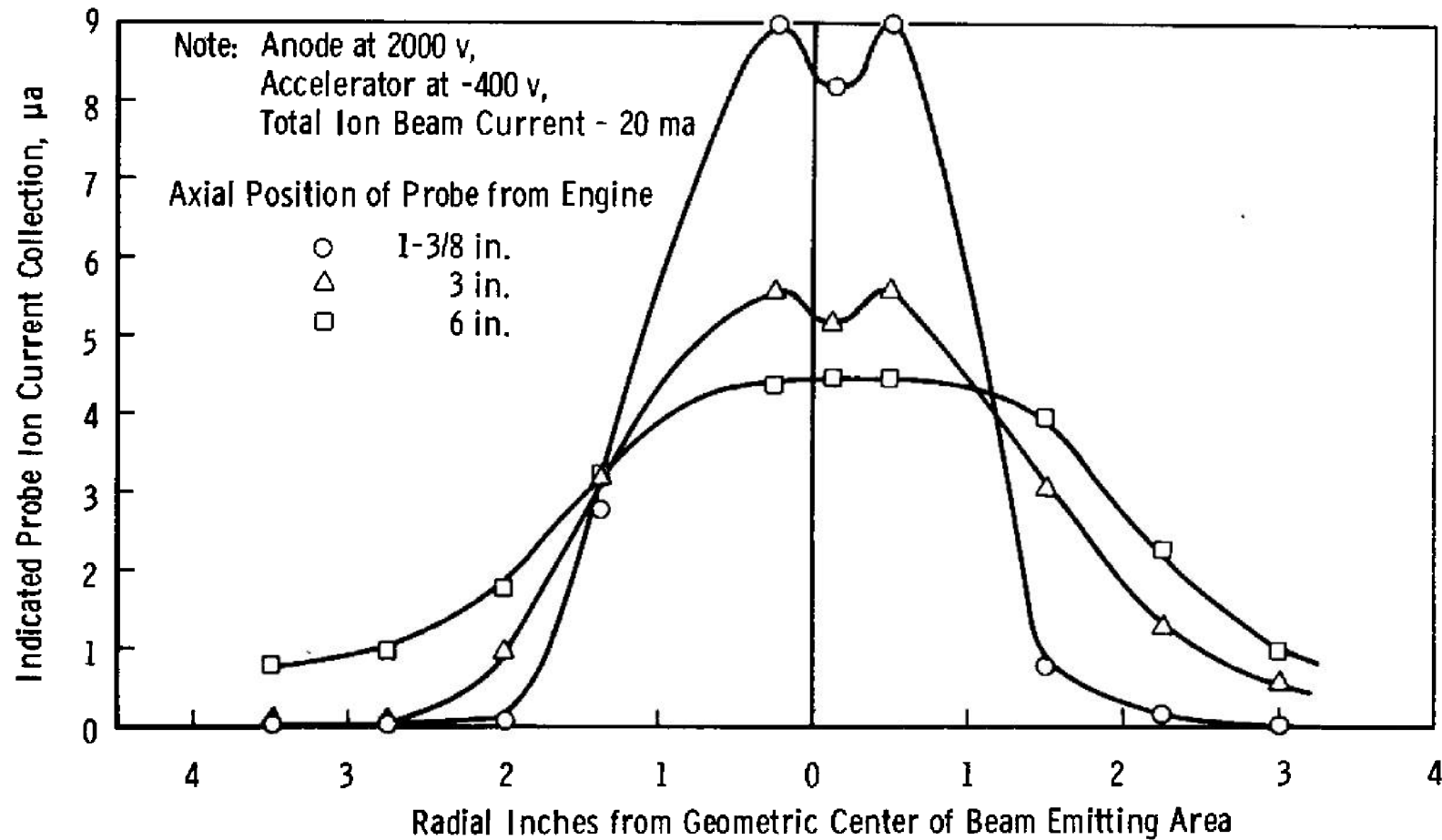


Fig. 26 Radial Ion Beam Density Profile (Impingement Probe)

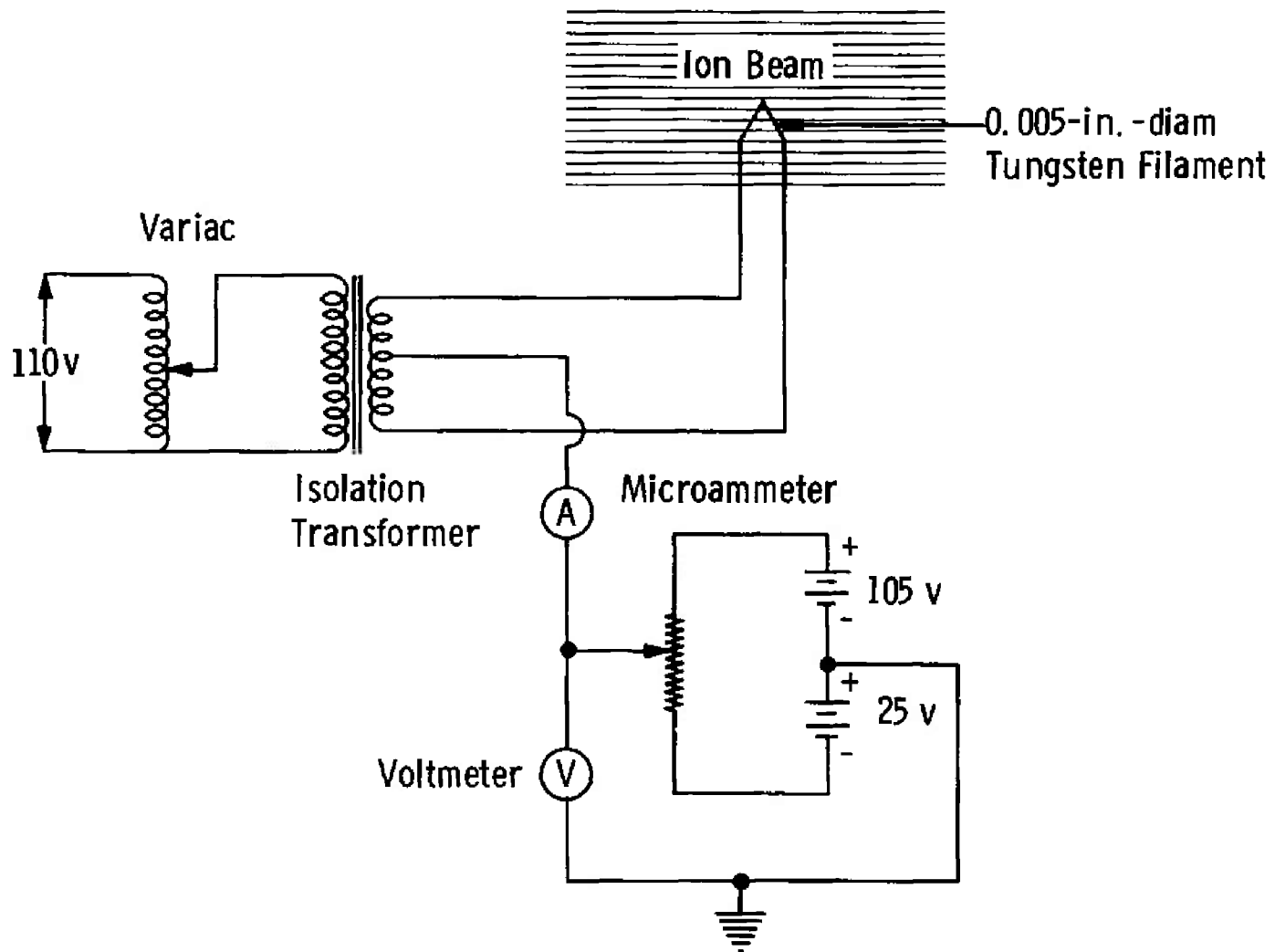


Fig. 27 Emissive Probe and Ion Beam Impingement Probe Circuitry

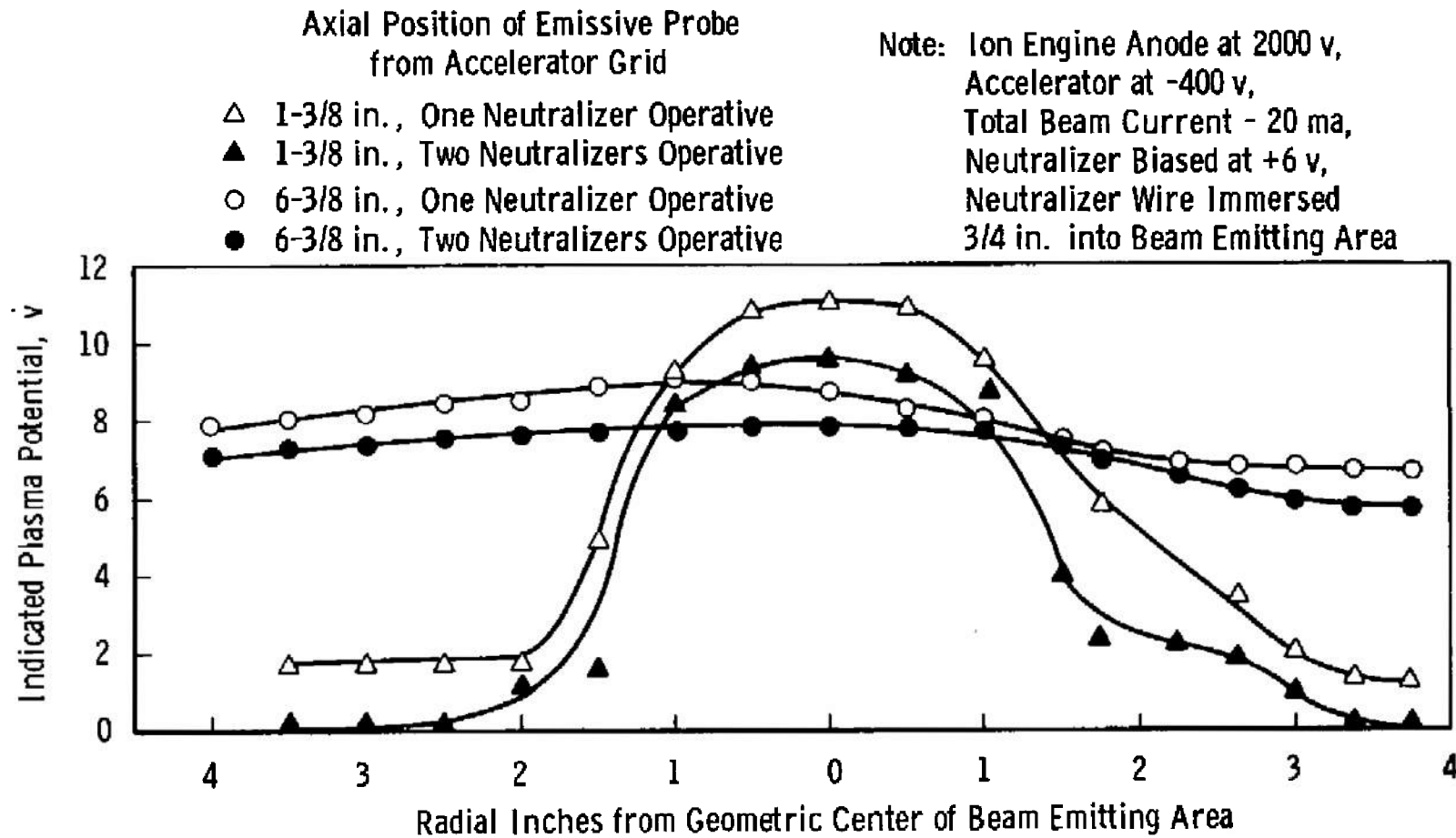


Fig. 28 Radial Plasma Potential Profile

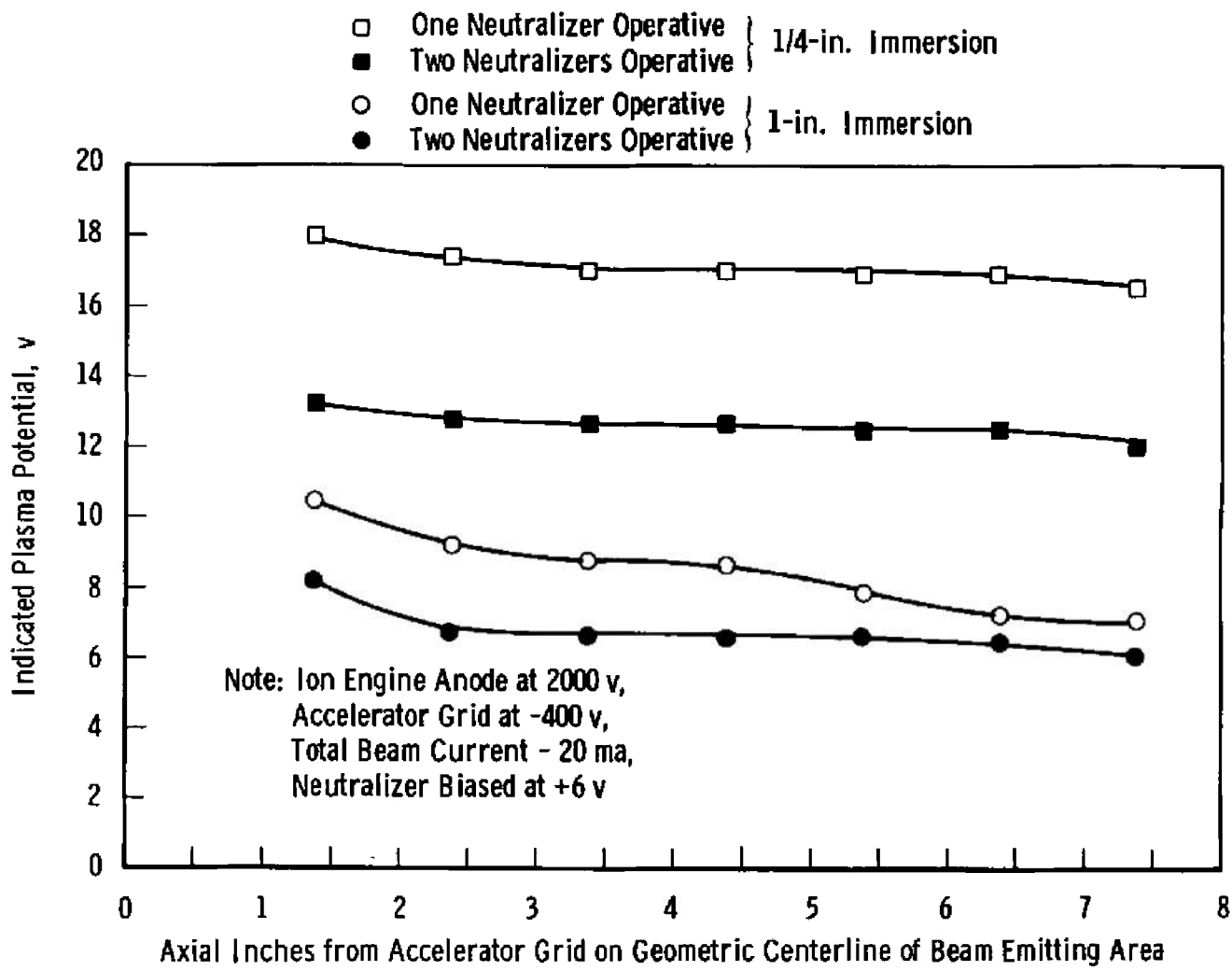


Fig. 29 Axial Plasma Potential Profile

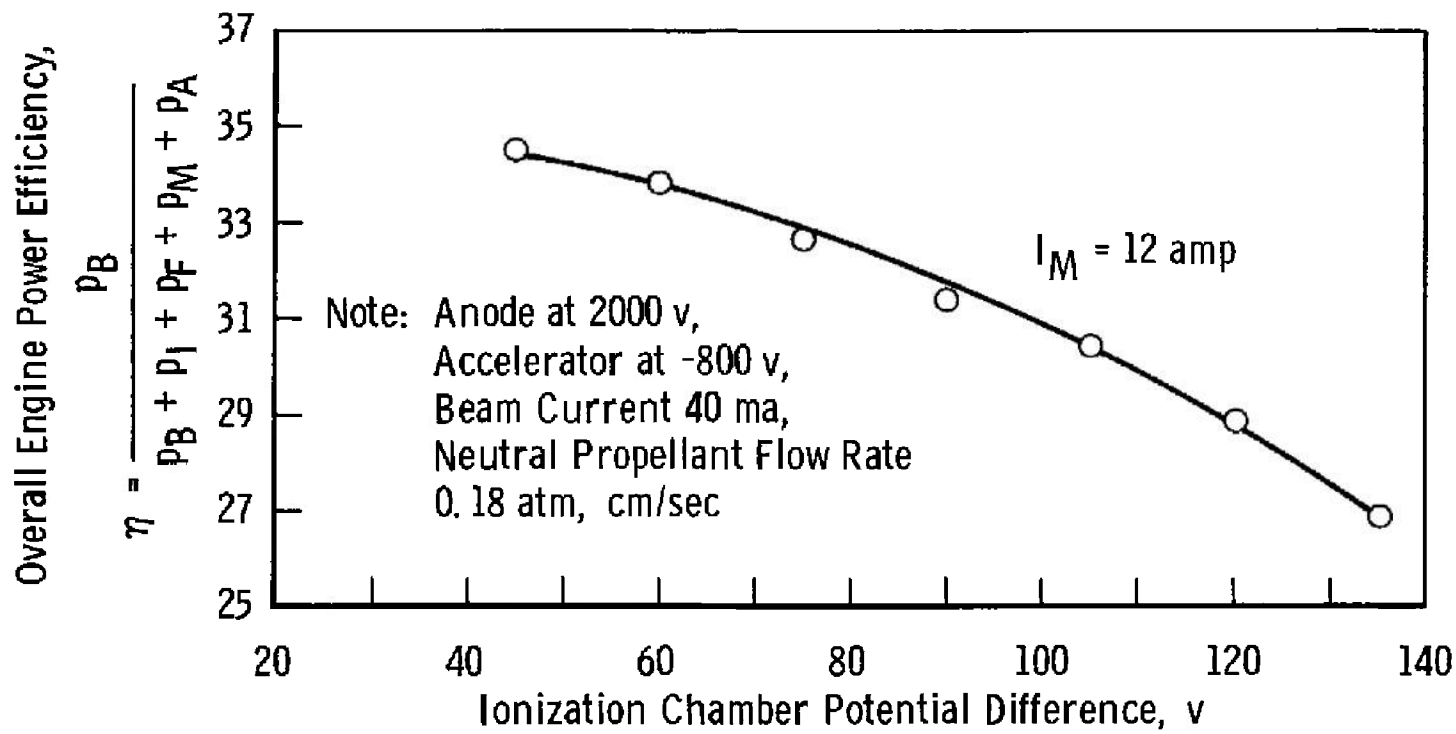


Fig. 30 Power Efficiency versus Ionization Chamber Potential

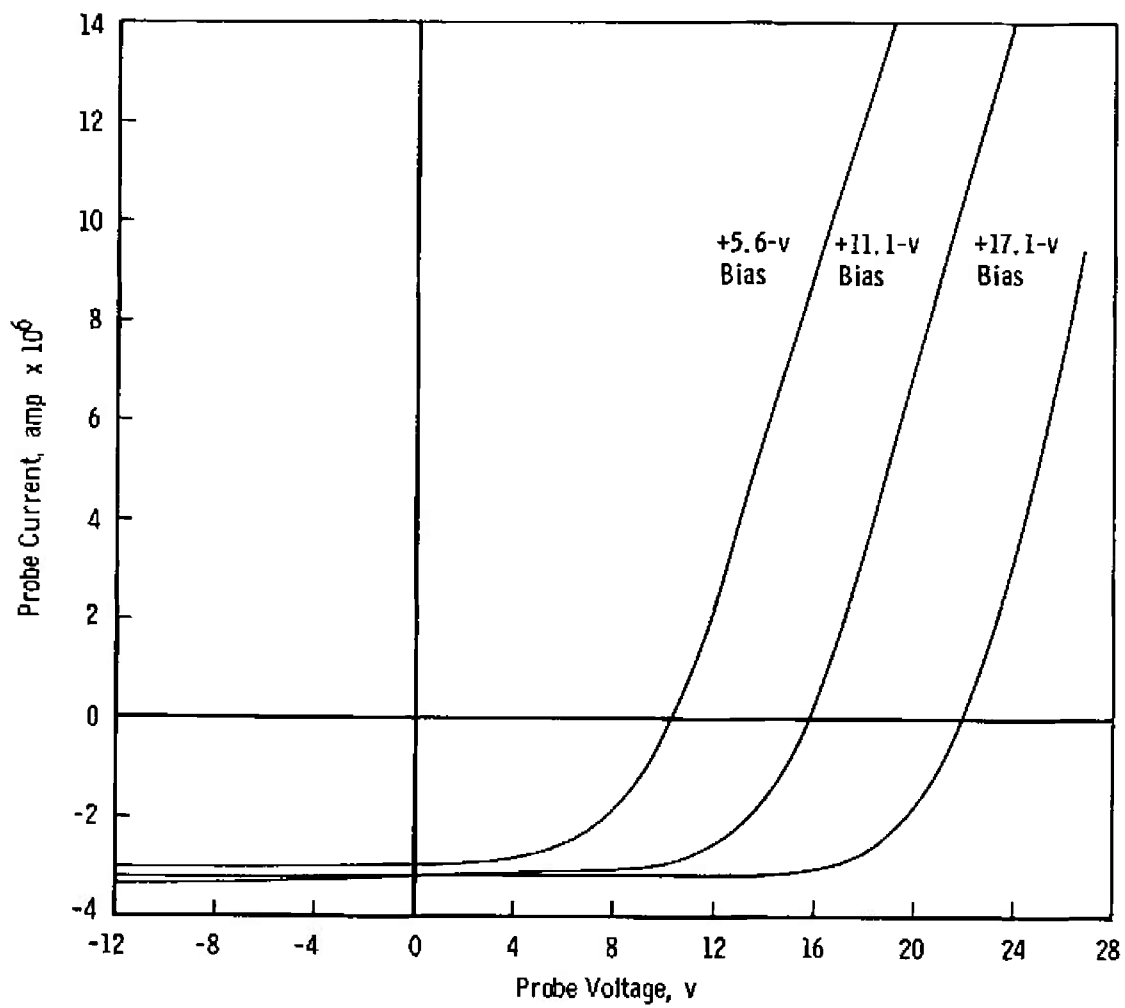


Fig. 31 Probe Voltage-Current Curves in the Ambient Plasma Stream

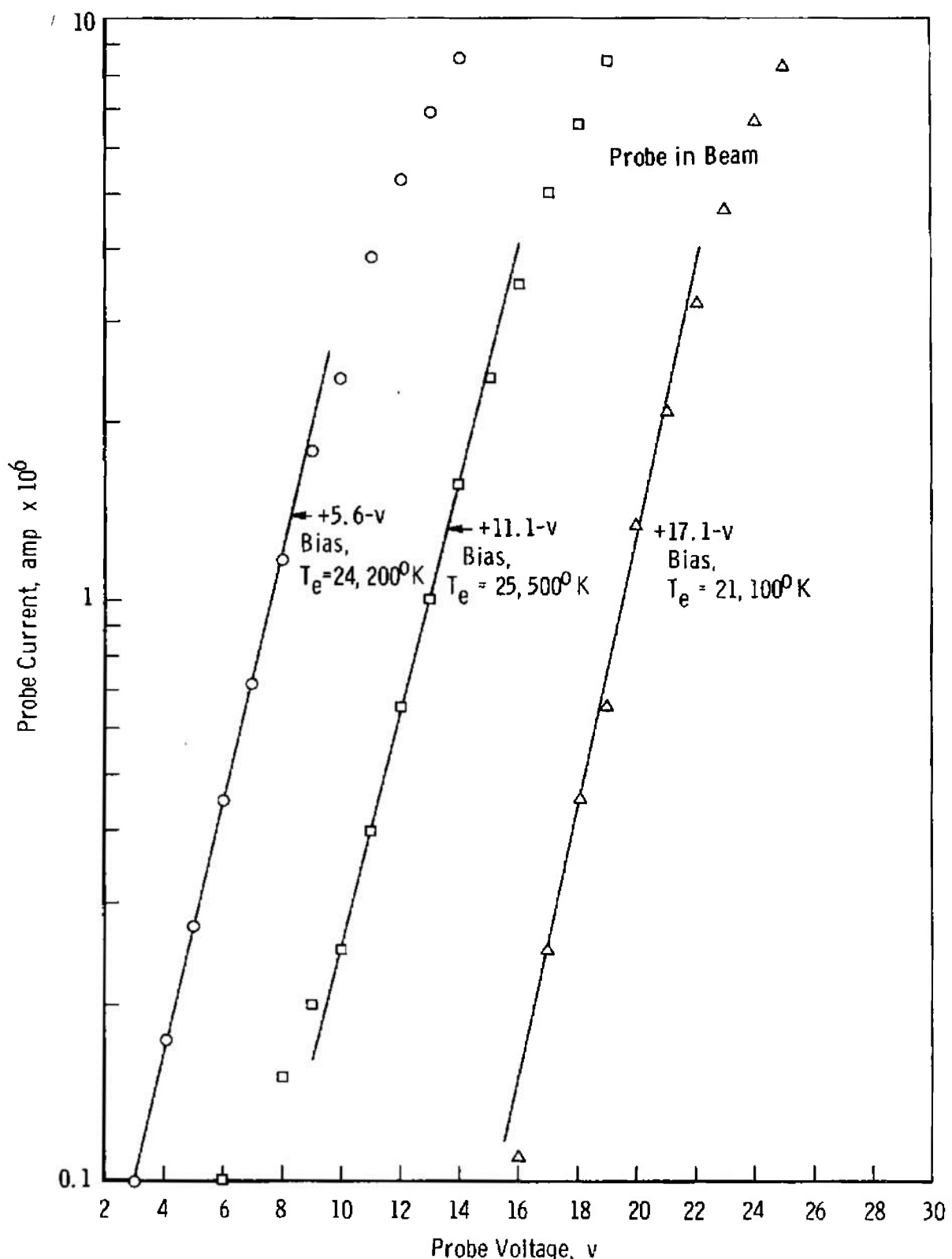


Fig. 32 Probe Voltage-Logarithm of Current Curves in the Ambient Plasma Stream

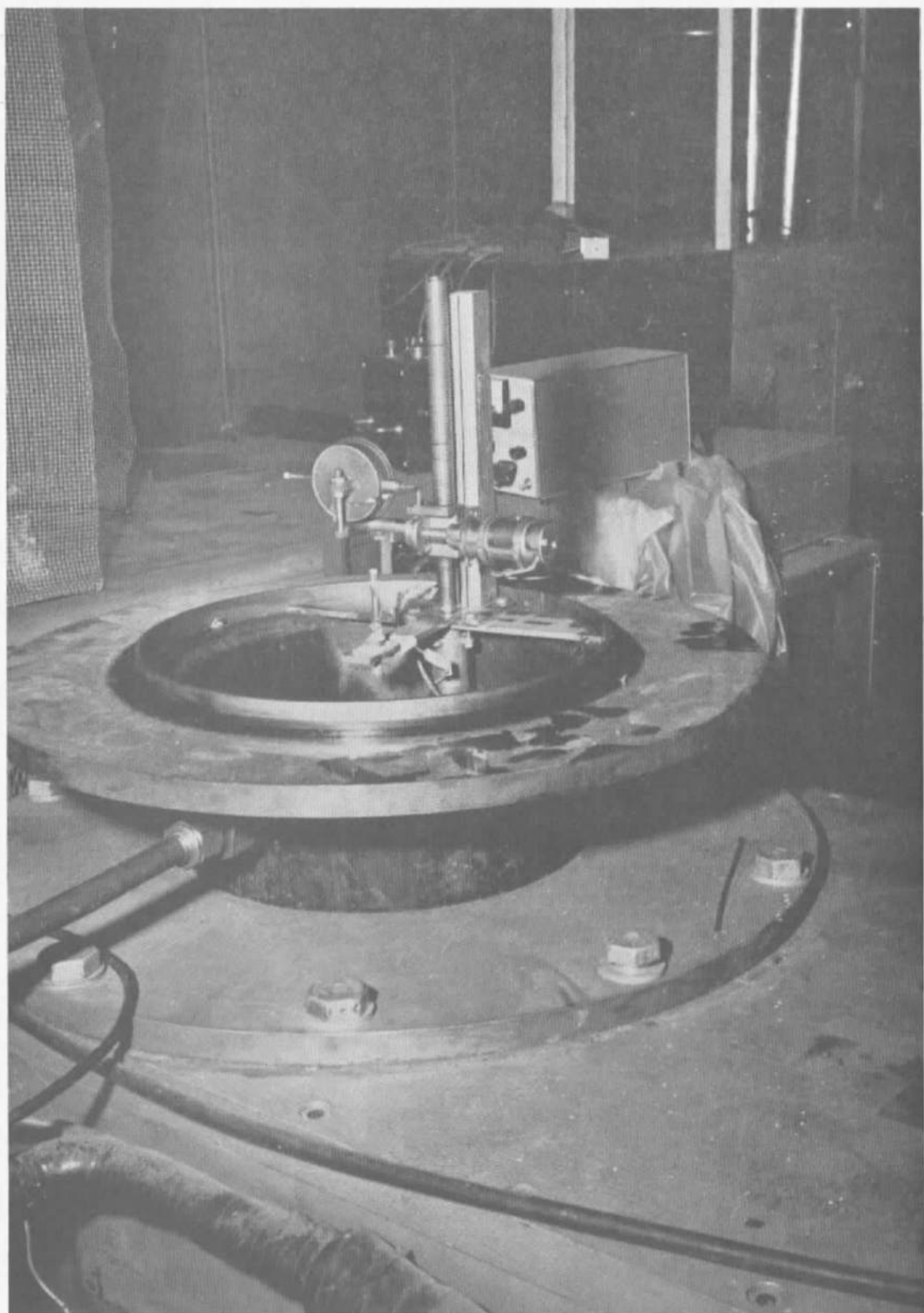


Fig. 33 Probe, Shield, and Traverse System

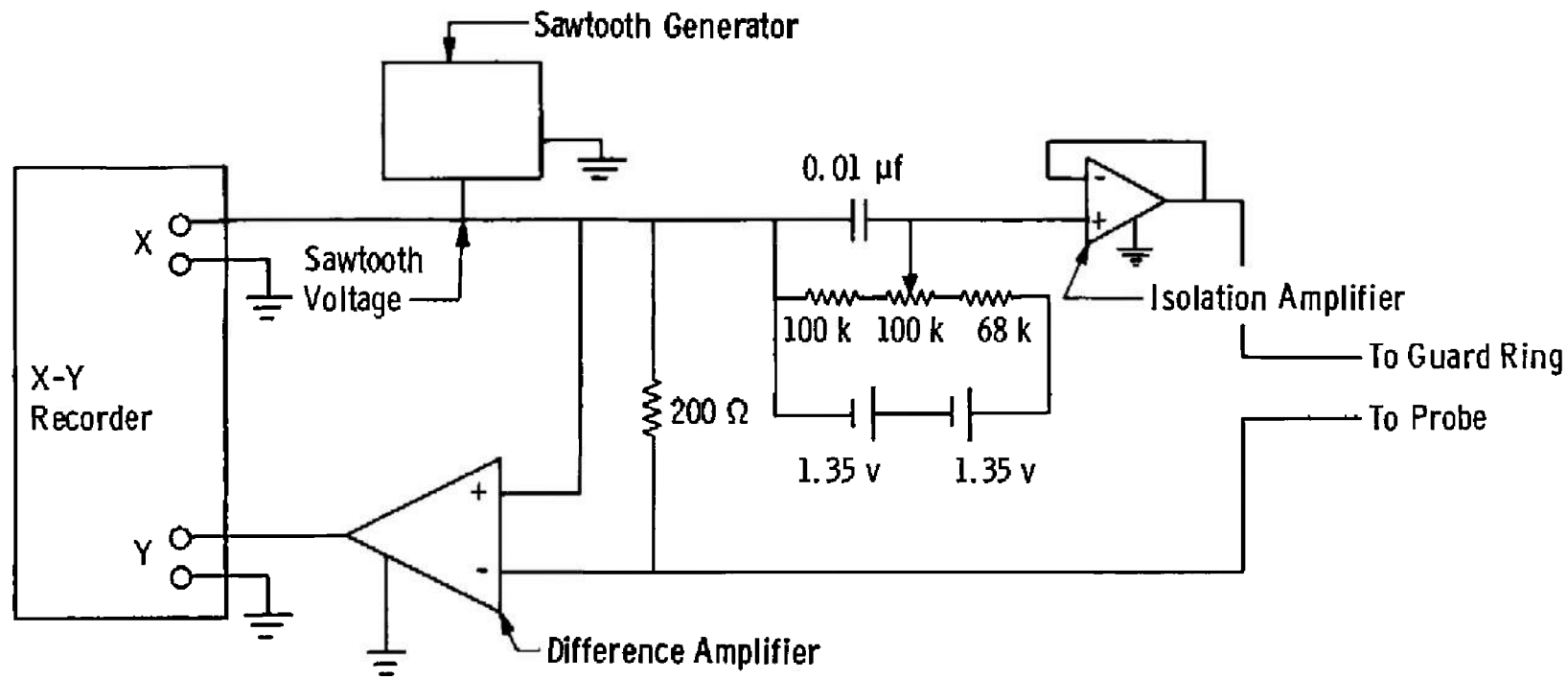


Fig. 34 Langmuir Characteristic Equipment Schematic

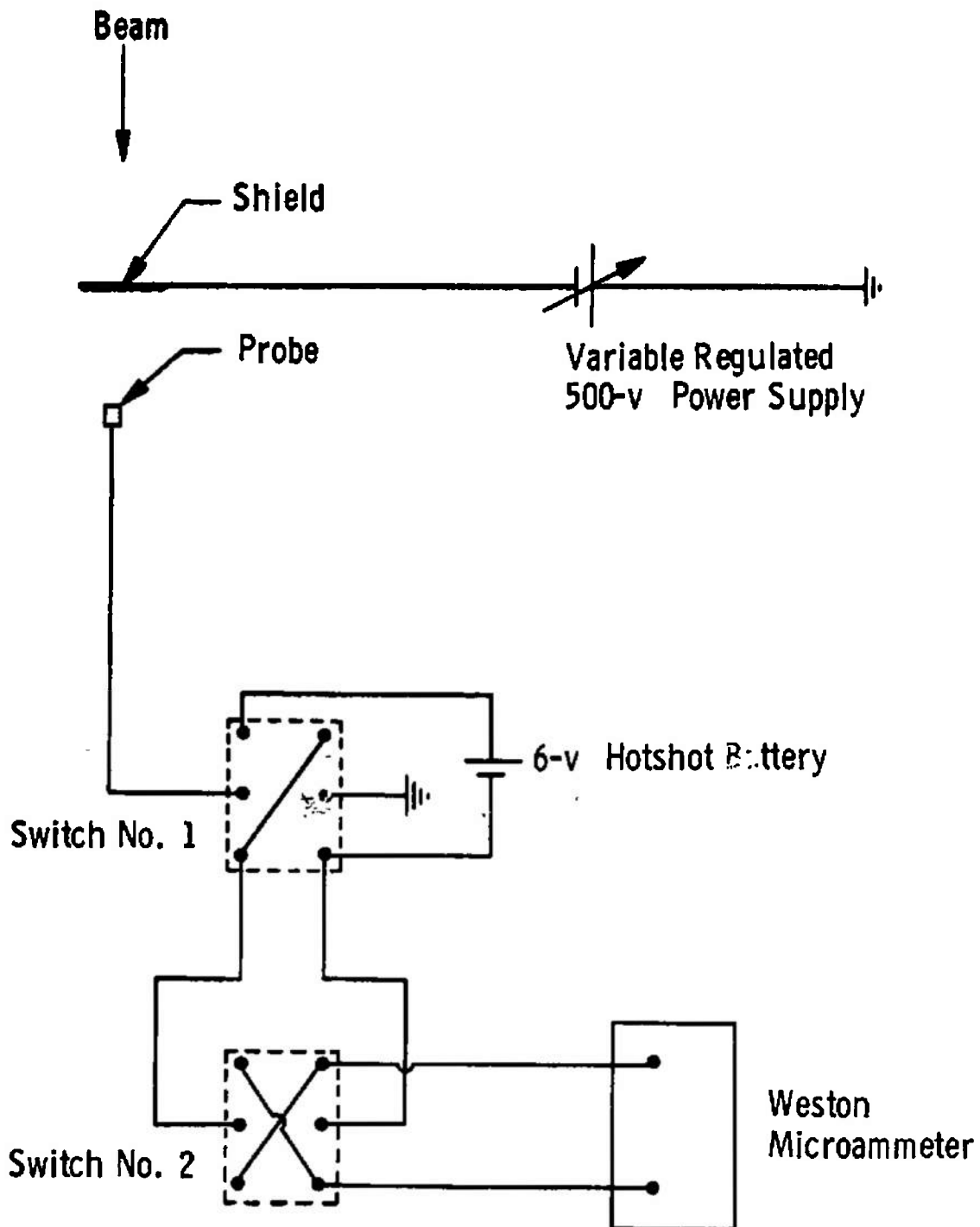


Fig. 35 Wake Investigation Equipment Schematic

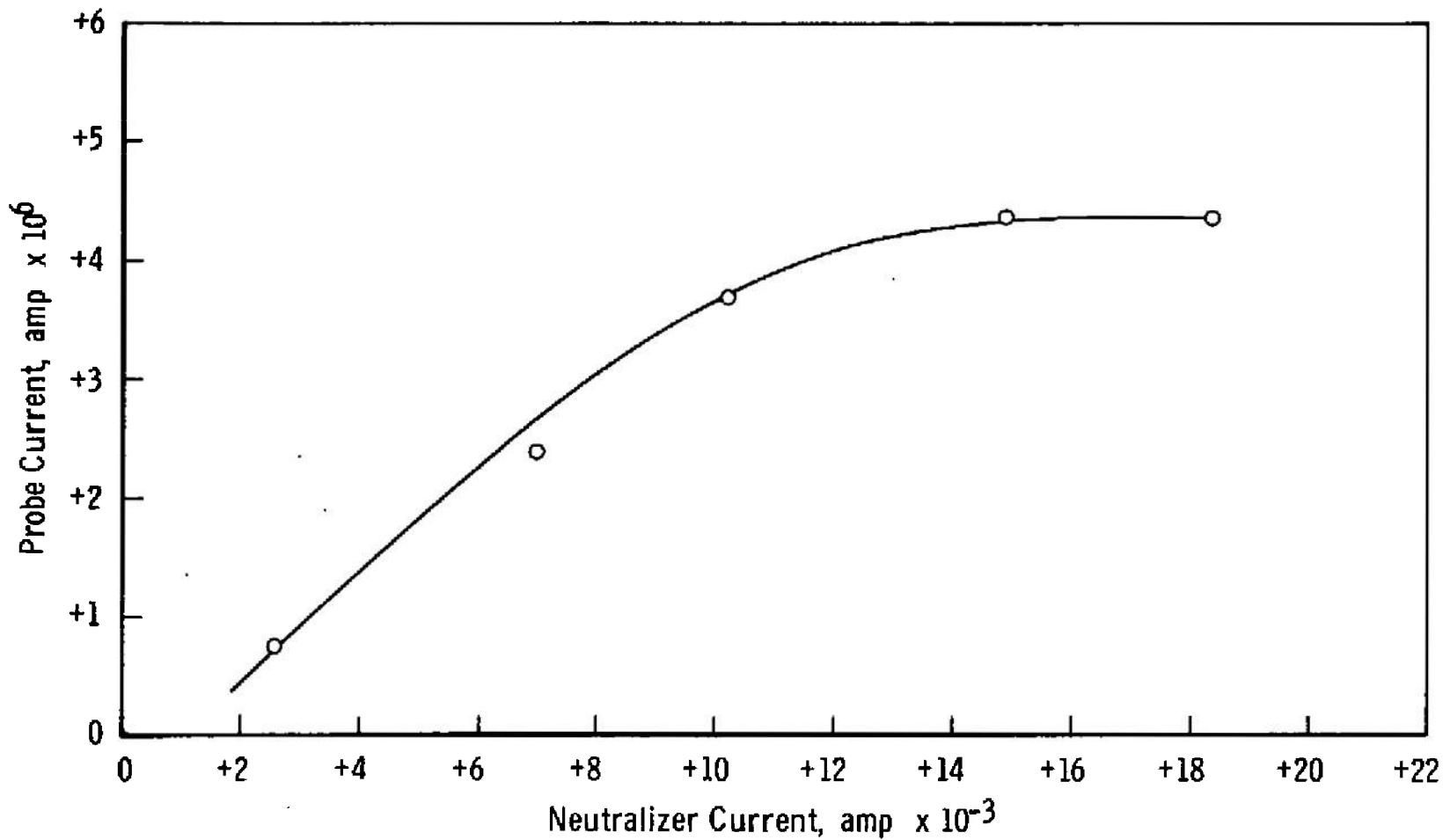


Fig. 36 Neutralizer Emission Current versus Neutralizer Heater Current

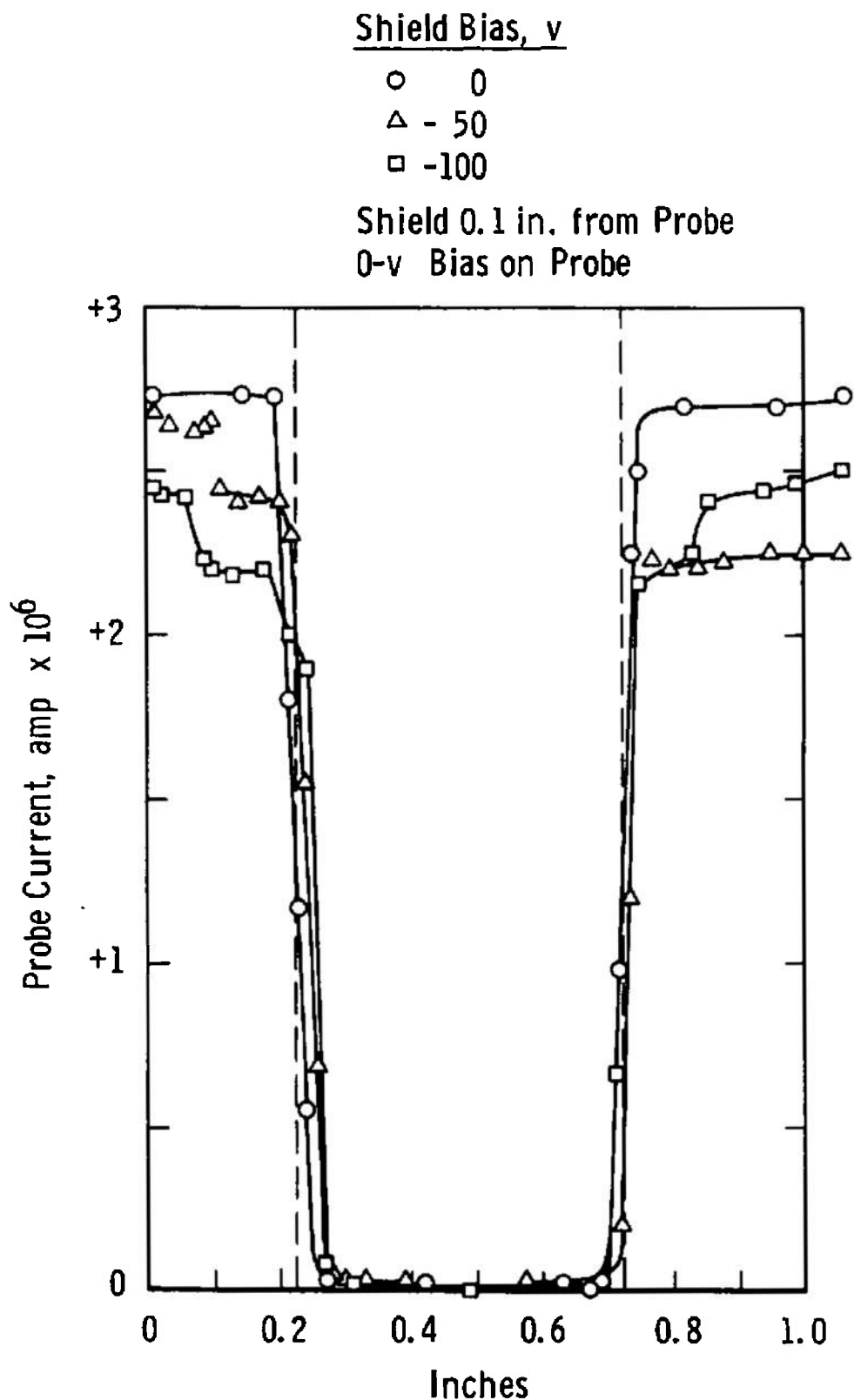


Fig. 37 Positive Charge Distribution in the Wake (Shield 0.1 in. from Probe)

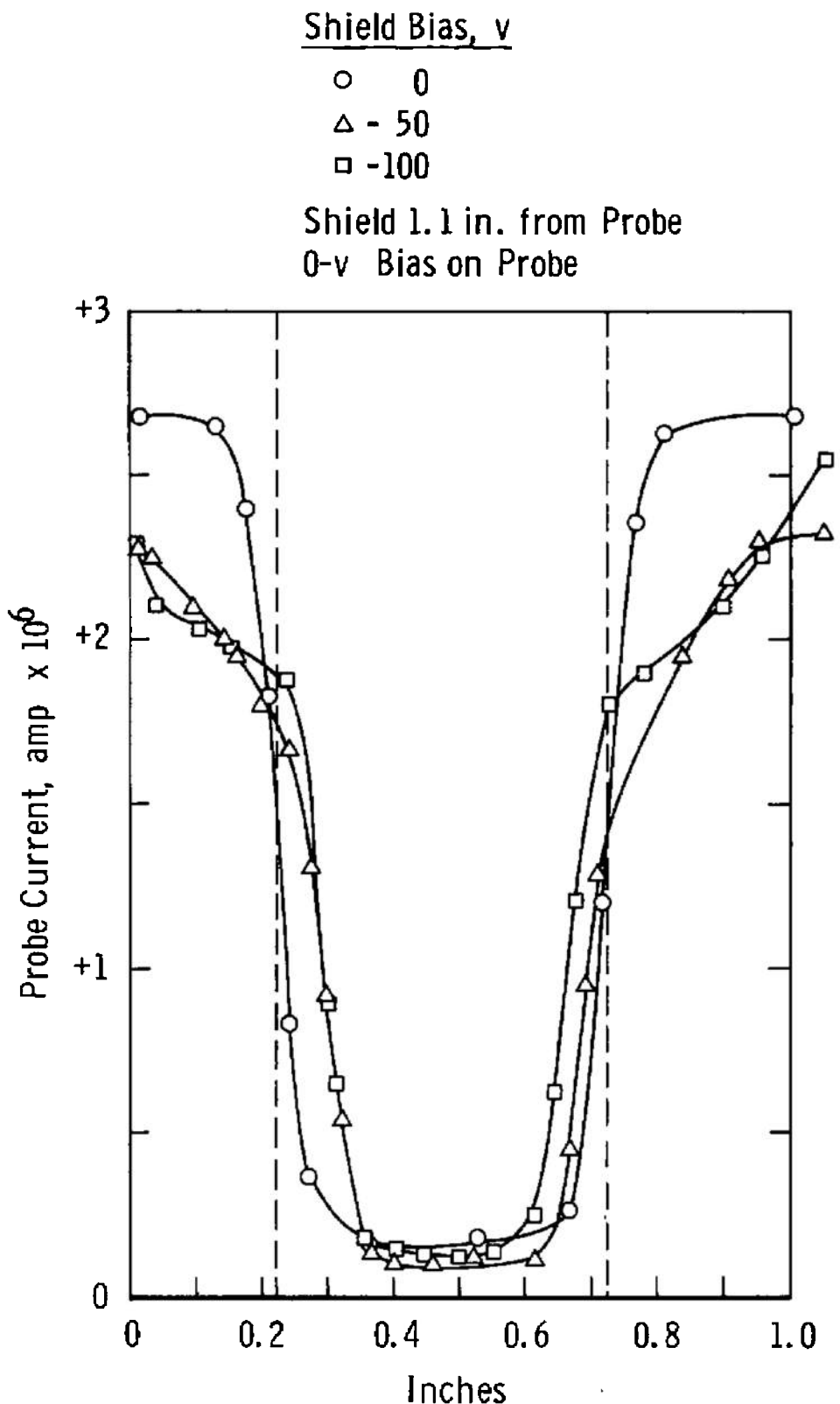


Fig. 38 Positive Charge Distribution in the Wake (Shield 1.1 in. from Probe)

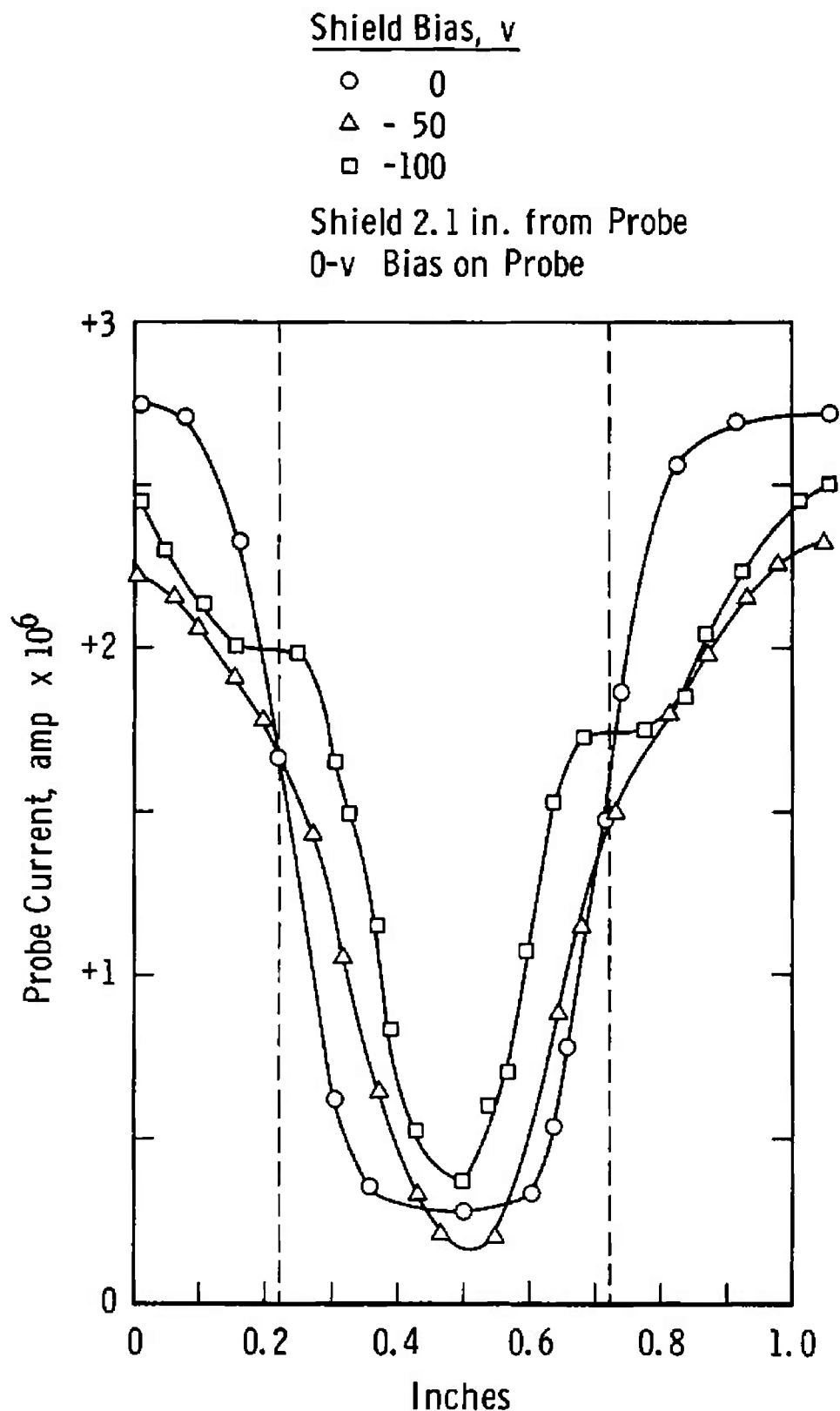


Fig. 39 Positive Charge Distribution in the Wake (Shield 2.1 in. from Probe)

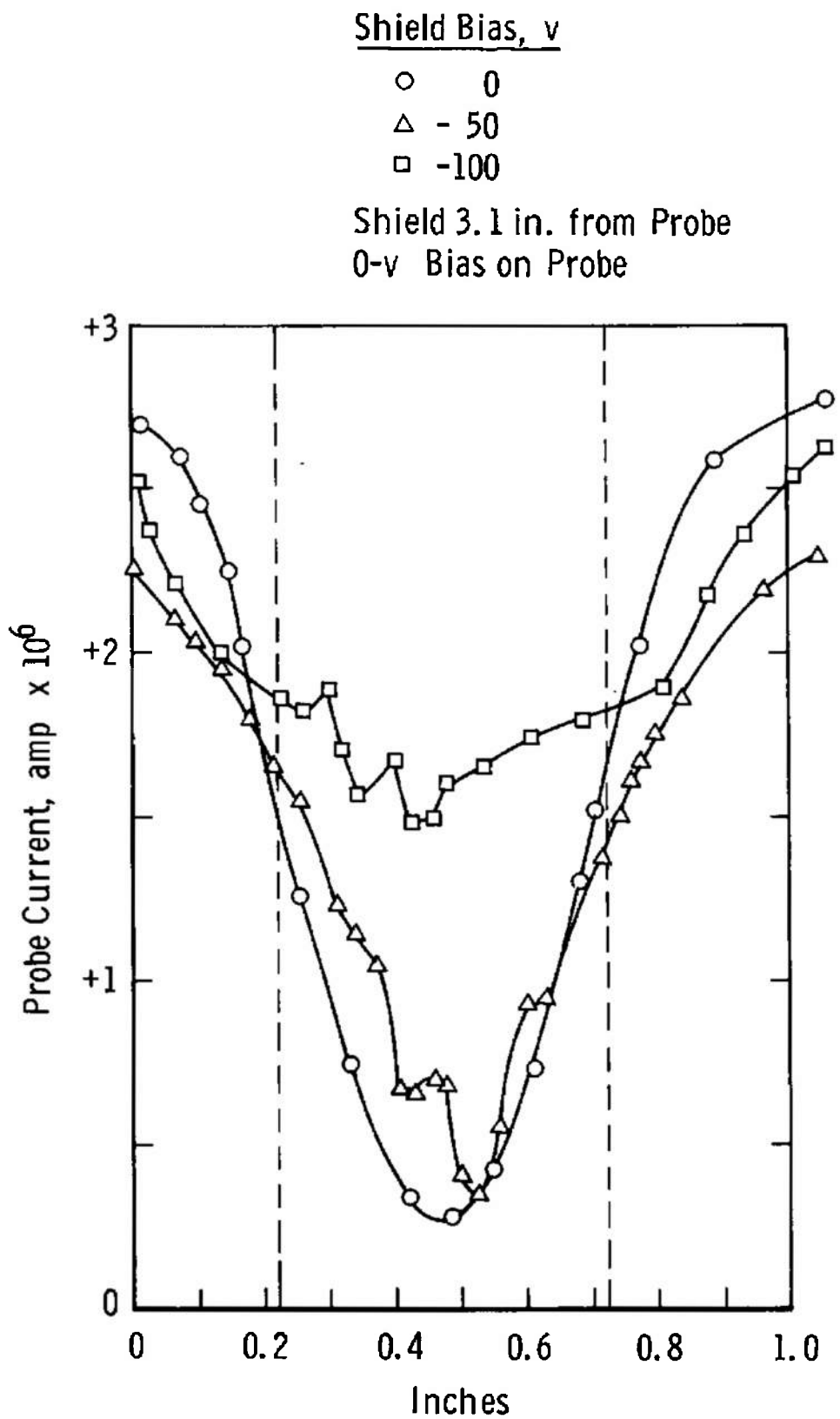


Fig. 40 Positive Charge Distribution in the Wake (Shield 3.1 in. from Probe)

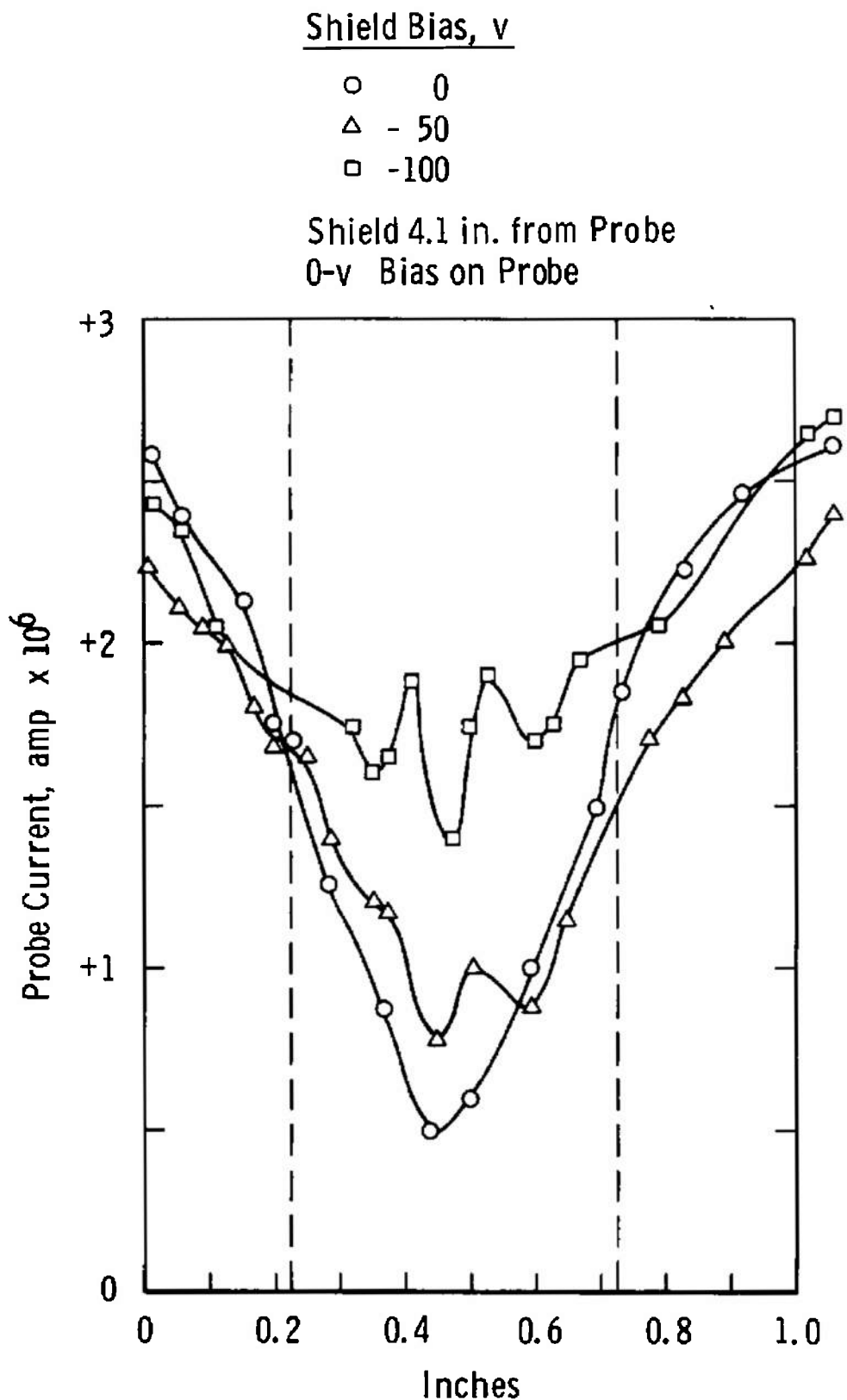


Fig. 41 Positive Charge Distribution in the Wake (Shield 4.1 in. from Probe)

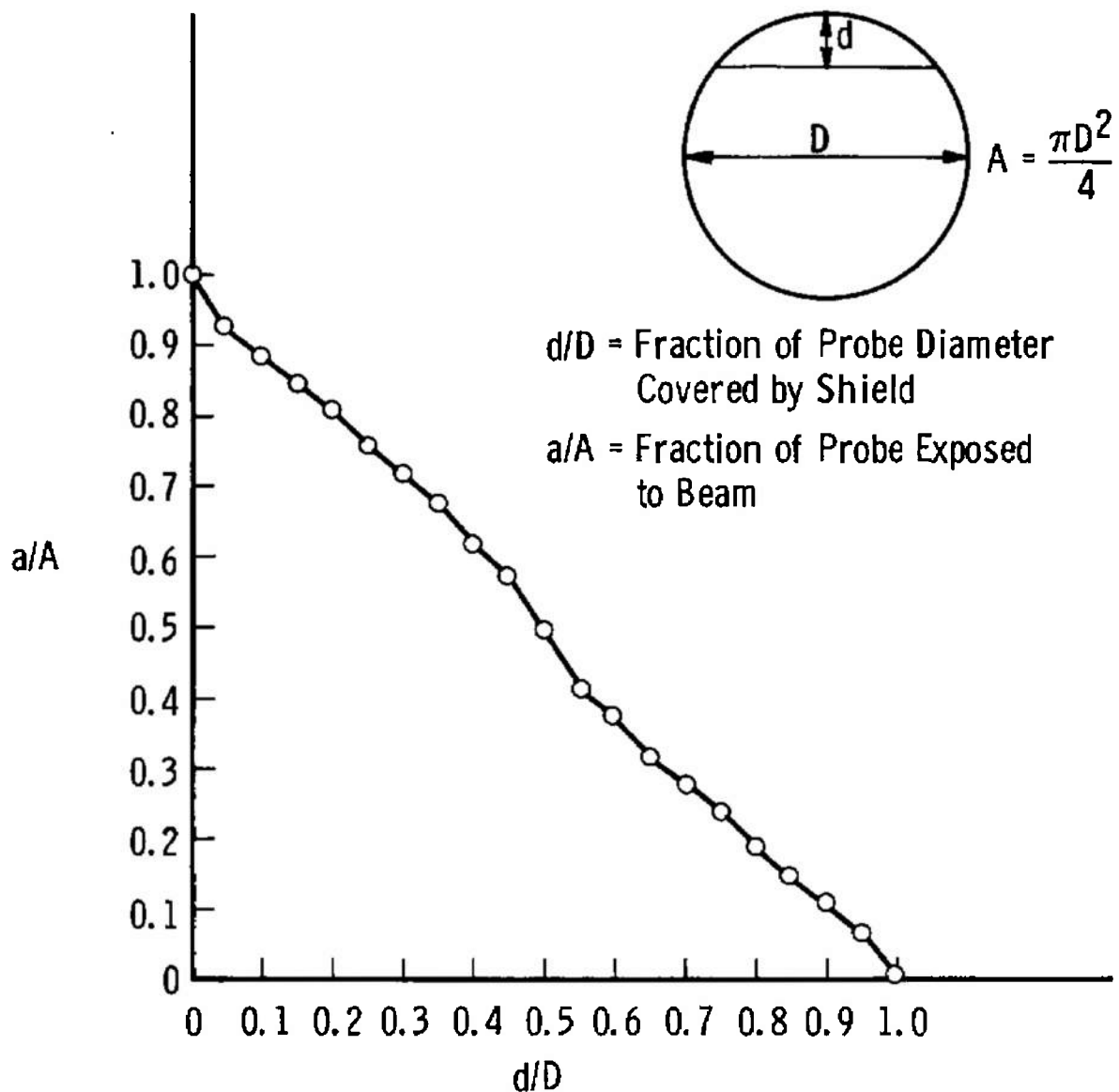


Fig. 42 Area of Probe Exposed as it Passes under the Shield

76

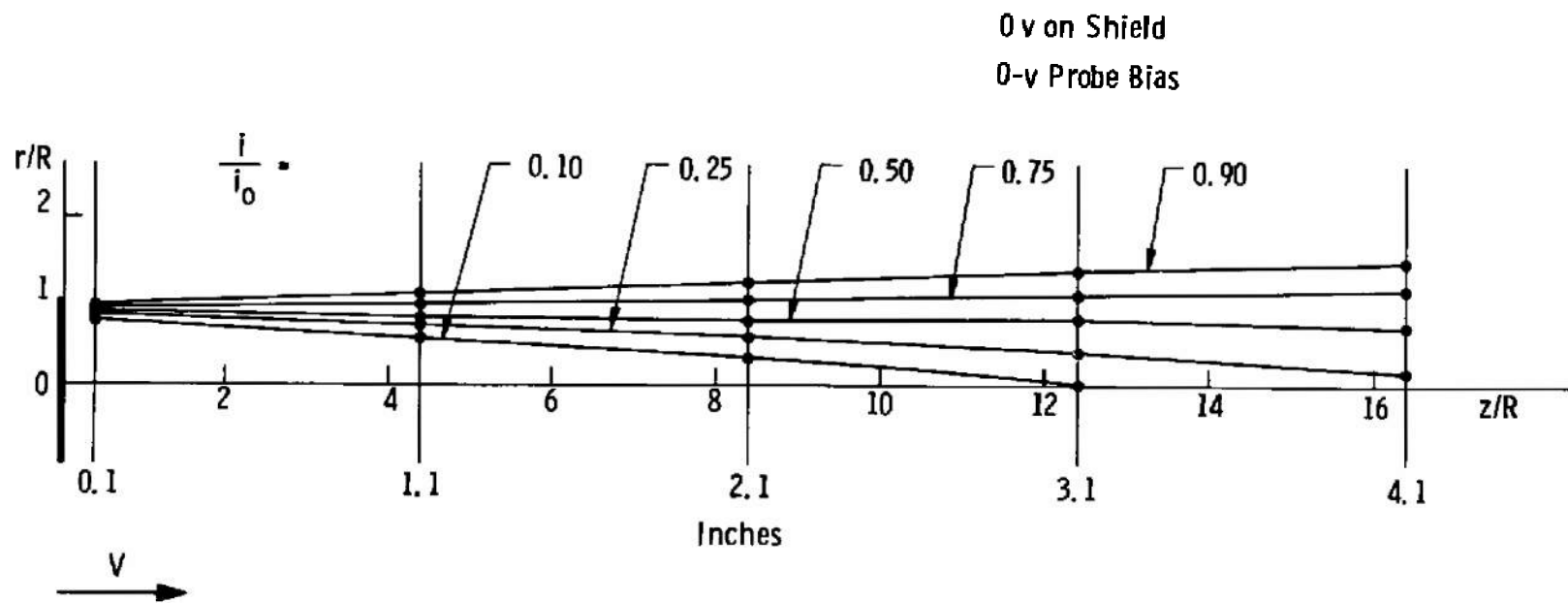


Fig. 43 Contour Plot of Positive Ions in the Wake (0 v on Shield)

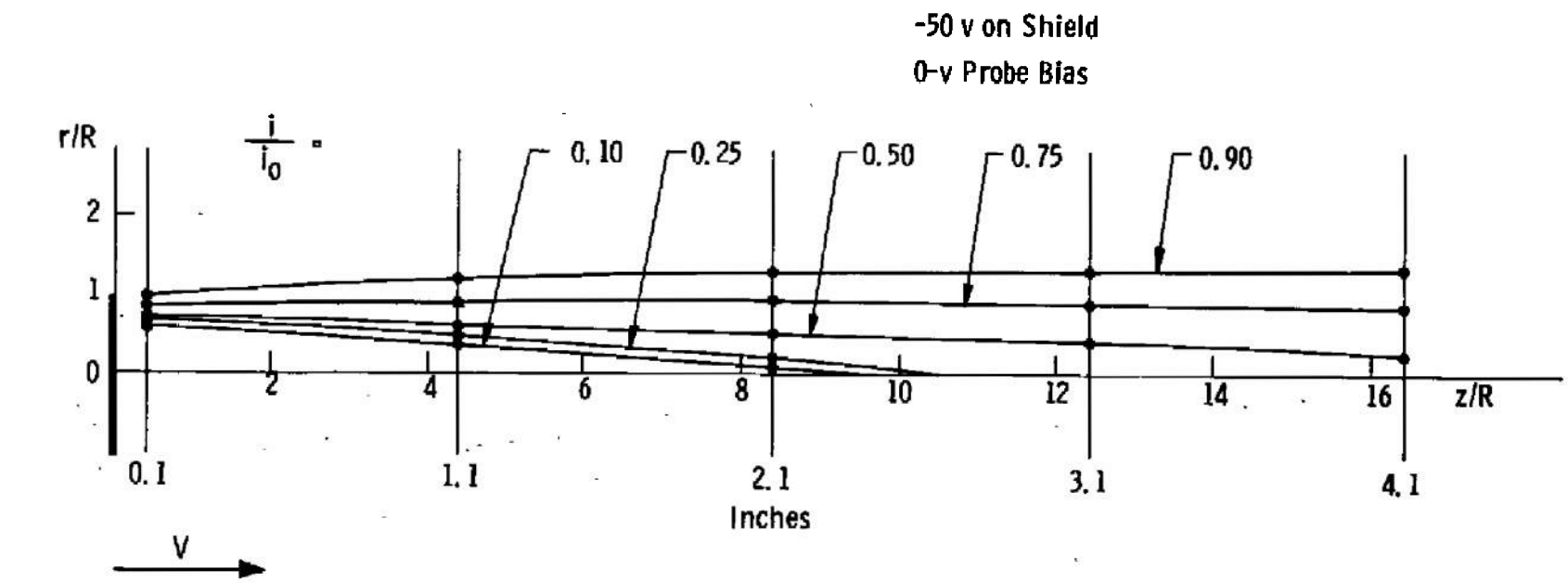


Fig. 44 Contour Plot of Positive Ions in the Wake (-50 v on Shield)

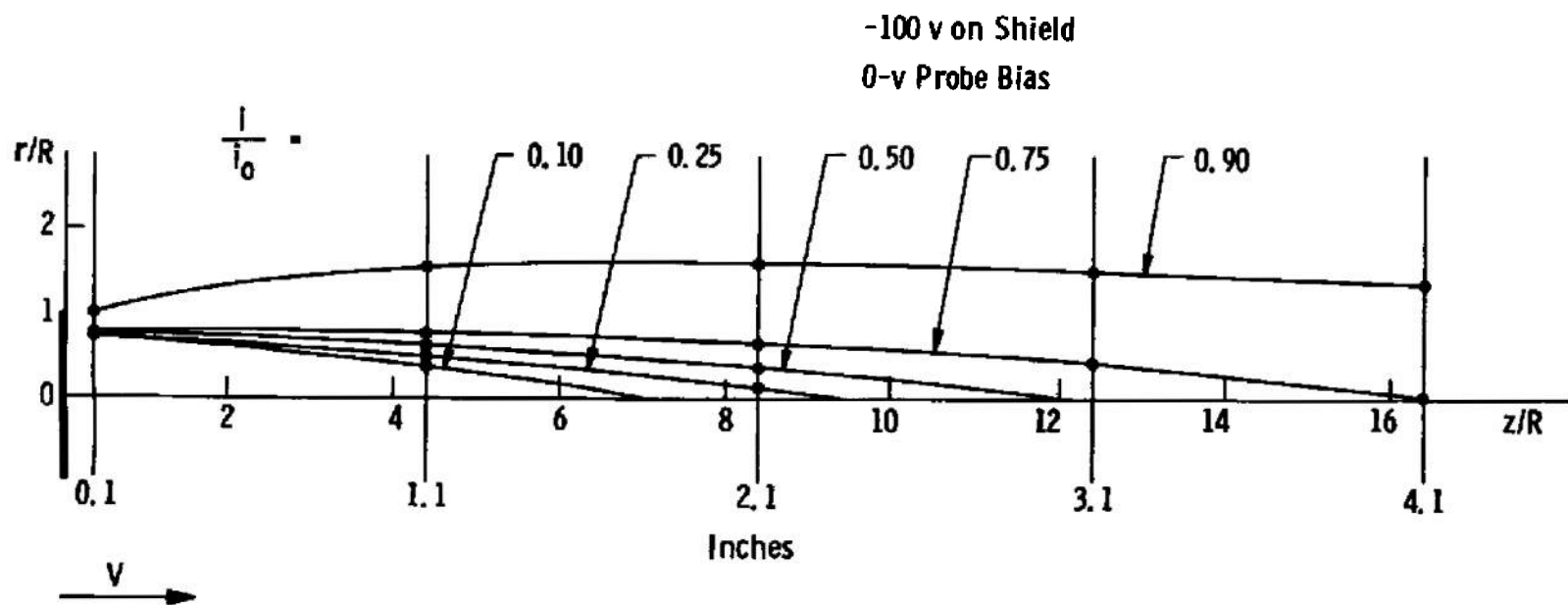


Fig. 45 Contour Plot of Positive Ions in the Wake (-100 v on Shield)

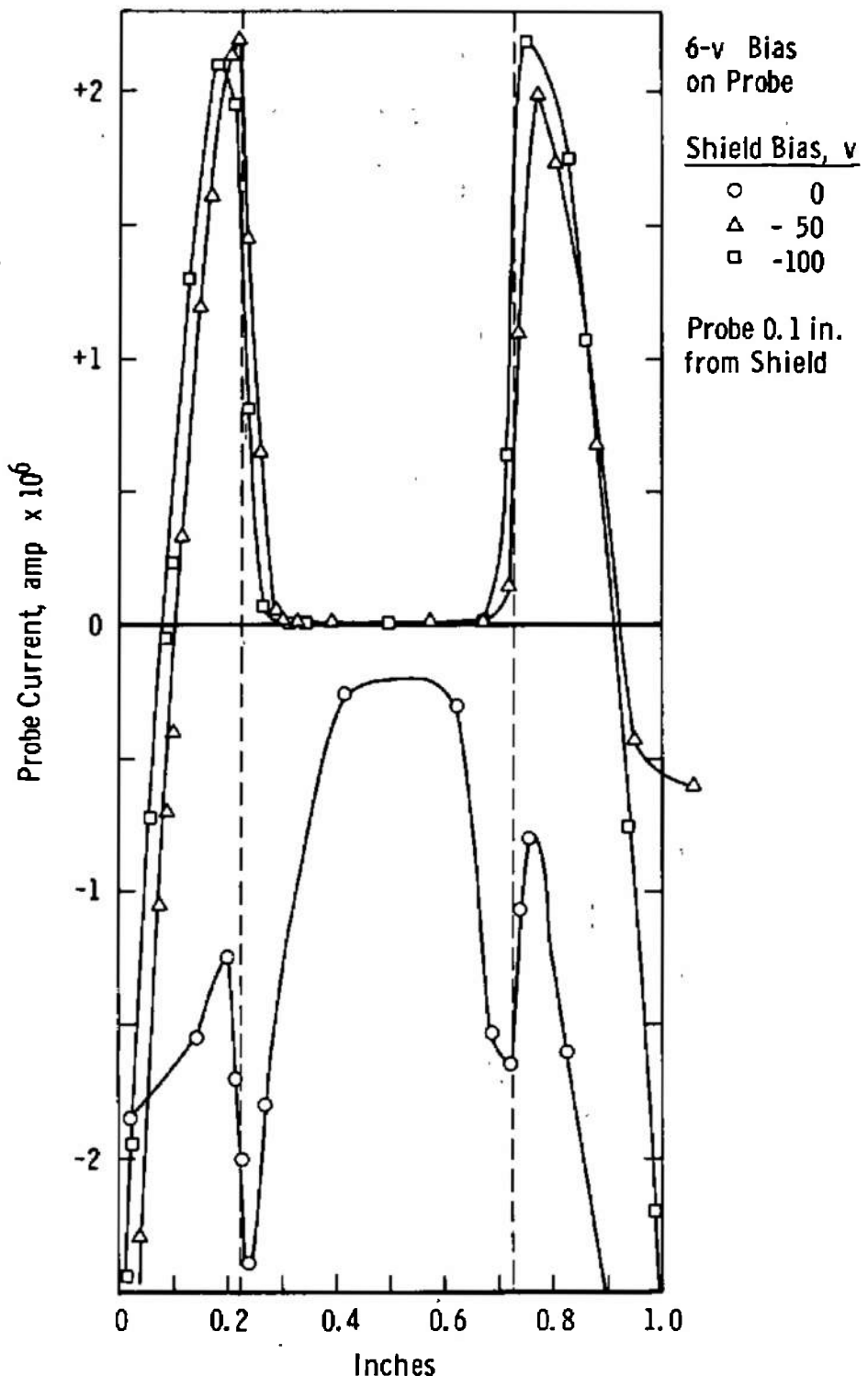


Fig. 46 Current Distribution Collected by Probe Biased 6.0 v
(Shield 0.1 in. from Probe)

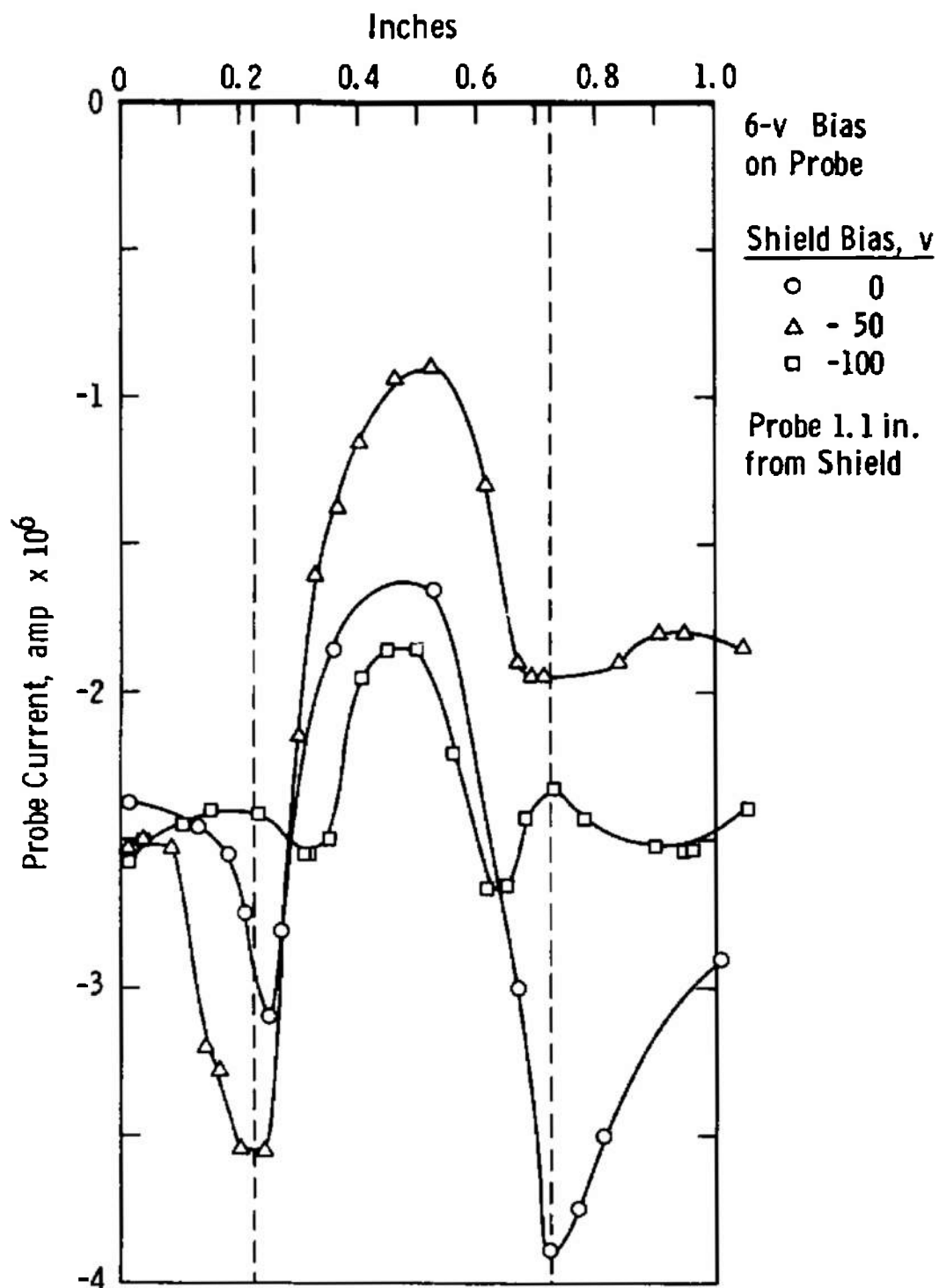


Fig. 47 Current Distribution Collected by Probe Biased 6.0 v
(Shield 1.1 in. from Probe)

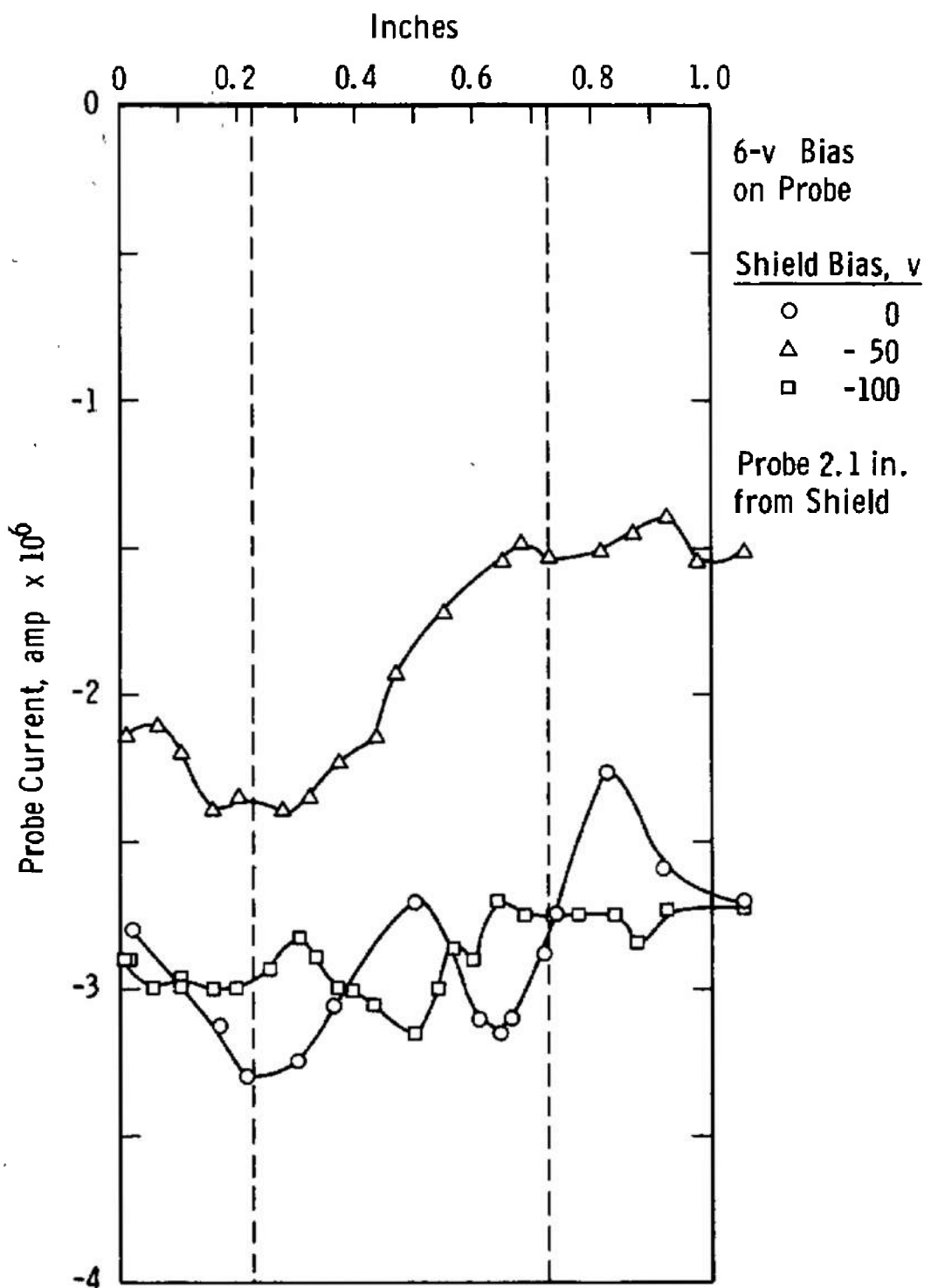


Fig. 48 Current Distribution Collected by Probe Biased 6.0 v
(Shield 2.1 in. from Probe)

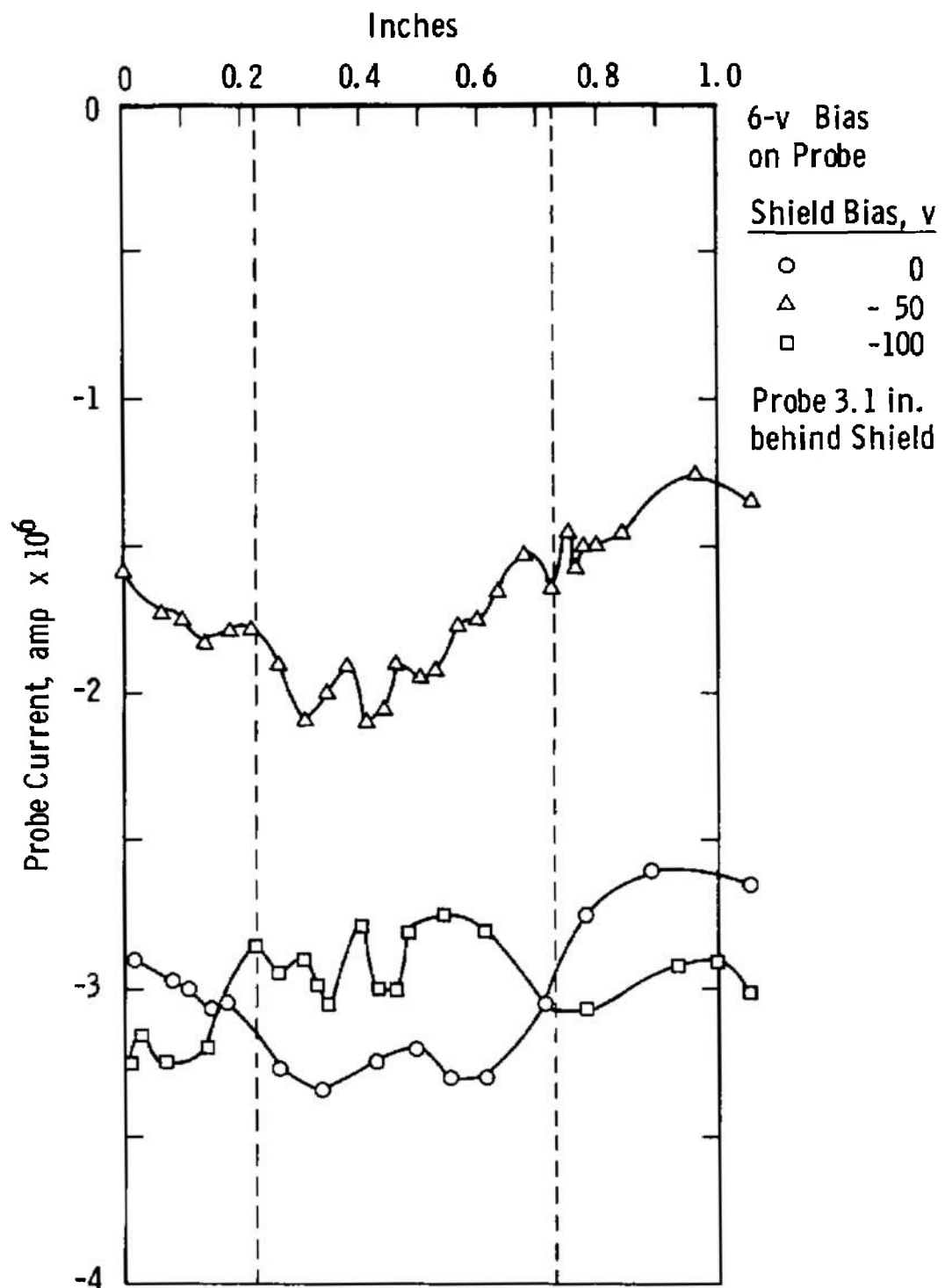


Fig. 49 Current Distribution Collected by Probe Biased 6.0 v
(Shield 3.1 in. from Probe)

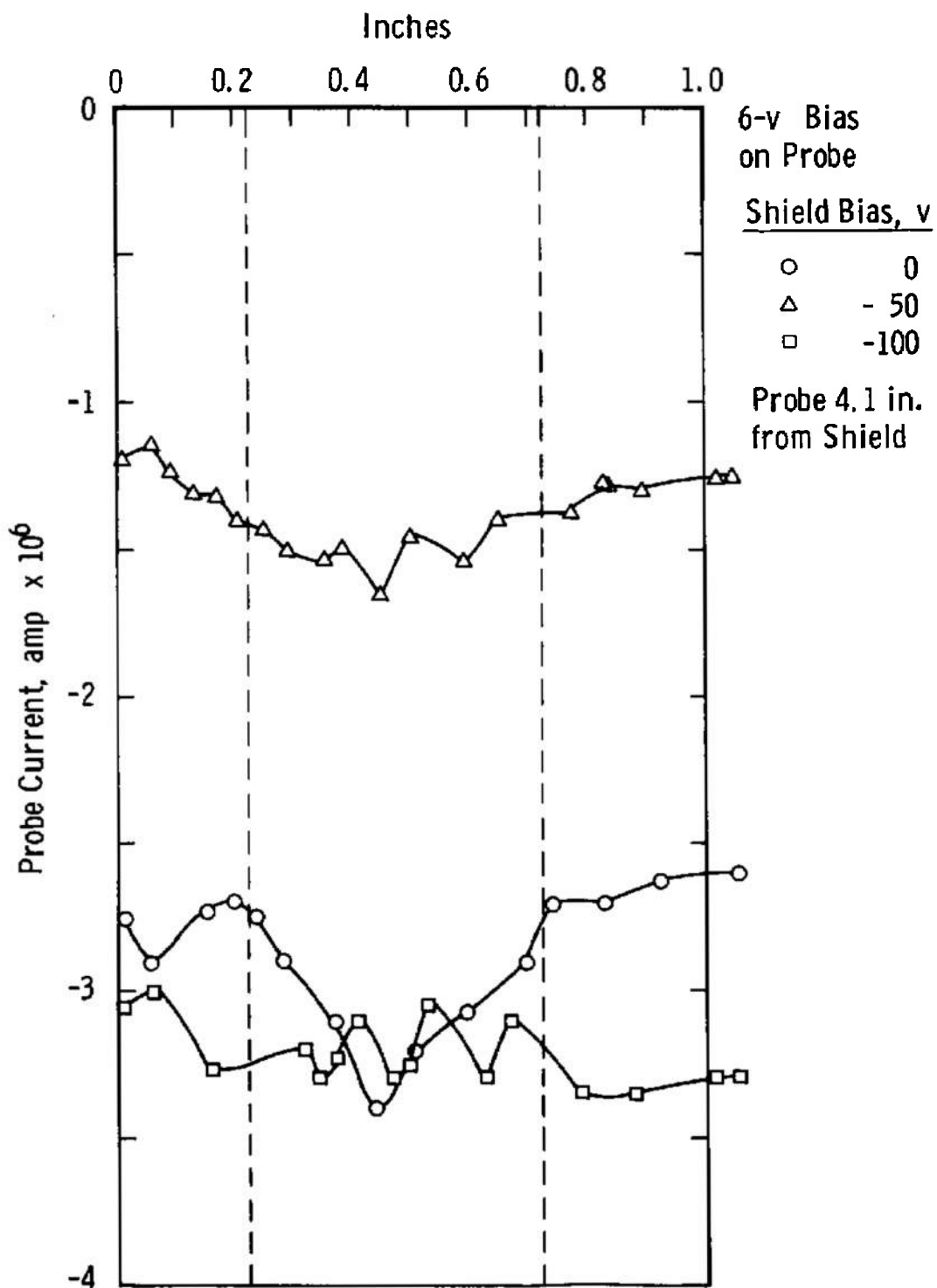


Fig. 50 Current Distribution Collected by Probe Biased 6.0 v
(Shield 4.1 in. from Probe)

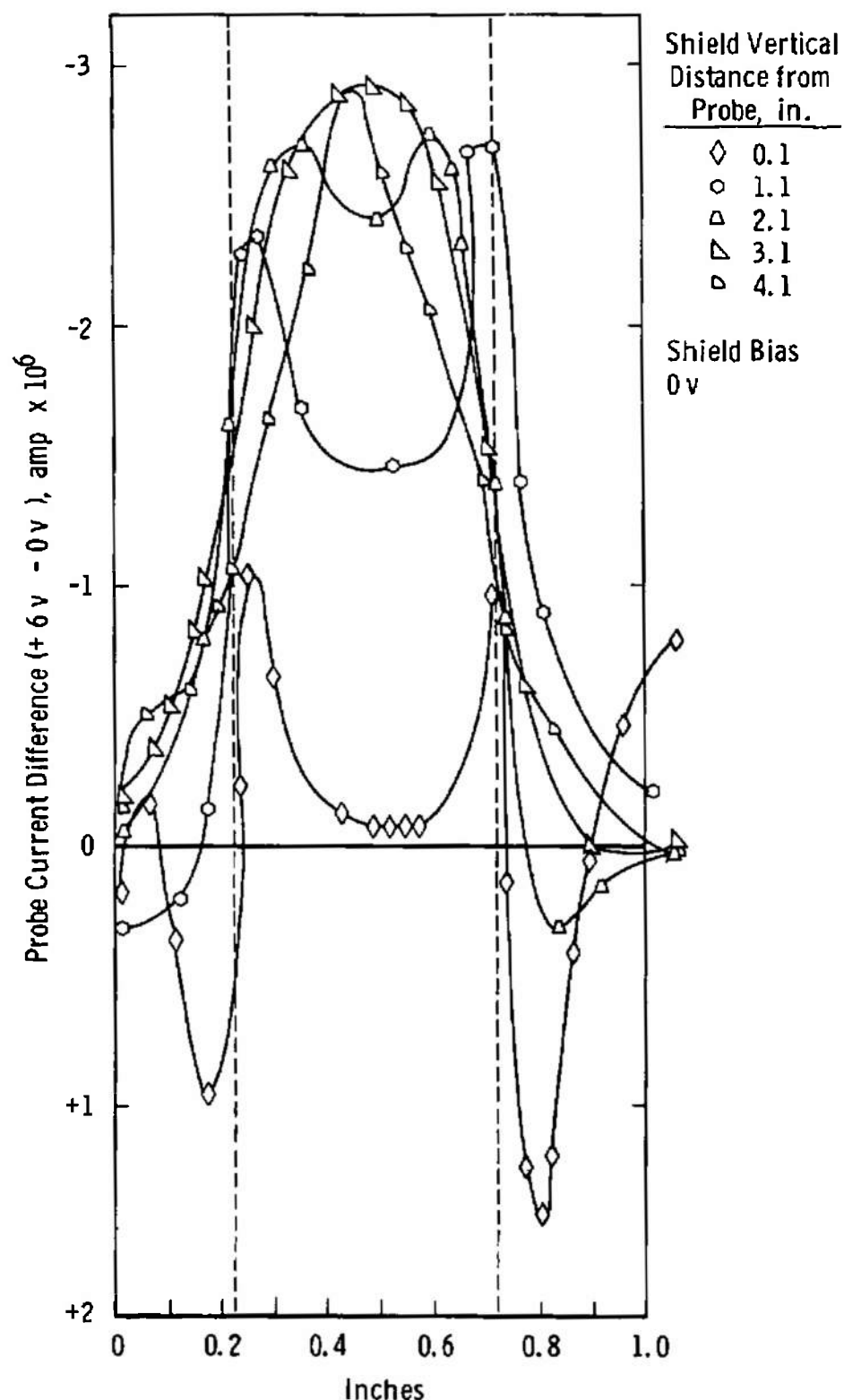


Fig. 51 Probe Current Difference (0 v on Shield)

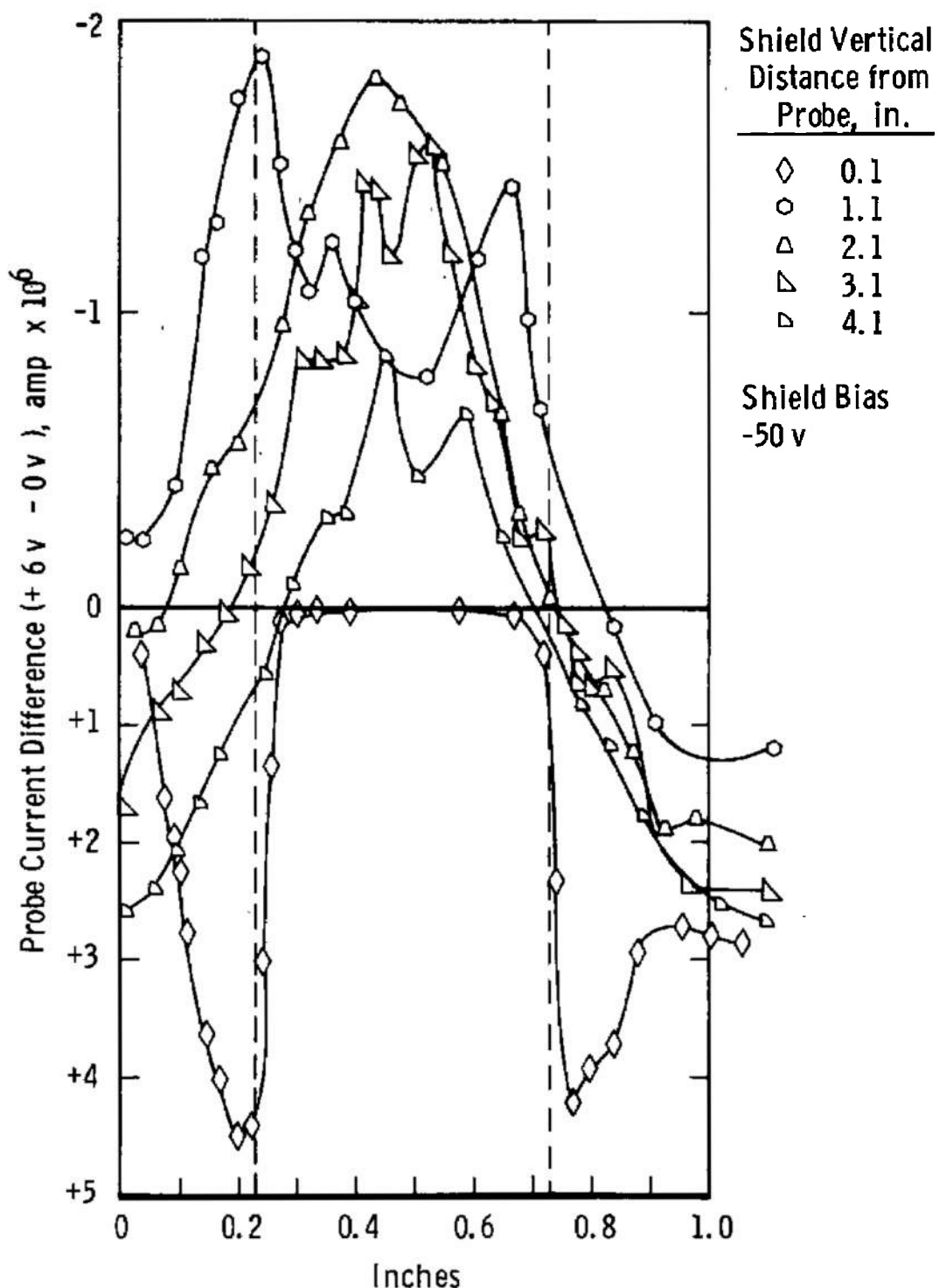


Fig. 52 Probe Current Difference (-50 v on Shield)

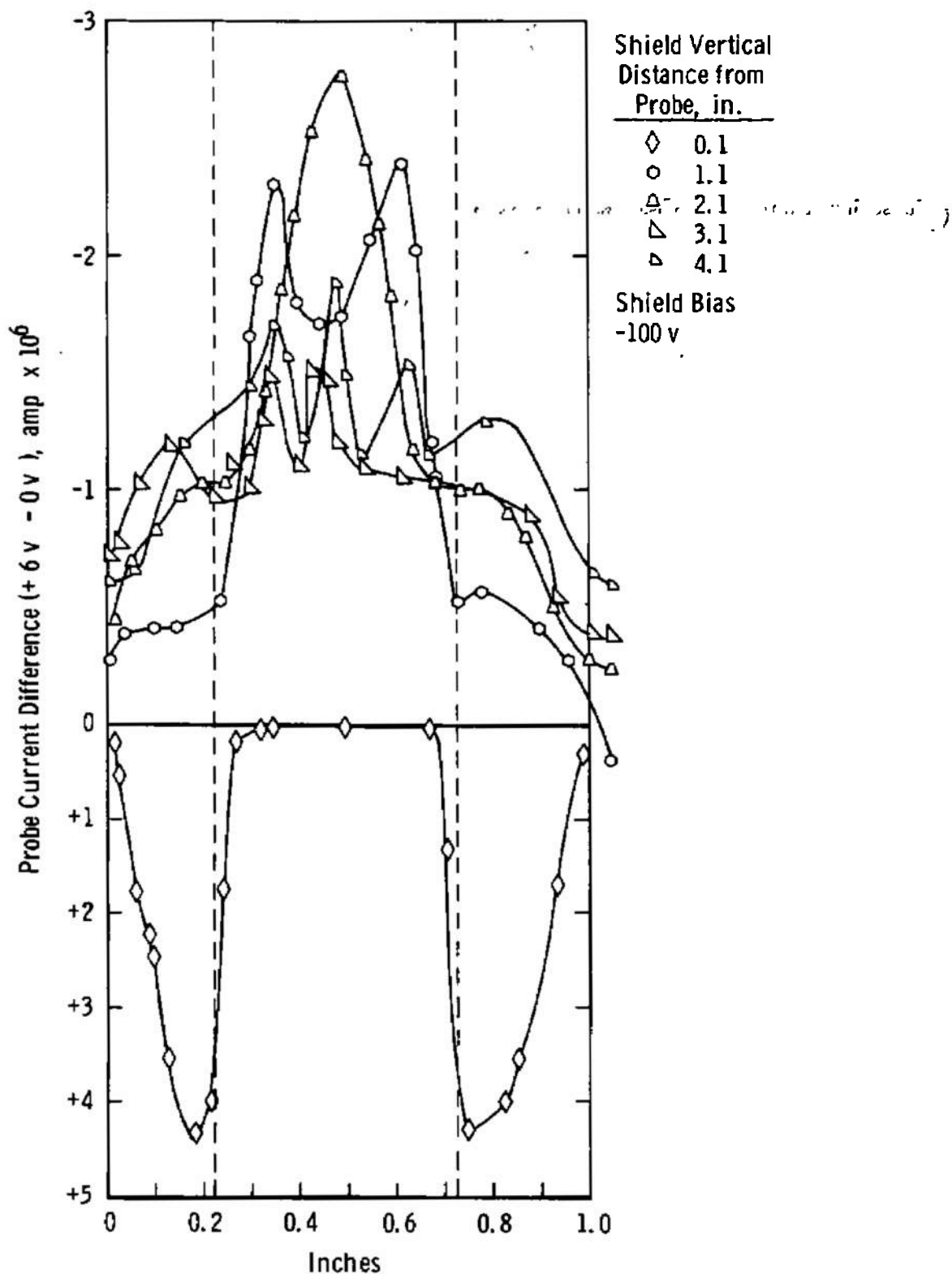


Fig. 53 Probe Current Difference (-100 v on Shield)

UNCLASSIFIED

Security Classification

DOCUMENT CONTROL DATA - R&D

(Security classification of title, body of abstract and indexing annotation must be entered when the overall report is classified)

1 ORIGINATING ACTIVITY (Corporate author) Arnold Engineering Development Center ARO, Inc., Operating Contractor Arnold Air Force Station, Tennessee		2a REPORT SECURITY CLASSIFICATION UNCLASSIFIED 2b GROUP N/A
3 REPORT TITLE INSTRUMENTATION DEVELOPMENT PROGRAM SUMMARY REPORT		
4 DESCRIPTIVE NOTES (Type of report and inclusive dates) Summary Report		
5 AUTHOR(S) (Last name, first name, initial) Hines, R. H. and Crosswy, F. L., ARO, Inc.		
6 REPORT DATE April 1967	7a. TOTAL NO OF PAGES 97	7b. NO OF REFS 21
8a. CONTRACT OR GRANT NO. AF 40(600)-1200	9a. ORIGINATOR'S REPORT NUMBER(S) AEDC-TR-66-233	
b. PROJECT NO. 5730	9b. OTHER REPORT NO(S) (Any other numbers that may be assigned this report) N/A	
c. Program Element 62405184		
d.		
10 AVAILABILITY/LIMITATION NOTICES Distribution of this document is unlimited.		
11. SUPPLEMENTARY NOTES Available in DDC.		12. SPONSORING MILITARY ACTIVITY Arnold Engineering Development Center Air Force Systems Command Arnold Air Force Station, Tennessee
13 ABSTRACT The design and operational characteristics of an in-house-built 5-cm-diam Kaufman-type ion engine that was used to evaluate diagnostic methods is presented. The discharge of the ion engine was investigated and analyzed by employing various types of material probes. The emissive probe was used to determine the beam potential, the electron temperature, and the ion impingement current density. The double Langmuir probe was used to determine electron temperature and ion impingement current density for cross correlation between probes. The analytical and experimental results are compared and discussed.		

UNCLASSIFIED

Security Classification

14 KEY WORDS	LINK A		LINK B		LINK C	
	ROLE	WT	ROLE	WT	ROLE	WT
ion engines electric propulsion development program instrumentation langmuir probes electron temperatures current density			17-5.			

1. Ion motors -- Diagnostic methods
2. Electric propulsion system --
3. Instrumentation -- Development

INSTRUCTIONS

1. ORIGINATING ACTIVITY: Enter the name and address of the contractor, subcontractor, grantee, Department of Defense activity or other organization (*corporate author*) issuing the report.

2a. REPORT SECURITY CLASSIFICATION: Enter the overall security classification of the report. Indicate whether "Restricted Data" is included. Marking is to be in accordance with appropriate security regulations.

2b. GROUP: Automatic downgrading is specified in DoD Directive 5200.10 and Armed Forces Industrial Manual. Enter the group number. Also, when applicable, show that optional markings have been used for Group 3 and Group 4 as authorized.

3. REPORT TITLE: Enter the complete report title in all capital letters. Titles in all cases should be unclassified. If a meaningful title cannot be selected without classification, show title classification in all capitals in parenthesis immediately following the title.

4. DESCRIPTIVE NOTES: If appropriate, enter the type of report, e.g., interim, progress, summary, annual, or final. Give the inclusive dates when a specific reporting period is covered.

5. AUTHOR(S): Enter the name(s) of author(s) as shown on or in the report. Enter last name, first name, middle initial. If military, show rank and branch of service. The name of the principal author is an absolute minimum requirement.

6. REPORT DATE: Enter the date of the report as day, month, year, or month, year. If more than one date appears on the report, use date of publication.

7a. TOTAL NUMBER OF PAGES: The total page count should follow normal pagination procedures, i.e., enter the number of pages containing information.

7b. NUMBER OF REFERENCES: Enter the total number of references cited in the report.

8a. CONTRACT OR GRANT NUMBER: If appropriate, enter the applicable number of the contract or grant under which the report was written.

8b, 8c, & 8d. PROJECT NUMBER: Enter the appropriate military department identification, such as project number, subproject number, system numbers, task number, etc.

9a. ORIGINATOR'S REPORT NUMBER(S): Enter the official report number by which the document will be identified and controlled by the originating activity. This number must be unique to this report.

9b. OTHER REPORT NUMBER(S): If the report has been assigned any other report numbers (either by the originator or by the sponsor), also enter this number(s).

10. AVAILABILITY/LIMITATION NOTICES: Enter any limitations on further dissemination of the report, other than those imposed by security classification, using standard statements such as:

- (1) "Qualified requesters may obtain copies of this report from DDC."
- (2) "Foreign announcement and dissemination of this report by DDC is not authorized."
- (3) "U. S. Government agencies may obtain copies of this report directly from DDC. Other qualified DDC users shall request through _____."
- (4) "U. S. military agencies may obtain copies of this report directly from DDC. Other qualified users shall request through _____."
- (5) "All distribution of this report is controlled. Qualified DDC users shall request through _____."

If the report has been furnished to the Office of Technical Services, Department of Commerce, for sale to the public, indicate this fact and enter the price, if known.

11. SUPPLEMENTARY NOTES: Use for additional explanatory notes.

12. SPONSORING MILITARY ACTIVITY: Enter the name of the departmental project office or laboratory sponsoring (paying for) the research and development. Include address.

13. ABSTRACT: Enter an abstract giving a brief and factual summary of the document indicative of the report, even though it may also appear elsewhere in the body of the technical report. If additional space is required, a continuation sheet shall be attached.

It is highly desirable that the abstract of classified reports be unclassified. Each paragraph of the abstract shall end with an indication of the military security classification of the information in the paragraph, represented as (TS), (S), (C), or (U).

There is no limitation on the length of the abstract. However, the suggested length is from 150 to 225 words.

14. KEY WORDS: Key words are technically meaningful terms or short phrases that characterize a report and may be used as index entries for cataloging the report. Key words must be selected so that no security classification is required. Identifiers, such as equipment model designation, trade name, military project code name, geographic location, may be used as key words but will be followed by an indication of technical context. The assignment of links, rules, and weights is optional.

UNCLASSIFIED

Security Classification